Budapest University of Technology and Economics

Dynamic analysis and tracking control of underactuated multibody systems

by

László Bencsik

Submitted as a partial fulfilment of the requirements
for the degree of Doctor of Philosophy in Mechanical Engineering
in the Pattantyús Ábrahám Géza School ol of PhD Studies
of the Budapest University of Technology and Economics.

Supervisor:
Dr. László Kovács

Budapest, March 30, 2017

Declaration of Authorship

I, László Bencsik, hereby declare that this Ph.D. thesis titled, 'Dynamic analysis and tracking control of underactuated multibody systems' and the work presented in it are my own. I confirm that all relevant resources are marked I have used while working on the thesis.

Signed: .....

Date: .....

Abstract

Dynamical systems with less independent control input than degrees of freedom are called underactuated. This Ph.D. thesis deals with the modelling and control issues of underactuated dynamical systems. In trajectory tracking control of underactuated systems, the stability behaviour have to be considered already during the control task definition. This work presents how the task of the system have to be selected, or how should it be modified for the stable operations. For the control of underactuated systems a novel technique is presented, which is based on a periodic variation of the different control objectives. This periodic controller can be used in other problems effectively as well. For example in case of the handling of driving torque saturation in trajectory tracking problems. One of the main contributions of the work is a novel technique, which makes possible the direct stability analysis of such systems, which are modelled by redundant coordinates. With this technique the multibody systems can be investigated systematically and efficiently. It is shown that the techniques of multibody systems are useful in the field of biomechanics as well. The investigation shows how the energy consumption of human running is related with different parameters of the motion.

Keywords: underactuated mechanical systems, multibody systems, servo-constraints, internal dynamics, actuator saturation, biomechanics

Kivonat

A doktori értekezés alulaktuált dinamikai rendszerek modellezésével és szabályozásával foglalkozik. Alulaktuált rendszerek pályakövetési feladataiban már a feladat megfogalmazásakor figyelembe kell venni a rendszer stabilitási tulajdonságait. A dolgozat bemutatja, hogy milyen módon kell a rendszer feladatát megválasztani, esetleg módosítani a stabil működés eléréséhez. A probléma megoldásához egy új, periodikus feladatmegosztáson alapuló módszer kerül bemutatásra. Ezen periodikus módszer más gyakorlati problémákban is hatékonyan alkalmazható, mint például a robotok beavatkozó egységeinek nyomatékszaturációját kezelő szabályozások esetén. Az értekezés a rendszer stabilitásának vizsgálatához egy új módszert mutat be, mellyel szisztematikusan vizsgálhatóak többtest-dinamikai rendszerek. A dolgozat egyik alkalmazási feladata a futás biomechanikai modelljével foglalkozik. Ez ugyancsak tekinthető alulaktuált rendszernek és ilyen módon használhatóak a kidolgozott többtest-dinamikai rendszerek leírására szolgáló módszerek.

Kulcsszavak: alulaktuált dinamikai rendszerek, kinematikai redundancia, kiszámított nyomatékok módszere, többtest-dinamikai rendszerek, periodikus szervó kényszerek, biomechanika

Acknowledgements

First of all I would like to express my greatest thanks to my family for their support of my studies and every other field of my life, which enabled me to prepare this thesis.

I would like to express my special thanks to László Kovács, who continuously supported my work with his knowledge and constructive advices. Nevertheless I am grateful to him for his help and guidance during my previous university studies. I would like to gratefully thank Prof. Gábor Stépán, whose encouragement and support, provided excellent research conditions. I would never have been able to finish my dissertation without Ambrus Zelei, a member of the "simulation trio". Thank for the valuable discussions, for the many cases more valuable arguing, and support which I could always have relied on. I express my special thanks to Roland Zana, who helped in the experimental validation. I also express my thanks to Anna Czeller for the support and the encouragement at the final and hardest period.

This work was supported by the HAS-BME Research Group on Dynamics of Machines and Vehicles under Grant No. MTA-NSF/103.

Contents

List of Figures

List of Tables

Introduction

Underactuated systems appear in the engineering structures and also in the nature. A system which has less independent actuators than the degrees of freedom said to be underactuated. Basically the same definitions can be found in [1] and in [2].

It is easy to find examples for underactuated systems since the human motion contains various underactuated problems. For example it is enough to examine the motion of the fingers where there are three joints but only 2 pairs of tendons transmit the motion. The flight of birds are also underactuated, since most birds can not elevate and can not rotate around the vertical axis without forward flying. Thus they cannot follow an arbitrarily trajectory, it is also true for the swimming of fishes. In field of engineering, cranes, ships and planes can be mentioned as the first characteristic examples. In case of a conventional overhead crane the horizontal direction of the trolley and the carried object is not independent and it could cause unwanted oscillations. The ships can not turn without forward or backward motion like the fishes. When the cranes are mounted on ships which, is quite frequent in the building of off-shore oil platforms these, problems are coupled and makes the control more complicated.

The evolution of robotic industry required novel robots, which have underactuated behaviour. The flexibility in robotics was appeared first in the parallel robot called Delta [3] which is doing pick and place task on small objects like bon-bons with high operating velocity. Here the flexibility is used to avoid getting in stuck in proximity of singular configurations. Here the flexibility avoids to getting stuck in near of the singular configurations. The light weight makes possible the energy efficiency, the agility and it makes possible the cooperation with humans like the KUKA LBR robot [4]. Since environment compliance is needed, these robots contain compliant joints, which increase the number of degrees of freedoms without additional actuators. During this development the engineers tried to mimic the nature, for example the graspers [5] [6] are designed similar to a human hand. In these applications the flexibility of the device or the not driven joints cause the underactuation.

Beside these examples the failure or saturation of an actuator, could be modelled as underactuation in a classical robotic applications [1], [7], [8].

The appropriate motion control of the humans or animals is result of a long learning process during childhood. This process could be much more difficult, when these skills have to be studied again after an unfortunate accident or disease. In the rehabilitation process, generally the balancing is the most difficult t task. In order to improve the balancing ability the physiotherapists use external devices like the balanceboard [9]. This hemisphere based plate introduces a further unactuated joint and makes the stable standing even more complicated. Since this further underactuation requires much more attention from the patient, it could increase the speed of the learning process. As a much more cheerful example sport device Jetovator can be mentioned [10] which is actuated by waterflow and its underactuated behaviour makes the control difficult and challenging.

In case of classical systems like cranes and ships the actuators are controlled by well trained operators and in some cases the computers give only an assistance like in the input-shaping method [11]. But most of underactuated robotic devices have to be controlled by computers and there is also a need for automation in cranes and in ships. The development of control strategies for underactuated systems were started in the early 90's and it remains a scientifically challenging task.

It seems straightforward to ask- why do we not copy the control of the humans or the animals? It seems easy to ask ourselves- how do we do it? The inventor of aviation Wilbur Wright gives us the sad truth: *I have asked dozens of bicycle riders how they turn to the left. I have never found a single person who stated all the facts correctly when first asked. They almost invariably said that to turn to the left, they turned the handlebar to the left and as a result made a turn to the left. But on further questioning them, some would agree that they first turned the handlebar a little to the right, and then as the machine inclined to the left they turned the handlebar to the left, and as a result made the circle inclining inwardly.*

The underactuation is a hot topic in robotics and in control methodology and several method and procedures exists for their control. This work focuses on the dynamic behaviour of the controlled underactuated systems, how these systems could be modelled for the controller, and how these could be analyzed. The goal is to exploit the knowledge of the dynamic properties in the control.

This work was originally motivated by an European Union 6th Framework Project (IST-2006-045530) project called Acroboter, coordinated by Department of Applied Mechanics.[12] The Acroboter is a special underactuated service robot application, which is moving on an almost obstacle free ceiling of a room, while transports the payload or a working unit similarly to gantry cranes.

The robot has to follow a trajectory in order to carry out the desired task. For the trajectory tracking the well-known computed torque control [13] is applied as a feed-forward control action.This model based controller requires appropriate dynamical modelling. Due to the high number of degrees of freedom and because closed kinematic chain can also be found in the system the effective dynamical modelling is also a key task. In favour of the generality the equation of motion is considered as a system, which is described by the non-minimum set of (dependent) coordinates [14].

Similar to the geometric constraints which give the relation between the dependent coordinates, the task of the controller is also given by additional constraints, the so-called servo-constraints. [15] [16] [17] [18]. These two types of constraint can be handled in an integrated framework and could give general method for the computation of the required control torque [19].

While the geometric constraints are naturally satisfied, the servo-constraints can not be fulfilled in all cases. With the generalization of computed torque controllers for underactuated systems we can see that some states of the system will not be specified by the control task. The dynamics associated with these uncontrolled states is referred to as the internal dynamics of the system [20]. These internal states can cause the unwanted oscillations and the instability of the system. In the literature there are several, mostly intuitive methods to handle this problem [21] [1]. Often the original task is modified by using a linear combination of the original and some new servo-constraints that aim to stabilize the internal dynamics of the system.

The main goal of this work is to explore the physical background of the instability of the internal dynamics, and give a systematic tools to overcome this problem. The proposed control procedures are based on the stability of the system and/or using mechanical performance measures like the effective mass or the dynamic manipulability [22]. In the subsequent chapters of this work first the multibody model based computed torque control and its solution technique will be introduced. Then for the dynamical analysis a novel technique will be introduced which makes possible the direct eigenvalue

analysis of multibody systems which are described by dependent coordinates. The application of this stability analysis technique will give a hand in the modification of the servo-constraints in order to get a feasible task. Beside the linear combination of the servo-constraints another possibility is the periodic variation of the servo-constraints. In one period the original servo-constraint is considered for realizing the desired motion, while in the subsequent period (which is typically shorter) a modified servo-constraint is applied to stabilize the unstable internal dynamics. The switching pattern and the period are chosen based on the numerical stability analysis. It is be shown that with application of the periodic servo-constraint the performance of the trajectory tracking could be enhanced effectively.

It is presented that, the method of periodically varied servo-constraints can be useful in actuator-saturation. Upon saturation, different sets of constraints are varied periodically to keep the reference point of the robot on the desired trajectory. The pattern of the periodic control is adjusted according to the variation of a new, manipulability type performance measure.

In the final chapter a different topic will be investigated. In that chapter the energy efficiency of the running is in the focus. It is shown that the techniques of multibody systems are useful in the field of biomechanics as well. The goal is to introduce a minimally complex biomechanical model which can characterise the dynamic effects of foot strike pattern and shank angle at foot touchdown. The investigation will show how the energy consumption of this locomotion is related with different parameters of the running.

Chapter 1

Dynamic modelling of multibody systems

The aim of this chapter is to introduce the applied multibody modelling and numerical simulation techniques of the presented work.

The parametrization of the equation of motion always depends on the aim of the investigation. The formulation must fit to the purpose of the motion analysis: in case of a controller design the direct input-output relationship has to appear, in case of Hardware-in-the-loop problem the measured variables have to be involved, in case of a motion simulation the structured layout and the time consumption of the simulation are the key problems. In all cases the chosen parametrization can be different.

The complexity of a dynamical model depends on the chosen coordinates, which have a major influence on the structure of the model and on the efficiency of numerical simulations. Often the chosen coordinates that are used to describe the configuration of the model belong to the contained kinematic pairs [23] [24]. These are called joint coordinates, which fully determine the pose of the system. If the number of the arbitrarily chosen coordinates is equal to the degrees of freedoms (DoF), then these joint coordinates are called the minimum set of generalized coordinates or shortly the generalized coordinates.

The position and the orientation of the end effector of an industrial robot can be described by using for example by Euler angles or by Roll-Pitch-Yaw [24] angles in the global coordinates system. These orientation representation formulations use three independent parameters for representing the orientation of a rigid body. However, in practical applications the Euler parameters [13] or the closely related quaternion and axis-angle based representations, which use four dependent scalar parameters, are more useful. The advantage of some redundant parameter based representations is that they can be used in case of singular configurations.

In fast, real time simulation it is important that the equation of motion have to be programmable in a way that computational costs are minimal, and computations may run parallel. In case of moderately complex multibody system the so-called natural coordinates [14] based parametrization is a commonly used approach. In that method the coefficient matrices do not contain transcendental and trigonometric terms which usually require additional computation efforts. In addition the mass matrix of a dynamical system modelled by these coordinates is almost always constant [14]. With this parametrization most of the control problems can be formulated efficiently.

In redundant coordinate based description techniques the holonomic or non-holonomic constraints will appear between the dependent coordinates and the equation of motion will be a Differential Algebraic Equation (DAE) instead of an Ordinary Differential Equation (ODE). The application of modelling techniques which are based on dependent coordinates is common in commercial

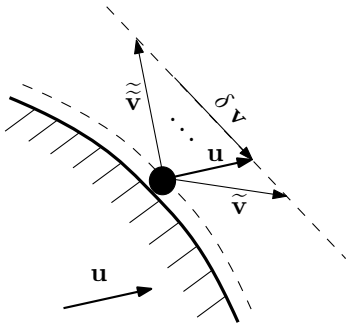

FIGURE 1.1. Velocity components associated with the constrained and admissible directions

multibody modelling softwares like ADAMS (Automated Dynamical Analysis of Mechanical Systems) [25], SIMPACK [26], or Matlab Simscape Multibody [27]. The multibody dynamics (MBD) softwares are become as standard tools as the Finite Element Analysis (FEA) technology, especially in the automotive industry [28].

These software packages provide a multibody simulation environment for mechanical systems, such as robots, vehicle suspensions, construction equipment and even for biomechanical models. The CAD models can be imported and the MBD simulation can be combined with finite element calculations for the stress analysis. In these commercial softwares the applied numerical methods and their effects are not exactly known, therefore it is preferred to develop individual MBD environments [29], [30] for academic purposes.

1.1 Equation of motion

A general multibody system can contain holonomic and non-holonomic constraints [23]. In the presented work only holonomic rheonomous systems will be investigated. Using the principle of virtual power [23] and the base of Newtonian mechanics, the fundamental equation of a constrained system can be written as

$$\int_m \delta\mathbf{v}^{\mathrm{T}}(\Delta m\dot{\mathbf{v}} - f_{\text{constraint}} - f_{\text{active}}) = 0, \tag{1.1}$$

where $\delta\mathbf{v}$ is the so-called virtual velocity, which is the difference of two possible velocities $\delta\mathbf{v} = \tilde{\mathbf{v}} - \tilde{\tilde{\mathbf{v}}}$ as illustrated in Fig. 1.1, Δm is an infinitesimal mass element of the system, f_{active} and $f_{constraint}$ represents the active and passive forces respectively. This formula is integrated over the mass volume of the system. Let us introduce $\mathbf{q} \in \mathbb{R}^n$ coordinates to describe the position of the system and with the elaboration of Eq. (1.1) the equation of motion of a holonomic multibody system can be written in Lagrangian formulation.

Using dependent descriptor coordinates $\mathbf{q} \in \mathbb{R}^n$ the equation of motion of a holonomic multibody system can be written as

$$\frac{\mathrm{d}}{\mathrm{d}t}\frac{\partial T}{\partial \dot{\mathbf{q}}} - \frac{\partial T}{\partial \mathbf{q}} = \mathbf{Q}(\mathbf{q}, \dot{\mathbf{q}}, t) + \mathbf{Q}_c(\mathbf{q}, t), \tag{1.2}$$

where T is the kinetic energy of the system and $\mathbf{Q}$ represents all the non-inertial and non-constraint forces. Since the descriptor coordinates are dependent, the constraint forces $\mathbf{Q}_c$ do not disappear, because nothing guarantees that $\delta\mathbf{v}$ is not perpendicular to $f_{\text{constraint}}$. In the related literature this equation is called as Lagrange's equations of the first kind. The connection between the bodies and the connection between the system and the environment are represented by constraints $(\phi_1, \ldots, \phi_l)$

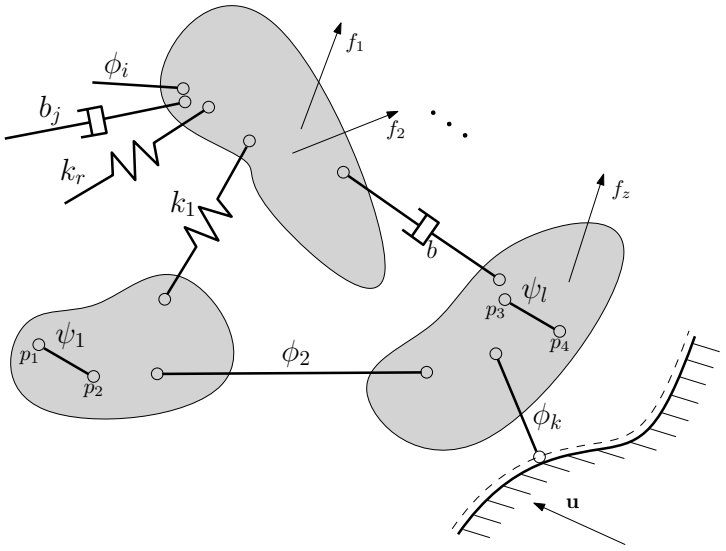

FIGURE 1.2. Schematic figure of a general multibody system

(see Fig. 1.2). Constrains $(\psi_1, \ldots, \psi_k)$ are the rigid body constraints [14]. These constraints are required for those bodies of the system which are modelled by dependent coordinates, e.g. in case of natural coordinates a 6 DoF rigid body is modelled by 12 coordinates. All of these $l + k = m$ number of constraints are involved in the following array

$$\boldsymbol{\varphi}(\mathbf{q}, t) = \mathbf{0} \,, \quad \boldsymbol{\varphi}(\mathbf{q}, t) \in \mathbb{R}^m. \tag{1.3}$$

The constraint force can be expressed as

$$\mathbf{Q}_c = -\boldsymbol{\Phi}^{\mathrm{T}} \boldsymbol{\lambda} \,, \quad \text{where } \boldsymbol{\Phi} = \frac{\partial \boldsymbol{\varphi}}{\partial \mathbf{q}}. \tag{1.4}$$

In the expression (1.4) Jacobian $\boldsymbol{\Phi}$ is orthogonal to the constrained surfaces thus it gives the direction of the constraint forces and $\boldsymbol{\lambda}$ is the array of Lagrange multipliers, which are proportional to the magnitude of the constraint forces. After the elaboration of Eq. (1.2) the equation of motion can be written in the general form

$$\mathbf{M}\ddot{\mathbf{q}} + \mathbf{c} + \boldsymbol{\Phi}^{\mathrm{T}} \boldsymbol{\lambda} = \mathbf{Q} \,, \tag{1.5}$$

where $\mathbf{M}$ is the mass matrix and $\mathbf{c}$ is the vector or nonlinear inertial forces.

Because of presence of dependent coordinates, equation of motion (1.5) is subjected to the geometric constraints (1.3). Thus dynamic equation (1.5) with algebraic condition (1.3) forms a Differential Algebraic Equation. The numerical integration of DAEs is much more complex than a simple ODE [31]. The problem is caused by the unkown algebraic variable $\boldsymbol{\lambda}$. It seems straigthforward to use the Udwadia-Kalaba multibody method [32] when Lagrange multipliers do not appear. However, in that case the constraint relations are formulated at the acceleration level and due to the numerical integration the constraint equations can not be satisfied precisely.

In the solution of the DAE problem the analysis of differentiation index can help for the categorization. The differentiation index can be constructed using different definitions. For example, in order to find consistent initial value, it is often necessary to consider the derivatives of some of the component functions of the DAE. The highest order of a derivative that is necessary in this process is called the differentiation index [31]. Otherwise based on reference [33], the differentiation

index is equal to the minimal number of differentiations of the constraints in order to get an ODE problem for all of the variables. Using the Lagrange equation of motion, when holonomic (geometric) constraints are applied, this index is 3. There are many methods and schemes that are used for the numerical integration of DAE-s applied in mechanical systems. Some well known methods are briefly introduced in the following sections.

1.2 Numerical solution techniques

There are approaches for the numerical solution of the system (1.5) and (1.3). One keeps the original descriptor coordinates, and the other one reduces the coordinates with appropriate selection or transformations. In all of the methods, the key task is to handle (eliminate or express) the algebraic variable $\boldsymbol{\lambda}$, namely the unknown constraint-forces.

Original coordinate set

Keeping the original coordinates descriptor coordinates the Lagrange multiplier can be eliminated with the relaxation of the constraint forces, as performed in the penalty method [14], [34], [35]. The penalty method replaces a constrained problem by a series of unconstrained problems whose solutions ideally converge to the solution of the original constrained problem. The problem with the penalty methods is that they require the use of large penalty numbers and high stiffness terms to keep the constraint violation at a satisfactory level. These penalty terms will make the equations stiff and will introduce numerical problems.

In the method of Lagrange multipliers [14] the constraints are considered on the acceleration level for the expression of the differential variable $\boldsymbol{\lambda}$ practically for the expression of the constraint forces.

The method proposed in [14], [36] keeps the original coordinates and it decomposes the admissible and constrained directions. The common point of these methods is the index reduction because their transforms a DAE with differentiation index-3 into an index-1 DAE system.

Newly introduced coordinate set

In [37] and [36] a coordinate transformation is carried out. With this step the unknown constraint forces will be eliminated.

In general it is easier to introduce the independent variables at velocity level [36]. The introduction of new independent generalized coordinates could be complicated in many cases due to the nonlinear position level transformation. An alternative possibility is the coordinate partitioning method which is originally introduced by Wehage and Haug in [38], when the independent coordinates are selected from the dependent set of coordinates. The method leads to a minimum set of constraint reaction-free dynamic equations in terms of the independent coordinates. In addition, the differential variables $\boldsymbol{\lambda}$ can also be determined. Since the coordinates depend on the configuration in [39], a special procedure, the so-called projective criterion is given for the selection of coordinates in order to enhance the computational efficiency.

In the subsequent sections the applied methods of this work will be summarized briefly: the transformation to the independent coordinates; the method of Lagrangian multipliers; and the coordinate partitioning method.

1.2.1 Formulation with independent coordinates

The DAE equation motion (1.5) together with (1.3) can be reformulated in the space of independent coordinates as it is presented in [36]. The coordinate transformation can be done using the following steps. The connection between the kinematic variations in the space of minimum (independent) set $\mathbf{p}$ and non-minimum (dependent) set of generalized velocities can be written as

$$\delta\dot{\mathbf{q}} = \mathbf{B}(\mathbf{q})\delta\dot{\mathbf{p}}(\mathbf{q}), \tag{1.6}$$

where the Jacobian matrix $\mathbf{B}$ can be constructed as the function of the independent coordinates. With this transformation the virtual power of the system (1.5) can be written as

$$\delta\dot{\mathbf{p}}^{\mathrm{T}}\mathbf{B}^{\mathrm{T}}(\mathbf{M}(\dot{\mathbf{B}}\dot{\mathbf{p}} + \mathbf{B}\ddot{\mathbf{p}}) + \mathbf{c} + \boldsymbol{\Phi}^{\mathrm{T}}\boldsymbol{\lambda} - \mathbf{Q}) = 0\,. \tag{1.7}$$

Since $\delta\dot{\mathbf{p}}$ can be considered as an independent kinematic variation, the constraint force are eliminated with the transformation of the forces the equation of motion as:

$$\mathbf{B}^{\mathrm{T}}\mathbf{M}\mathbf{B}\ddot{\mathbf{p}} + \mathbf{M}\mathbf{B}\dot{\mathbf{p}} + \mathbf{B}^{\mathrm{T}}\mathbf{c} = \mathbf{B}^{\mathrm{T}}\mathbf{Q}\,. \tag{1.8}$$

The above formula (1.8) is an ordinary differential equation which can be directly used for the numerical simulation.

The main difference between the coordinate partitioning [38] technique and the above summarized method is that in case of the coordinate partitioning technique new coordinates are selected from the original coordinates using the constraint equations, whereas here partly or entirely new set of coordinates are introduced. Despite both method can be used generally, both of them require further non-unique intuitive steps during the transformation.

Similar to the selection of the dependent set of coordinates $\mathbf{q}$, the selection of the independent set of coordinates $\mathbf{p}$ is also intuitive. This intuitive selection can be quite complex especially in closed-loop mechanisms.

1.2.2 Method of Lagrange multipliers

One commonly used technique for the solution of a DAE problem is the so-called method of Lagrange multipliers [14]. The dimension of generalized coordinates is n, and the dimension of the equation (1.5) is also n, and it contains n differential variables and further m algebraic unknowns, namely the Lagrange multipliers. Equation (1.5) is augmented by additional m constraint equations (1.3). In general an index-1 DAE problem is solvable [33]. Thus, in case of geometric constraints, when the DAE index is three, a second order index reduction is required, which can be achieved by the direct time differentiation of the constraints (1.3) twice. For this the constraint equation at the acceleration level can be written as

$$\ddot{\boldsymbol{\varphi}} \equiv \boldsymbol{\Phi}\ddot{\mathbf{q}} + \dot{\boldsymbol{\Phi}}\dot{\mathbf{q}} + \dot{\boldsymbol{\pi}} = \mathbf{0}, \tag{1.9}$$

where $\boldsymbol{\pi} = \partial\boldsymbol{\varphi}/\partial t$. Equation (1.5) and (1.9) can be combined as

$$\begin{bmatrix} \mathbf{M} & \boldsymbol{\Phi}^{\mathrm{T}} \\ \boldsymbol{\Phi} & \mathbf{0} \end{bmatrix} \begin{bmatrix} \ddot{\mathbf{q}} \\ \boldsymbol{\lambda} \end{bmatrix} = \begin{bmatrix} \mathbf{Q} \\ -\dot{\boldsymbol{\Phi}}\dot{\mathbf{q}} - \dot{\boldsymbol{\pi}} \end{bmatrix}. \tag{1.10}$$

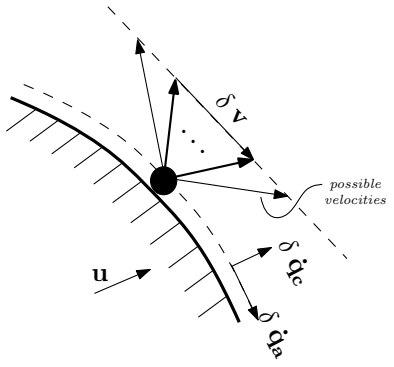

FIGURE 1.3. Velocity components associated with the constrained and admissible directions

Now we have the same number of equations $(n+m)$ as unknowns $(n+m)$. The leading matrix is symmetrical (if $\mathbf{M}$ is symmetrical) and can be very sparse in many practical cases. From equation (1.10) the accelerations $\ddot{\mathbf{q}}$ and a Lagrange multipliers $\boldsymbol{\lambda}$ can be expressed. Since equation (1.9) is an unstable equation and round-off errors appear during the integration, the position and velocity level constraints will not be perfectly satisfied. Therefore the numerical integration needs stabilization.

Stabilization of constraints

The best known and practical idea for the stabilization of the constraints is the so called Baumgarte [40] stabilization technique when the constraint condition at the acceleration level (1.9) is augmented with linear spring- and damper-like terms

$$\ddot{\boldsymbol{\varphi}} + 2\alpha\,\dot{\boldsymbol{\varphi}} + \beta^2\,\boldsymbol{\varphi} = 0, \tag{1.11}$$

where α and β are appropriately chosen constants. By using (1.11) instead of (1.9) the equation (1.10) can be written as

$$\begin{bmatrix} \mathbf{M} & \boldsymbol{\Phi}^{\mathrm{T}} \\ \boldsymbol{\Phi} & \mathbf{0} \end{bmatrix} \begin{bmatrix} \ddot{\mathbf{q}} \\ \boldsymbol{\lambda} \end{bmatrix} = \begin{bmatrix} \mathbf{Q} \\ -\dot{\boldsymbol{\Phi}}\dot{\mathbf{q}} - \dot{\boldsymbol{\pi}} - 2\alpha\,\dot{\boldsymbol{\varphi}} - \beta^2\,\boldsymbol{\varphi} \end{bmatrix}. \tag{1.12}$$

Reference [14] suggests that the Baumgarte parameters should be the same and should be between $5-20$. In [41] a detailed study is provided for the selection of Baumgarte parameters. The Baumgarte stabilization is general, easy to implement and numerically efficient. Its computational cost is a small fraction of the total computational time. Furthermore it does not fail near singular configurations or in the presence of redundant constraints.

The introduced artificial spring and damper can influence the motion in the non-constrained directions as well, which can be incorrect. Despite this potential problems the simplicity of the method makes it a widespread technique.

In order to overcome the numerical instability, in the method of Lagrange multipliers there are numerical schemes for mixed systems which allow to adding the algebraic equations to the DAE system (1.10) like in [42]. However these techniques are not used widely because they are computationally expensive and usually they have an over-damping effect.

1.2.3 Projection into admissible and constrained motion spaces

A possible approach [36], which also result the equation of motion in index-1 form, is based on the separation of generalized virtual velocity $\delta\dot{\mathbf{q}}$ into admissible part $\delta\mathbf{q}_a$, and constrained part $\delta\dot{\mathbf{q}}_c$, generalized velocities as

$$\delta\dot{\mathbf{q}} = \delta\dot{\mathbf{q}}_a + \delta\dot{\mathbf{q}}_c. \tag{1.13}$$

These directions are depicted in Fig. 1.3. The geometrical interpretation of this separation is explained in more detail in [43].

The elements of these vectors can be constructed based on the constraint Jacobian Φ because the Jacobian is orthogonal to the subspace defined by the constraints. Vectors $\delta\dot{\mathbf{q}}_a$ and $\delta\dot{\mathbf{q}}_c$ are the linear combination of the original virtual velocity $\delta\dot{\mathbf{q}}$. By means of algebraic calculations, the following assumption can be easily deduced as

$$\delta\dot{\mathbf{q}} = (\mathbf{I} - \mathbf{\Phi}^{\dagger}\mathbf{\Phi})\delta\dot{\mathbf{q}} + \mathbf{\Phi}^{\dagger}\mathbf{\Phi}\delta\dot{\mathbf{q}}, \tag{1.14}$$

where $\mathbf{\Phi}^{\dagger}\mathbf{\Phi}$ gives the projection onto the constrained directions and as a complement $\mathbf{I}-\mathbf{\Phi}^{\dagger}\mathbf{\Phi}$ defines the projection into the admissible directions. In (1.14) $\mathbf{\Phi}^{\dagger}$ is the Moore-Penrose pseudoinverse of $\mathbf{\Phi}$. The Moore-Penrose pseudoinverse [44] is a generalized inverse which is quite common in robotics, but it is based on a purely mathematical concept. In order to preserve physical consistency during the numerical calulations the mass matrix may be employed as the metric for the tangent space of the configuration manifold. Based on [36] and [44] the generalized inverse can be derived as

$$\mathbf{\Phi}^{\dagger} = \mathbf{M}^{-1}\mathbf{\Phi}^{\mathrm{T}}(\mathbf{\Phi}\mathbf{M}^{-1}\mathbf{\Phi}^{\mathrm{T}})^{-1}. \tag{1.15}$$

This expression uses physical considerations in order to avoid operations with different units. This is the reason why the mass matrix $\mathbf{M}$ appears in the calculation. In the following

$$\mathbf{P}_a = \mathbf{I} - \mathbf{\Phi}^{\dagger}\mathbf{\Phi} \tag{1.16}$$

will be considered as a projection operator which projects into admissible directions. The following operator projects into the constrained direction

$$\mathbf{P}_c = \mathbf{\Phi}^{\dagger}\mathbf{\Phi}. \tag{1.17}$$

In algebraic point of view it means that $\mathbf{P}_a$ projects into the nullspace of the constraint Jacobian $\mathbf{\Phi}$. The principle of the virtual power can be expressed from the equation of motion (1.5)

$$\delta\dot{\mathbf{q}}^{\mathrm{T}}(\mathbf{M}\ddot{\mathbf{q}} + \mathbf{\Phi}^{\mathrm{T}}\boldsymbol{\lambda} + \mathbf{c} - \mathbf{Q}) = 0. \tag{1.18}$$

By substituting the decomposition (1.13) into (1.18) the equation of motion reads as

$$\delta\dot{\mathbf{q}}_a^{\mathrm{T}}(\mathbf{M}\ddot{\mathbf{q}} + \mathbf{\Phi}^{\mathrm{T}}\boldsymbol{\lambda} + \mathbf{c} - \mathbf{Q}) + \delta\dot{\mathbf{q}}_c^{\mathrm{T}}(\mathbf{M}\ddot{\mathbf{q}} + \mathbf{\Phi}^{\mathrm{T}}\boldsymbol{\lambda} + \mathbf{c} - \mathbf{Q}) = 0. \tag{1.19}$$

Since in the constrained direction the virtual velocity $\mathbf{q}_c$ necessarily satisfies the constraints, the variation of it is zero and consequently the second part of (1.19) is identically zero. Thus the

equation of motion in the admissible space reads as

$$\delta\dot{\mathbf{q}}^{\intercal}\mathbf{P}_a^{\mathrm{T}}(\mathbf{M}\ddot{\mathbf{q}} + \mathbf{\Phi}^{\mathrm{T}}\boldsymbol{\lambda} + \mathbf{c} - \mathbf{Q}) = 0. \tag{1.20}$$

The admissible virtual velocities are orthogonal to the constraint forces, thus these forces have no virtual power. Thus after the elimination of the algebraic variable $\boldsymbol{\lambda}$ the equation of motion can be written as

$$\mathbf{P}_a^{\mathrm{T}}\mathbf{M}\ddot{\mathbf{q}} + \mathbf{P}_a^{\mathrm{T}}\mathbf{c} - \mathbf{P}_a^{\mathrm{T}}\mathbf{Q} = \mathbf{0}. \tag{1.21}$$

The direct inversion (for the expression of accelerations) of the projected equation (1.21) is not straightforward because the matrix $\mathbf{P}_a^{\mathrm{T}}\mathbf{M}$ is singular. In order to handle the singularity, first we have to further elaborate the first term $\mathbf{P}_a^{\mathrm{T}}\mathbf{M}$ of (1.21) using the generalized pseudoinverse (1.15)

$$\mathbf{P}_a^{\mathrm{T}}\mathbf{M}\ddot{\mathbf{q}} = \mathbf{M}\ddot{\mathbf{q}} - (\mathbf{\Phi}\mathbf{M}^{-1}\mathbf{\Phi}^{\mathrm{T}})^{-\intercal}\mathbf{\Phi}\mathbf{M}^{-\intercal}\mathbf{M}\ddot{\mathbf{q}}. \tag{1.22}$$

Using the equation on the acceleration level constraint equation(1.9) the projection of the inertial forces finally reads as

$$\mathbf{P}_a^{\mathrm{T}}\mathbf{M}\ddot{\mathbf{q}} = \mathbf{M}\ddot{\mathbf{q}} - (\mathbf{\Phi}\mathbf{M}^{-1}\mathbf{\Phi}^{\mathrm{T}})^{-\intercal}(-\dot{\mathbf{\Phi}}\dot{\mathbf{q}} - \mathbf{\Phi}_t). \tag{1.23}$$

With this expansion the equation of the admissible motion can be derived in the following form

$$\mathbf{M}\ddot{\mathbf{q}} - (\mathbf{\Phi}\mathbf{M}^{-1}\mathbf{\Phi}^{\mathrm{T}})^{-\intercal}(-\dot{\mathbf{\Phi}}\dot{\mathbf{q}} - \mathbf{\Phi}_t) + \mathbf{P}_a^{\mathrm{T}}\mathbf{c} - \mathbf{P}_a^{\mathrm{T}}\mathbf{Q}_{ex} = \mathbf{0}. \tag{1.24}$$

Because in Eq. (1.24) the constraint equations are considered at the level of acceleration it is necessary to ensure the fulfilment of the constraint equations. In [36] a simple projection based configuration and velocity correction is proposed after each integration step. The advantage of the applied method is that using the non-minimum set of descriptor coordinates the terms has a simple structure and their elements can often be derived in closed form. It also needs some control process for satisfying the constraints at position and velocity levels, but there is no need for tuning of additional parameters for stabilizing the constraints during integration.

Chapter 2

Underactuated mechanical systems

Underactuated systems form a class of mechanical systems in robotics and control theory. As a fundamental definition an underactuated system has fever number of independent actuators than the degrees of freedom n [45]. In this case, the system is said to be trivially underactuated [2]. Besides the trivially underactuated systems other control problems can be modelled as underactuation like joint flexibility or saturation, as it will be shown later.

2.1 Possibilities for the characterisation of underactuated systems.

The need for the categorization of different problems in order to choose the most appropriate tool or technique is common in every field of science. It is true for underactuated systems as well. In the followings, an overview will be given on the possible categorizations and analyzing approaches.

2.1.1 Input-output location

Based on the spatial location of the actuators and the controlled coordinates *collocated* and *non-collocated* underactuated systems are distinguished [45], [46].

For several manipulators the joints can be partitioned unequivocally into active $\mathbf{q}_a$, and passive $\mathbf{q}_p$, sets (see Fig. 2.1). This is an actuation based separation.

During the control-task based separation coordinates are separated into controlled $\mathbf{q}_c$ and uncontrolled ones $\mathbf{q}_u$. The time history of the controlled coordinates are explicitly specified in the control task, while there isn't any prescription for the uncontrolled coordinates.

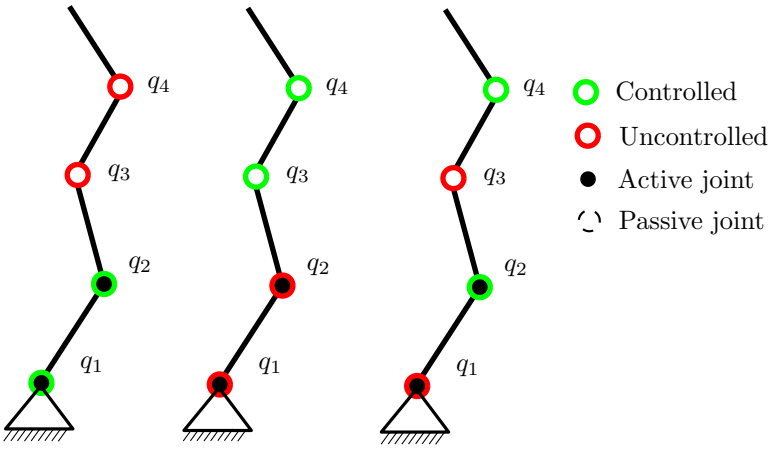

FIGURE 2.1. Collocated case (left) , Non-collocated case (centre), Mixed case (right)

If $\mathbf{q}_a \equiv \mathbf{q}_c$ and $\mathbf{q}_p \equiv \mathbf{q}_u$, the system has collocated output. If $\mathbf{q}_p \equiv \mathbf{q}_c$ and $\mathbf{q}_a \equiv \mathbf{q}_u$, the system is called non-collocated as it is seen in Fig. 2.1. Physically it means that the output have to be associated only with the active or only with the passive joints. If the output is related to both the passive and active joints, this separation is not possible. Furthermore in many cases the coordinate separation to active and passive ones is difficult or not possible.

2.1.2 Input-output dependence

A more systematic categorization technique uses the differentiation order of dependence between the inputs and the outputs. It is the so called relative degree [47] [20].

For the presentation the concept of relative degree, let us consider a general multiple input - multiple output (MIMO) control system:

$$\dot{\mathbf{x}} = \mathbf{f}(\mathbf{x}) + \mathbf{g}(\mathbf{x})\mathbf{u}, \tag{2.1}$$

where $\mathbf{x} = [\mathbf{q}, \dot{\mathbf{q}}]^{\mathrm{T}}$ is a state space vector. If we formulate the equation with independent coordinates, the dimension of the state $\mathbf{x} \in \mathbb{R}^{2g}$.

The output $\mathbf{y} \in \mathbb{R}^{l}$ that corresponds to the desired task is described by the function:

$$\mathbf{y} = \mathbf{h}(\mathbf{x}). \tag{2.2}$$

The relative degree r_i for the i^{th} output $y_i(\mathbf{x})$ means the minimum number of time differentiation for which any element of the output $\mathbf{u}$ appear explicitly in the differentiated output [20]. Mathematically the series of differentiations can be formulated with the so-called Lie derivatives (directional derivative)[48]. Using equation (2.1) of the controlled system, the total time derivative of the output function (2.2) can be written as

$$\dot{\mathbf{y}} = \frac{\mathrm{d}\mathbf{h}(\mathbf{x})}{\mathrm{d}\mathbf{x}}\dot{\mathbf{x}} = \frac{\mathrm{d}\mathbf{h}(\mathbf{x})}{\mathrm{d}\mathbf{x}}\mathbf{f}(\mathbf{x}) + \frac{\mathrm{d}\mathbf{h}(\mathbf{x})}{\mathrm{d}\mathbf{x}}\mathbf{g}(\mathbf{x})\mathbf{u}. \tag{2.3}$$

After differentiating the output r_i times, the control input $\mathbf{u}$ appears, as it can be seen here

$$\begin{aligned}
y_i &= h_i(\mathbf{x}) \\
\dot{y}_i &= \frac{\mathrm{d}h_i(\mathbf{x})}{\mathrm{d}\mathbf{x}}\mathbf{f}(\mathbf{x}) \\
\ddot{y}_i &= \frac{\mathrm{d}^2 h_i(\mathbf{x})}{\mathrm{d}\mathbf{x}^2}\mathbf{f}^2(\mathbf{x}) \\
&\vdots \\
y_i^{(r_i-1)} &= \frac{\mathrm{d}^{r_i-1} h_i(\mathbf{x})}{\mathrm{d}\mathbf{x}^{r_i-1}}\mathbf{f}^{r_i-1}(\mathbf{x}) \\
y_i^{(r_i)} &= \frac{\mathrm{d}^{r_i} h_i(\mathbf{x})}{\mathrm{d}\mathbf{x}^{r_i}}\mathbf{f}^{r_i}(\mathbf{x}) + \frac{\mathrm{d}^{r_i} h_i(\mathbf{x})}{\mathrm{d}\mathbf{x}^{r_i}}\mathbf{g}(\mathbf{x})\mathbf{u}
\end{aligned} \tag{2.4}$$

For brevity let us use the following notations

$$L_f\mathbf{h}(\mathbf{x}) = \frac{\mathrm{d}\mathbf{h}(\mathbf{x})}{\mathrm{d}\mathbf{x}}\mathbf{f}(\mathbf{x}) \quad \text{and} \quad L_g\mathbf{h}(\mathbf{x}) = \frac{\mathrm{d}\mathbf{h}(\mathbf{x})}{\mathrm{d}\mathbf{x}}\mathbf{g}(\mathbf{x}). \tag{2.5}$$

With this notations the input output relationship can be written in the following compact form

$$y_i^{(r_i)} = L_f^{r_i}\mathbf{h}(\mathbf{x}) + L_g L_f^{r_i-1}\mathbf{h}(\mathbf{x})\mathbf{u}. \tag{2.6}$$

Practically this systematic calculation process results in the method of partial feedback linearization [20]. In case of MIMO systems this calculation have to be carried out for all outputs y_i; $i = 1 \dots l$. The relative degree vector $\mathbf{r} = [r_1, \dots, r_l]$, represents the relation between the inputs and outputs. If the derivatives for all outputs are calculated, an input-output normal form can be constructed and a new state variables $\mathbf{z} = [y_1, \dot{y}_1, \cdots y_1^{(r_1)} \dots y_l, \dot{y}_l \cdots y_l^{(r_l)}]^{\mathrm{T}}$ can be introduced. With this transformation the feedback law can be constructed [20, 47] in order to eliminate to non-linearities of a general dynamical system.

The relative degree analysis helps us to understand how the input is related with the desired task (desired variable) as it will be used later. Controlled systems can be categorized based on their largest relative degree.

2.1.3 Unobservable states

In the field of underactuated systems, it is quite common to use the notion of *internal dynamics* [20] and investigate its behaviour. In order to understand the meaning of internal dynamics, we take a general n dimensional dynamical system. If we have a one dimensional output y, based on expression (2.4), the control problem can be described with r number of states. Hence, if $r < n$, then $r - n$ number of states is not required for the exact definition of the output. The states of the internal dynamics are denoted with $\boldsymbol{\eta} = [\eta_1, \dots, \eta_{n-r}]^{\mathrm{T}}$. If there is internal dynamics ($r < n$), the full state input-output linearisation is not possible. Therefore, a part of the system dynamics (described by $\boldsymbol{\eta}$) does not appear among the control goals, because these *unobservable* states cannot be seen from the external input-output relationship. This part of the dynamics will be called as *internal dynamics* [20]. For the clarification, it have to be noted that these unobservable states have to be also measured for the control. To generalize the concept of internal dynamics to multiple output ($y \in \mathbb{R}^l$) system let us summarize the elements (taxicab norm) of the relative degree vector $\mathbf{z} = [y_1, \dot{y}_1, \cdots y_1^{(r_1)} \dots y_l, \dot{y}_l \cdots y_l^{(r_l)}]^{\mathrm{T}}$ as

$$\widetilde{r} = ||\mathbf{r}||_1 = \sum_{i=1}^{l} r_i. \tag{2.7}$$

In this case the internal dynamics exists if $\widetilde{r}$ is less than the dimension of the state vector $\mathbf{x}$ (2.1).

In the thesis the dimension of the input $\mathbf{u}$ is l and the task (output) is also l dimensional for the investigated applications. For most of the problems in the thesis the relative degree vector of the system is $\mathbf{r} = [2, \dots, 2]^{\mathrm{T}}$. In that cases the number of unobservable states is $2\,j = 2\,g - 2\,l$, where g represents the DoF. Physically it means that j number of coordinates and the corresponding velocities can describe the state of the internal dynamics.

Again, the internal dynamics is a special part of the dynamics that cannot be seen in the external input-output relationship. It is a similar to the definition of flatness systems in nonlinear control theory [20, 49]. Flatness is an extension of controllability from linear systems to nonlinear systems. A system is differentially flat when the system has flat output. With a flat output all states of the system can be expressed with finite number of derivations. Using the notion of internal dynamics a system is differentially flat when there is no internal dynamics.

The task of the control design is to ensure the stability of the whole systems. This means that the unobservable states have to be bounded. Thus the system can be stabilized if the internal dynamics is stable. A dynamical system (2.1) can be minimum-phase at an equlibirium point $\mathbf{x}_0$ if the zero dynamics in $\boldsymbol{\eta} = \mathbf{0}$ is exponentially stable. Otherwise it is called non-minimum phase [1], [50]. The internal dynamics is called *zero dynamics* if there is an initial condition $\mathbf{x}_0$ and control $\mathbf{u}$ with which the system output $\mathbf{y} = \mathbf{h}(\mathbf{x})$ is kept constant. Physically it means that the output can be kept constant independently from the internal dynamics.

It have to be noted that the internal dynamics and its stability depend on the choice of the output function (2.2).

2.1.3.1 Representative example

For the demonstration of the relative degree analysis, an underactuated benchmark example is studied in the followings. This simple problem can be used to understand the physical background of several control problems such as control of flexible robot manipulators [13]. This linear underactuated system contains two blocks connected by a spring as shown in Fig. 2.2. Two studies are carried out in case of this example. The first one analyzes the collocated control and second one analyzes the non-collocated problem (see in Sec. 2.1.1).

For the dynamical modelling, the absolute displacement of the blocks are chosen as general coordinates $\mathbf{q} = [x_1,\ x_2]^{\mathrm{T}}$.

The equation of motion can be easily deduced as

$$\begin{bmatrix} m_1 & 0 \\ 0 & m_2 \end{bmatrix} \begin{bmatrix} \ddot{x_1} \\ \ddot{x_2} \end{bmatrix} + \begin{bmatrix} k(x_1 - x_2) \\ k(x_2 - x_1) \end{bmatrix} = \begin{bmatrix} 1 \\ 0 \end{bmatrix} F. \tag{2.8}$$

In case of the collocated control the the first block of the system is controlled and the output is given as

$$y = x_1, \tag{2.9}$$

where $\mathbf{q}_a \equiv \mathbf{q}_c = [x_1]$, $\mathbf{q}_p \equiv \mathbf{q}_u = [x_2]$.

The relation between the $l = 1$ dimensional input $\mathbf{u} = [F]$ and the output can be defined with the differentiation of the output (2.9) similar to the expressions in (2.4) as

$$\underbrace{\begin{bmatrix} \dot{y} \\ \ddot{y} \end{bmatrix}}_{\mathbf{z}} = \underbrace{\begin{bmatrix} \dot{x}_1 \\ (F - k(x_1 - x_2))/m_1 \end{bmatrix}}_{\boldsymbol{\chi}(\mathbf{q}, \dot{\mathbf{q}})}. \tag{2.10}$$

In this case the control input F appears in the second derivative of the output and the dimension of the controlled states $\mathbf{z}$ is 2, thus the sum of elements of the relative degree vector $\widetilde{r} = 2$. Since the state vector $\mathbf{x} = [\mathbf{q}, \dot{\mathbf{q}}]^{\mathrm{T}}$ of the system is 4-dimensional, internal dynamics is present in this control task.

The second scenario when the motion of the second block is controlled it is called non-collocated case (see in Sec. 2.1.1). Here the output can be written as

$$y = x_2 \tag{2.11}$$

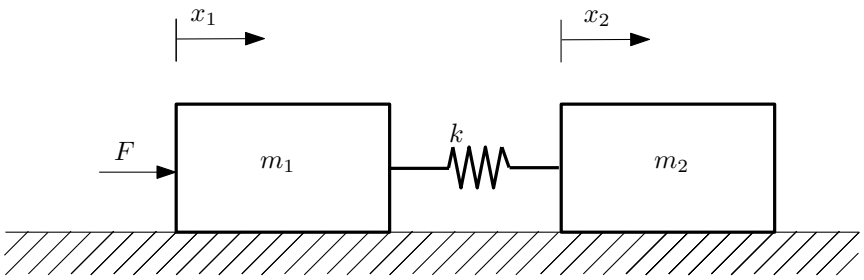

FIGURE 2.2. Control of a two-mass problem

Along the lines of Eq. (2.4) the relation between the input and the output can be expressed as

$$\underbrace{\begin{bmatrix} \dot{y} \\ \ddot{y} \\ \dddot{y} \\ y^{IV} \end{bmatrix}}_{\mathbf{z}} = \underbrace{\begin{bmatrix} \dot{x}_2 \\ k(x_1 - x_2)/m_2 \\ k(\dot{x}_1 - \dot{x}_2)/m_2 \\ k(\frac{F+k(x_2-x_1)}{m_1} - \ddot{x}_2)/m_2 \end{bmatrix}}_{\boldsymbol{\chi}(\mathbf{q},\dot{\mathbf{q}})}, \tag{2.12}$$

Here input F appears first in the fourth time derivative of the output. Thus the relative degree sum $\widetilde{r} = 4$ in this control problem (see Eq. (2.7)). In [51] it is called pure tangential realisation of the servo-constraints. Based on the definition of the internal dynamics (see Sec. 2.1.3) there is no internal dynamics here and the problem is differentially flat [49]. Using an other terminology and assuming that both manifolds are smooth the Eq. 2.12 is a diffeomorphic coordinate transformation [52] while from $\mathbf{z} = \boldsymbol{\chi}(\mathbf{q}, \dot{\mathbf{q}})$ equation with knowing $\mathbf{z}$ all elements of the state $(\mathbf{q}, \dot{\mathbf{q}})$ can be expressed.

Despite the output can expressed directly from (2.12) it has practical drawbacks. Here the first requirement is that the desired path have to be C^4 continuous, which is easily feasible. But in order to carry out a stable controller the second and the third derivatives have to be measured, which is hardly feasible in a real robotic system. In the later sections such systems will be analyzed when there is internal dynamics and their relative degree is 2 for all input-output pairs $\mathbf{r} = [2, \ldots, 2]^{\mathrm{T}}$.

2.2 Inverse dynamics for trajectory tracking control

It is quite common to use the solution of the inverse dynamics problems in trajectory tracking control of fully actuated manipulators. From the inverse dynamics calculation the required forces or torques can be calculated. The inverse dynamics calculations mostly referred as Computed Torque Control (CTC) [13, 24].

The equation of motion of a general controlled mechanical system is given in the following form

$$\mathbf{M}(\mathbf{q})\ddot{\mathbf{q}} + \mathbf{c}(\mathbf{q}, \dot{\mathbf{q}}) = \mathbf{Q}(\mathbf{q}) + \mathbf{H}(\mathbf{q})\mathbf{u} \,. \tag{2.13}$$

The desired variables $\mathbf{q}_{\mathrm{d}}$, $\dot{\mathbf{q}}_{\mathrm{d}}$, $\ddot{\mathbf{q}}_{\mathrm{d}}$ are determined from the prescribed task (2.2). We assume that control input matrix $\mathbf{H}$ is a square matrix and invertible, so the nominal value of required control input can be expressed as

$$\mathbf{u}_{\mathrm{n}} = \mathbf{H}(\mathbf{q}_{\mathrm{d}})^{-1}\Big(\mathbf{M}(\mathbf{q}_{\mathrm{d}})\ddot{\mathbf{q}}_{\mathrm{d}} - \mathbf{c}(\mathbf{q}_{\mathrm{d}}, \dot{\mathbf{q}}_{\mathrm{d}}) - \mathbf{Q}(\mathbf{q}_{\mathrm{d}})\Big) \,. \tag{2.14}$$

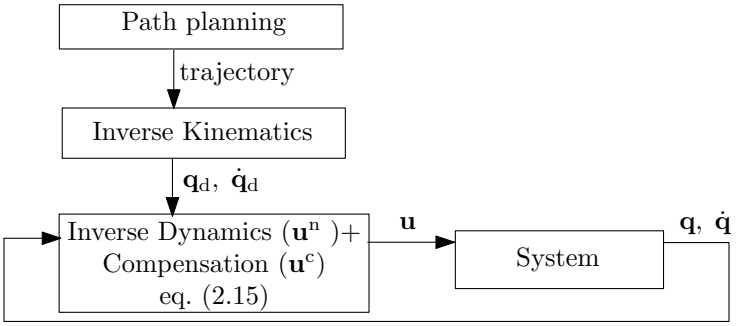

FIGURE 2.3. Scheme of inverse dynamics control in fully-actuated case

The modelling errors and disturbances can be eliminated with an additional simple linear compensator like a proportional-derivative (PD) controller [13] as

$$\mathbf{u} = \mathbf{u}_\mathrm{n} + \mathbf{u}_\mathrm{c},\ \text{where}\ \ \mathbf{u}_\mathrm{c} = \mathbf{H}(\mathbf{q}_\mathrm{d})^{-1}(\mathbf{q}_\mathrm{d})\Big(\mathbf{K}_\mathrm{p}(\mathbf{q}_\mathrm{d} - \mathbf{q}) - \mathbf{K}_\mathrm{d}(\dot{\mathbf{q}}_\mathrm{d} - \dot{\mathbf{q}}))\Big)\ . \tag{2.15}$$

The result of Eq. (2.15) is identical with the feedback linearization [13]. The operation of the control is visualized in Fig. 2.3.

2.2.1 Inverse dynamics for underactuated systems

Let us consider (2.13) again. The rank of matrix $\mathbf{H}$ is equal to the number of independent actuators which is l. Because in case of an underactuated system the number of the independent actuators is less than the degrees-of-freedom ($l < g$) $\mathbf{H}$ is a rank deficient matrix and the inverse dynamics (2.14) cannot be computed directly as in Eq. (2.14). In the control definition, we suppose that the dimension of the task (2.2) is equal to number of inputs l which is less than the degrees of freedom. Therefore the solution of the inverse kinematics is not unique and it is not possible to determine all of the values of the desired variables $\mathbf{q}_\mathrm{d},\ \dot{\mathbf{q}}_\mathrm{d},\ \ddot{\mathbf{q}}_\mathrm{d}$ based on pure kinematic equations.

There are extensions of CTC method for underactuated systems in the literature. One possibility is to use the so-called partial feedback linearisation [45]. An other method is called Computed Reference Computed Torque Control (CRCTC) [46]. In this method the coordinates are separated to controlled and uncontrolled ones. The desired value of the controlled coordinates are known from the task and the method calculates a desired value for the uncontrolled coordinates on-line. With the computed desired values for uncontrolled coordinates the inverse dynamics problem can be solved. The main drawback of the CRCTC method is that the equation of motion have to be formulated with minimum set of coordinates which may be disadvantageous in complex systems.

In case of dependent set of coordinates, it is a useful approach to use the so-called servo-constraints [15, 53, 54] for describing the desired task. They are also called as control or program constraint [18]. These constraints are mathematically equivalent to the geometric constraints, however, the fact that they do not belong to physical interconnections of bodies makes an important difference. The servo-constraints, for example can describe the tool-center-point (TCP) [13] trajectory of the robot, and the violation of these constraints is in relation with the tracking error. Let us consider the servo-constraints in the form

$$\boldsymbol{\gamma}(\mathbf{q}, t) = \mathbf{p}(\mathbf{q}) - \mathbf{h}(t) = \mathbf{0}\ , \tag{2.16}$$

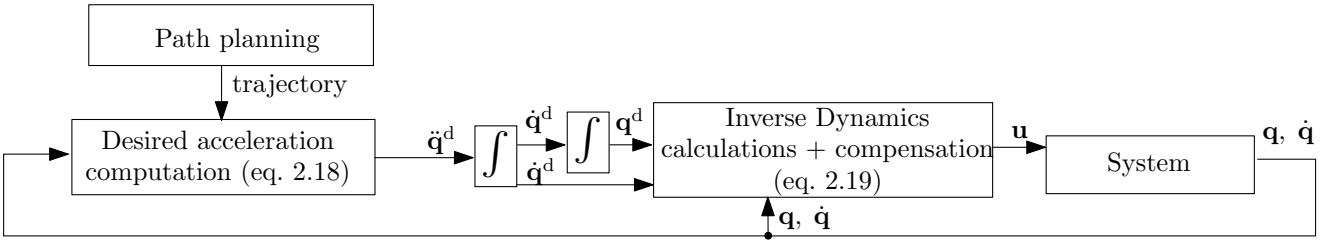

FIGURE 2.4. Scheme of the direct method for underactuated systems

where $\mathbf{p}(\mathbf{q})$ describes the output, e.g., position and orientation of the TCP of a robot, as function of the generalized coordinates, and $\mathbf{h}(t)$ is the desired output with explicit time dependence. Using the idea of the Lagrangian multipliers, similarly to the solution of Eq. (1.10), the servo-constraints can be expressed at the acceleration level too, as follows

$$\ddot{\boldsymbol{\gamma}} = \boldsymbol{\Gamma}(\mathbf{q})\ddot{\mathbf{q}} + \dot{\boldsymbol{\Gamma}}(\mathbf{q})\dot{\mathbf{q}} - \dot{\mathbf{g}}(t)\ , \tag{2.17}$$

where $\boldsymbol{\Gamma} = \partial\mathbf{p}/\partial\mathbf{q}$ is the Jacobian associated with the servo-constraints and $\mathbf{g} = \partial\mathbf{h}/\partial t$. Analogue to the numerical solution of DAE equation, a DAE-index reduction is achieved with the higher order representation of the servo-constraints (see: Sec. 1.2). The calculation of the control force basically have two different ways. In the first method [17, 54] the desired values are determined for all coordinates at position, velocity and at acceleration level as well. In this approach the controlled and non-controlled dynamics have to be separated. Using the equation of motion (2.13) and the servo-constraint equations at the level of acceleration (2.17) the dynamics of the controlled system is described by

$$\begin{bmatrix} \mathbf{N}(\mathbf{q})\,\mathbf{M}(\mathbf{q}) \\ \boldsymbol{\Gamma}(\mathbf{q}) \end{bmatrix} \ddot{\mathbf{q}} = \begin{bmatrix} \mathbf{N}(\mathbf{q})\left(\mathbf{Q}(\mathbf{q}) - \mathbf{c}(\mathbf{q},\dot{\mathbf{q}})\right) \\ \dot{\mathbf{g}}(t) - \dot{\boldsymbol{\Gamma}}(\mathbf{q},\dot{\mathbf{q}})\dot{\mathbf{q}} \end{bmatrix} = \mathbf{0}, \tag{2.18}$$

where matrix $\mathbf{N}$ is orthogonal to the control input matrix $\mathbf{H}$ thus $\mathbf{NH} = \mathbf{0}$. Equation (2.18) gives the prescribed values for the accelerations $\ddot{\mathbf{q}}_{\mathrm{d}}$. From that the desired values for the position $\mathbf{q}_{\mathrm{d}}$ and for the velocity $\dot{\mathbf{q}}_{\mathrm{d}}$ can be integrated on-line in every time step. For the integration of desired variables a backward Euler differentiation scheme is used in several publications [17] [54]. Practically it means we compute the desired values for all DoFs. These are the *computed desired* variables. As a combination of (2.14) and (2.15) using a generalized inverse the required control input can be calculated as in [46]:

$$\mathbf{u} = \left(\mathbf{H}^{\mathrm{T}}\mathbf{H}\right)^{-1}\mathbf{H}^{\mathrm{T}}\left(\mathbf{M}(\mathbf{q}_{\mathrm{d}})\ddot{\mathbf{q}}_{\mathrm{d}} - \mathbf{c}(\mathbf{q}_{\mathrm{d}},\dot{\mathbf{q}}_{\mathrm{d}}) - \mathbf{Q}(\mathbf{q}_{\mathrm{d}}) - \mathbf{K}_{\mathrm{P}}(\mathbf{q}_{\mathrm{d}} - \mathbf{q}) - \mathbf{K}_{\mathrm{D}}(\dot{\mathbf{q}}_{\mathrm{d}} - \dot{\mathbf{q}})\right)\ . \tag{2.19}$$

The scheme on Fig. 2.4 shows the operation of the method.

The other approach for the calculation of the control force uses the actual "measured" state of the system and desired trajectory. In this approach the calculation of the control force $\mathbf{u}$ similar to the method Lagrange multipliers in Eq. (1.5). Combining the equation of motion (2.13) and the servo-constraint on the level of acceleration level (2.17) we can obtain the following form:

$$\begin{bmatrix} \mathbf{M}(\mathbf{q}) & -\mathbf{H}(\mathbf{q}) \\ \boldsymbol{\Gamma} & \mathbf{0} \end{bmatrix} \begin{bmatrix} \ddot{\mathbf{q}}_{\mathrm{d}} \\ \mathbf{u} \end{bmatrix} = \begin{bmatrix} -\mathbf{c}(\mathbf{q},\dot{\mathbf{q}}) + \mathbf{Q}(\mathbf{q}) \\ -\dot{\boldsymbol{\Gamma}}(\mathbf{q})\dot{\mathbf{q}} + \dot{\mathbf{g}}(t) - \mathbf{K}_{\mathrm{D}}\dot{\boldsymbol{\gamma}}(t) - \mathbf{K}_{\mathrm{P}}\boldsymbol{\gamma}(t) \end{bmatrix}, \tag{2.20}$$

where k_P and k_D terms are the gains of the applied controller. Basically in the controller (2.20)

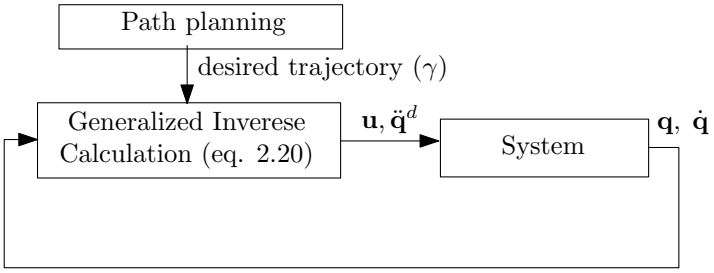

FIGURE 2.5. Scheme of the extension of Computed Torque control for underactuated systems

the term $-\mathbf{K}_\mathrm{D}\dot{\boldsymbol{\gamma}}(t) - \mathbf{K}_\mathrm{P}\boldsymbol{\gamma}(t)$ is the so-called synthetic input [20], while the remaining terms provide enough force to keep the current state of the system $\mathbf{q}, \dot{\mathbf{q}}$.

Here the control inputs $\mathbf{u}$ play a role as the Lagrange multipliers. Equation (2.20) only depends on the measured variables $\mathbf{q}$ and $\dot{\mathbf{q}}$, the given task, and its derivatives $\boldsymbol{\gamma}$ and$\dot{\boldsymbol{\gamma}}$. With this method the scheme of the control is simplified to a simple computed-torque-control shown in Fig. 2.5.

2.2.2 Extension for redundant coordinates

In the field of multibody systems it is quite common to use the non-minimum set of descriptor coordinates. Similarly to equation (2.20) the equation of motion in differentiation index 1 form (1.10) can be extended with the servo-constraints at the acceleration level

$$\begin{bmatrix} \mathbf{M} & \boldsymbol{\Phi}^\mathrm{T} & -\mathbf{H} \\ \boldsymbol{\Phi} & \mathbf{0} & \mathbf{0} \\ \boldsymbol{\Gamma} & \mathbf{0} & \mathbf{0} \end{bmatrix} \begin{bmatrix} \ddot{\mathbf{q}}_\mathrm{d} \\ \boldsymbol{\lambda} \\ \mathbf{u} \end{bmatrix} = \begin{bmatrix} -\mathbf{c} + \mathbf{Q} \\ -\dot{\boldsymbol{\Phi}}\dot{\mathbf{q}} - \dot{\boldsymbol{\pi}} \\ -\dot{\boldsymbol{\Gamma}}\dot{\mathbf{q}} + \dot{\mathbf{g}}(t) - \mathbf{K}_\mathrm{D}\dot{\boldsymbol{\gamma}}(t) - \mathbf{K}_\mathrm{P}\boldsymbol{\gamma}(t) \end{bmatrix}. \tag{2.21}$$

From equation (2.21) the required control force $\mathbf{u}$ can be calculated. Comparing the expression with Eq. (1.12), here the Baumgarte stabilisation is not needed for the geometric constraints . This is because the values of coordinates $\mathbf{q}$ and velocities $\dot{\mathbf{q}}$ are measured and therefore the constraints are naturally satisfied, or at least the constraint error is not accumulating. During the dissertation this control technique will be used in the trajectory tracking problems.

Chapter 3

Stability investigation of multibody systems

Stability analysis has an important role in the control design of multibody systems [37]. This section proposes a stability analysis method of the index-3 DAE problem described by Eq. (1.5)-(1.3). The application procedure of the method for both continuous and discrete time systems is presented.

In the stability analysis, various stability definitions are used or defined depending on the problem. The most used ones in controlled systems are the Bounded Input Bounded Output [55] (BIBO) and the Lyapunov stability theory [56]. When the system is BIBO stable, then the output will be bounded for every input to the system that is bounded. This technique is especially used in linear switched systems.

The Lyapunov theory is treating the stability of solutions near to a point of an equilibrium [33]. Consider the ordinary differential equation with initial condition

$$\dot{\mathbf{x}} = \mathbf{f}(\mathbf{x}, t), \quad \mathbf{x}(0) = \mathbf{x}_0. \quad \text{where } \mathbf{x} \in \mathbb{R}^n \tag{3.1}$$

It is also supposed that $\mathbf{f}$ has an equilibrium at $\mathbf{x}_e$ and $\mathbf{f}(\mathbf{x}_e) = 0$. Then,

1. the equilibrium is said to be Lyapunov stable if for every $\epsilon > 0$, there exist a $\delta > 0$ such that, if $||\mathbf{x}_0 - \mathbf{x}_e|| < \delta$, then for every $t \geq 0$, $||\mathbf{x}(t) - \mathbf{x}_e|| < \epsilon$. The schematic drawing is depicted on Fig. 3.1a.

2. The equilibrium is said to be quasi-asymptotically stable if exists such a $\delta > 0$ that, if $||\mathbf{x}_0 - \mathbf{x}_e|| < \delta$, then for every $t \geq 0$, $\lim_{t\to\infty} ||\mathbf{x}(t) - \mathbf{x}_e|| = 0$. The schematic drawing is depicted on Fig. 3.1b.

An equilibrium is asymptotically stable if it is both Lyapunov and quasi-asymptotically stable as it is drawn on Fig. 3.1c.

In case of a nonlinear differential equation the analytical solution is not known thus the stability of an equilibrium can not be determined. In order to overcome this problem, a scalar energy-like function is constructed and it is called the Lyapunov function. With the Lyapunov function the stability of an equilibrium can be proven [56]. However, in complex problems it is hard to prove that a Lyapunov function exists and is also hard to construct an appropriate function.

In case of a linear system, the stability can be proven easier. The Hartmann-Grobman theorem [57] states that the behavior of a dynamical system in a neighbourhood of a hyperbolic equilibrium

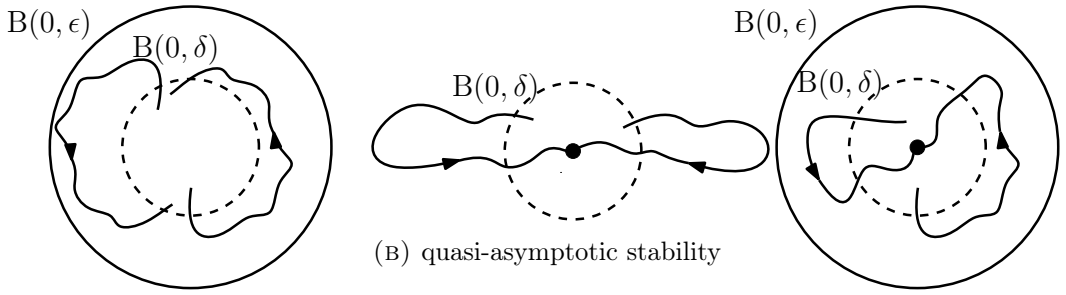

(A) Lyapunov stability (B) quasi-asymptotic stability (C) asymptotic stability

FIGURE 3.1. Stability definitions

point is qualitatively the same as the behavior of its linearization near this equilibrium point. Function $\mathbf{f}$ can be approximated with its Taylor series [58] around $\mathbf{x}_e$. Let us introduce a new variable $\boldsymbol{\xi} = \mathbf{x} - \mathbf{x}_e$ as a perturbation, with which $\dot{\boldsymbol{\xi}} = \dot{\mathbf{x}}$. The i^{th} element of the function can be approximated as

$$\dot{\xi}_i \approx f_i(\mathbf{x}_e) + \sum_{j=1}^{n} \left.\frac{\partial f_i}{\partial x_j}\right|_{\mathbf{x}_e} \xi_j + \text{H.O.T.}, \tag{3.2}$$

where abbreviation H.O.T refers to the higher order terms of the Taylor series. It is generalized for for the whole set of $\boldsymbol{\xi}$. Leave the H.O.T and suppose that $\mathbf{x}_e$ is an equilibrium thus $\mathbf{f}(\mathbf{x}_e) = \mathbf{0}$ and using $\mathbf{x}_e = \mathbf{0}$ assumption (3.2) simplifies as

$$\dot{\boldsymbol{\xi}} = \mathbf{A}\,\boldsymbol{\xi}, \quad \text{where } A_{ij} = \left.\frac{\partial f_i}{\partial x_j}\right|_{\mathbf{x}_e}. \tag{3.3}$$

The $\dot{\boldsymbol{\xi}} = \mathbf{A}\,\boldsymbol{\xi}$ is called the linearization of $\dot{\mathbf{x}} = \mathbf{f}(\mathbf{x})$ at $\mathbf{x} = \mathbf{x}_e$. If $\mathbf{A}$ has n eigenvalues, each of which has strictly negative real part, then $\mathbf{x} = \mathbf{x}_e$ is asymptotically stable [56].

For the analysis of the controlled system the equation of motion have to be linearized around the equilibrium position or the desired trajectory. The linearization of the dynamical system is straightforward, when it is modelled with an ODE as it is discussed in [59]. However, as it is presented before, the governing equation of a multibody system is typically a differential algebraic equation. In this case the eigenvalue analysis is not as straightforward as in case of an ODE. The eigenvalue analysis methods for constrained equations can be mainly divided into two categories.

One possible approach is to transform the original equation of motion into the space of independent coordinates before the eigenvalue analysis [19], [60]. This transformation can be done by the introduction of a new set of independent coordinates as it is presented in [36], or with the partitioning of the coordinates [39]. These reduction based techniques are efficient when the degrees of freedom of the system and the number of constraints are relatively small. In contrast, the reduction into independent coordinates in case of a high dimensional problem is numerically expensive and depends on the configuration.

The other possibility is the direct eigenvalue analysis [61, 62]. A few studies are available where the direct eigenvalue analysis of the constrained dynamic equations are used to analyse the stability and dynamical characteristics, such as vibration frequencies of complex and large deformable mechanical systems [61–63]. In these works, the Lagrange multipliers associated with the constraints are considered as differential variables in the eigenvalue problem. Because of this, spurious eigenvalues appear, beside the physically meaningful ones, and they do not characterize the dynamics of the

investigated system. Reference [62] describes how these spurious eigenvalues are resulted from the algebraic part of the problem and how they can be recognized and isolated using the calculated eigenvectors of the system. These direct linearization techniques use the DAE equation in the original index-3 form, which means that the constraints are considered in the original algebraic form.

3.1 Eigenvalue separation for continuous system

In the followings, a different approach will be presented. In order to eliminate the Lagrange multipliers $\boldsymbol{\lambda}$ the equation of motion (1.5) have to be written in index-1 form as (1.10). As a first step, Eq. (1.10) is reorganized as:

$$\begin{bmatrix} \ddot{\mathbf{q}} \\ \boldsymbol{\lambda} \end{bmatrix} = \begin{bmatrix} \mathbf{f}_1(\mathbf{q}, \dot{\mathbf{q}}, t) \\ \mathbf{f}_2(\mathbf{q}, \dot{\mathbf{q}}, t) \end{bmatrix}. \tag{3.4}$$

In the stability investigation it is enough to deal with function $\mathbf{f}_1$, which describes the dynamics of the system. The state space variables are collected in $\mathbf{x} = [\mathbf{q}, \dot{\mathbf{q}}]^\mathsf{T}$. The first order form of the first set of equations in (3.4) is linearized around the investigated configuration $\mathbf{x}_e = [\mathbf{q}_e, \dot{\mathbf{q}}_e]^\mathsf{T}$. We apply again the small perturbation: $\boldsymbol{\xi} = \mathbf{x} - \mathbf{x}_e$ similarly as in Eq. (3.2). The following form is obtained

$$\begin{bmatrix} \dot{\mathbf{q}} \\ \ddot{\mathbf{q}} \end{bmatrix} = \begin{bmatrix} \dot{\mathbf{q}}_e \\ \mathbf{f}_1(\mathbf{x}_e) \end{bmatrix} + \left[\begin{array}{cc} \mathbf{0} & \mathbf{I} \\ \frac{\partial \mathbf{f}_1(\mathbf{x},t)}{\partial \mathbf{q}} & \frac{\partial \mathbf{f}_1(\mathbf{x},t)}{\partial \dot{\mathbf{q}}} \end{array} \right]\Bigg|_{\mathbf{x}_e} \begin{bmatrix} \mathbf{q} - \mathbf{q}_e \\ \dot{\mathbf{q}} - \dot{\mathbf{q}}_e \end{bmatrix}. \tag{3.5}$$

Since $\mathbf{f}_1(\mathbf{x}_e) = \mathbf{0}$ because $\mathbf{x}_e$ is an equilibrium, Eq. (3.5) can be rewritten in the general form:

$$\dot{\boldsymbol{\xi}} = \mathbf{A}(\mathbf{x}_e)\,\boldsymbol{\xi}, \quad \text{where } \mathbf{A}(\mathbf{x}_e) = \left[\begin{array}{cc} \mathbf{0} & \mathbf{I} \\ \frac{\partial \mathbf{f}_1(\mathbf{x},t)}{\partial \mathbf{q}} & \frac{\partial \mathbf{f}_1(\mathbf{x},t)}{\partial \dot{\mathbf{q}}} \end{array} \right]\Bigg|_{\mathbf{x}_e}. \tag{3.6}$$

$\mathbf{A}$ is a finite matrix and Eq. (3.6) is asymptotically stable if the real part of all the eigenvalues μ_i of matrix $\mathbf{A}$ are negative [59].

In case of the constrained system (1.5)-(1.3), the dimension of $\mathbf{x}$ is $2\,n$ and because of the m number of constraints the system has only $n - m$ degrees of freedom. Hence, only $g = n - m$ pairs of eigenvalues characterize the dynamics of the system. Eq. (3.4) contains m constraint relations at the acceleration level. In order to see the additional effect of acceleration level constraints 1.9 let us write Eq. (1.9) in first order form as:

$$\begin{bmatrix} \dot{\boldsymbol{\varphi}} \\ \ddot{\boldsymbol{\varphi}} \end{bmatrix} = \begin{bmatrix} 0 & \mathbf{I} \\ 0 & 0 \end{bmatrix} \begin{bmatrix} \boldsymbol{\varphi} \\ \dot{\boldsymbol{\varphi}} \end{bmatrix}. \tag{3.7}$$

The leading matrix of (3.7) have $2\,m$ zero eigenvalues. These eigenvalues also appear in the direct investigation and these have to be isolated from the eigenvalues of matrix $\mathbf{A}$ in Eq. (3.6). It seems straightforward to collect $2\,m$ zero eigenvalues from the eigenvalue vector $\boldsymbol{\mu} = [\mu_1 \cdots \mu_{2\,n}]^\mathrm{T}$. But in such systems, when there are eigenvalues close to zero, the numerical selection of the non-physical eigenvalues has limitations.

I propose that in order to detect physically meaningless eigenvalues a detection function is introduced as:

$$\ddot{\boldsymbol{\varphi}} + \mathbf{f}_s = \mathbf{0}, \text{ where } \quad \mathbf{f}_s = a_1\,\dot{\boldsymbol{\varphi}} + a_2\,\boldsymbol{\varphi} = \mathbf{0}. \tag{3.8}$$

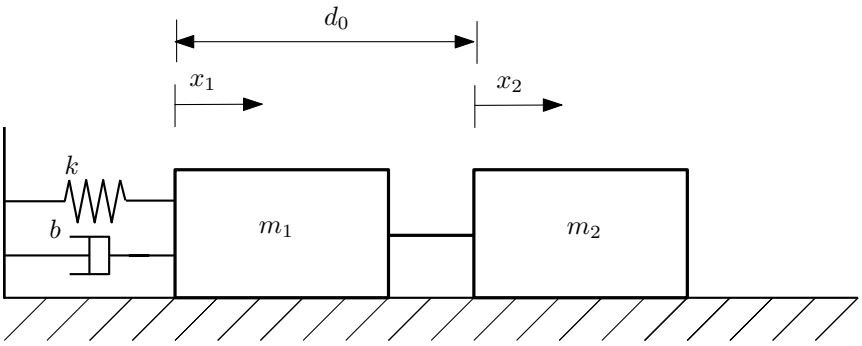

FIGURE 3.2. Constrained system example

This function introduces a fictitious dynamic behaviour associated with the constraints. With the introduced dynamical behaviour the physically meaningless eigenvalues can be detected using sensitivity analysis [58] with respect to parameters a_1 and a_2. The form of the expression (3.8) has similiar structure as the Baumgarte stabilization technique, but here the introduced terms are used only for detecting of the spurious eigenvalues and not for the stabilization of the constraints. In the proposed method, the constraints in the form of (3.8) are used in (3.4) instead of (1.9). For the local sensitivity analysis the partial derivatives of the eigenvalues $\boldsymbol{\mu}$ respect to a_1 and a_2 are calculated. These partial derivatives are given with the following Jacobian

$$\mathbf{T} = \begin{bmatrix} \frac{\partial \mu_1}{\partial a_1} & \dots & \frac{\partial \mu_{2\,n}}{\partial a_1} \\ \frac{\partial \mu_1}{\partial a_2} & \dots & \frac{\partial \mu_{2\,n}}{\partial a_2} \end{bmatrix}. \tag{3.9}$$

In practice this matrix can be constructed with numerical differentiation. The $2\,m$ number of largest elements in the first row of Jacobian $\mathbf{T}$ are associated with the spurious eigenvalues. This is also true for the second row, which provides redundant information regarding the eigenvalues. The related $2\,m$ number of eigenvalues have to be discarded from $\boldsymbol{\mu}$.

The above explained method is possible because of the Rouche's theorem [64], which states that the eigenvalues μ_i change continuously, if the system parameters are also varied continuously.

3.1.1 Example for a continuous time system

In order to demonstrate the proposed technique, the simplest system with continuous time-behaviour, which can be described with differential algebraic equations, is analyzed. The benchmark example (see Fig. 3.2) is built up by two blocks. The blocks are connected with a rigid rod, the system has one DoF. This system is described by dependent coordinates $\mathbf{q} = [x_1, x_2]^{\mathrm{T}}$. The only constraint is that the distance between the blocks is constant $\varphi = x_1 - x_2 - d_0 = 0$. Then Eq. (1.5) reads

$$\begin{bmatrix} m_1 & 0 \\ 0 & m_2 \end{bmatrix} \begin{bmatrix} \ddot{x}_1 \\ \ddot{x}_2 \end{bmatrix} + \begin{bmatrix} 1 \\ -1 \end{bmatrix} \lambda = \begin{bmatrix} -k\,x_1 - b\,\dot{x}_1 \\ 0 \end{bmatrix}. \tag{3.10}$$

Using the dependent coordinates based description, the eigenvalues can be calculated as it is proposed in (Sec. 3.1). For the numerical study the physical parameters were the following $m_1 = m_2 = 1\,\mathrm{kg}$, $b = 1\,\mathrm{N/m}$ $k = 1\,\mathrm{Ns/m}$. In the detecting function $\mathbf{f}_s$ the parameters are simply chosen as $a_1 = 1$ and $a_2 = 1$. Fig. 3.3 shows the elements of Jacobian $\mathbf{T}$. Both first and second rows show that the 3rd and 4th eigenvalues have to be discarded. In order to show that the introduced detecting

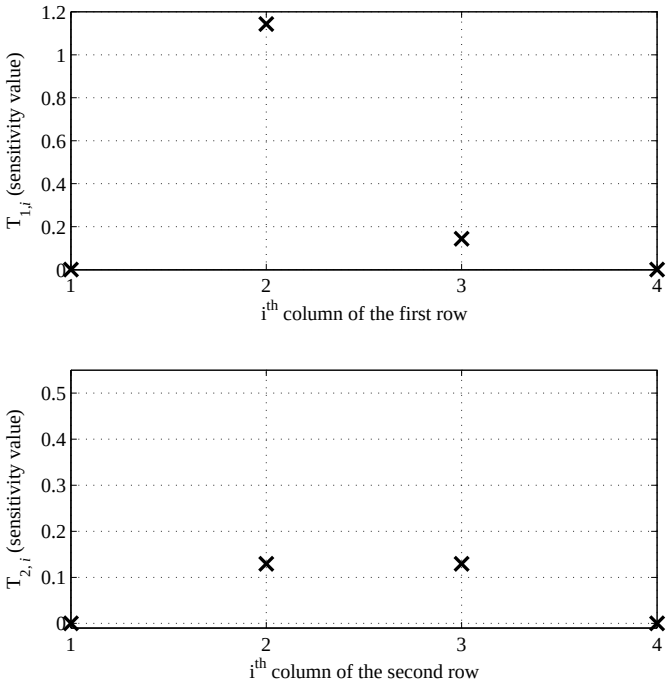

FIGURE 3.3. Jacobian $\mathbf{T}$ of the sensitivity function in case of the two-mass example

TABLE 3.1. Calculated eigenvalues of the two-mass example in continuous case

	DAE based solution	Exact solution
eigenvalue of the physical system	$-0.2500 + 0.6614i$	$-0.2500 + 0.6614i$
eigenvalue of the physical system	$-0.2500 - 0.6614i$	$-0.2500 - 0.6614i$
eigenvalues due to constrained dynamics	-8.8730	-
eigenvalues due to constrained dynamics	-1.1270	-

function $\mathbf{f}_s$ does not change the values of the real eigenvalues, the eigenvalues are calculated with different a_1 parameters. Fig. 3.4 shows that only the non-physical eigenvalues change.

To verify the result let us calculate the eigenvalues using independent coordinates based description. In this case position of the first block x_1 is chosen as the generalized coordinate. The equation of motion reads

$$(m_1 + m_2)\ddot{x}_1 + k\dot{x}_1 + bx_1 = 0, \tag{3.11}$$

where m_1 and m_2 are the masses of the blocks respectively, b is the damping coefficient and k is the stiffness coefficients. In this case the eigenvalues can be expressed in analytical form

$$\lambda_{1,2} = \frac{-b \pm \sqrt{b^2 - 4k(m_1 + m_2)}}{2(m_1 + m_2)}. \tag{3.12}$$

The results of the proposed method and analytical calculations are summarized in Table 3.1. The results show that using the dependent coordinates based description the real eigenvalues of the system could be calculated, the results are the same as with analytical calculations (3.12) and the error is within the limits of the round-off error.

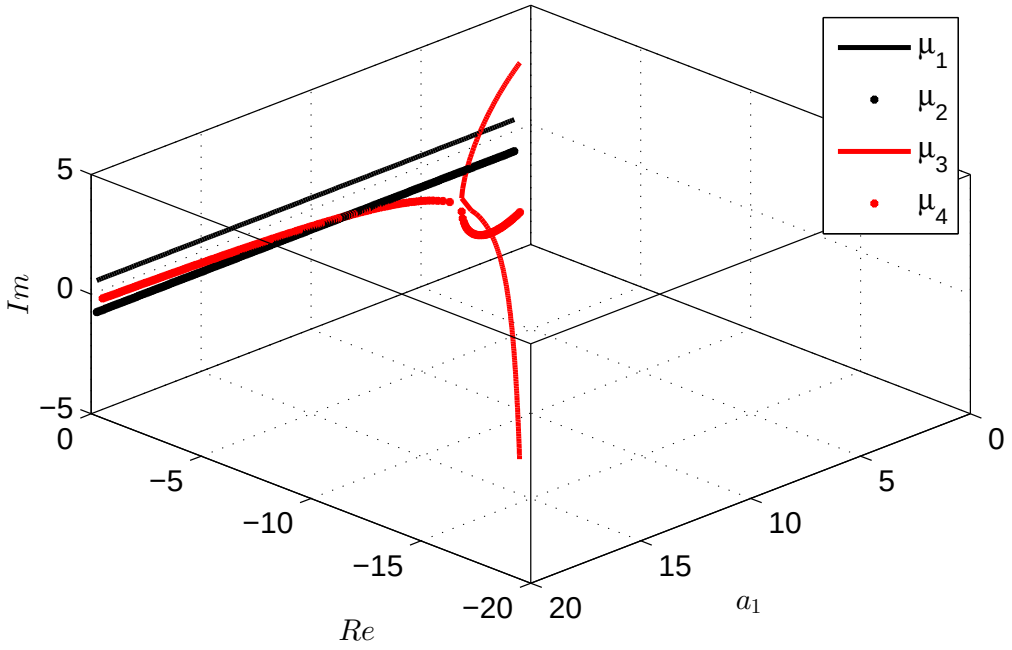

FIGURE 3.4. Changing of the non-physical eigenvalues in case of the two-mass example

3.2 Eigenvalue separation for sampled systems

The stability investigation technique introduced in Sec. 3.1 can be extended to sampled systems. Considering the discrete behavior of the digitally controlled system, a piecewise solution of the linearized equation of motion have to be constructed for eigenvalue analysis.

It is assumed that during the operation of a robotic system, the $(i-1)^{\text{th}}$ measured values of $\mathbf{q}$ and $\dot{\mathbf{q}}$ are used in the control law. Then the calculated control forces $\mathbf{u}$ are available at the i^{th} time instant and they are held by a zero-order-hold (ZOH) until the end of the $(i+1)^{\text{th}}$ sampling instant. Thus a ZOH plus a unit delay is supposed. In case of a real device, this control input $\mathbf{u}$ is commanded to the physical system. In the case of stability investigation or numerical simulation, $\mathbf{u}$ is substituted into Eq. (2.13). As a result, we obtain the dynamic model of the closed-loop system.

The linearized equation of motion (3.5) can be extended to the above explained closed-loop, sampled system as

$$\dot{\boldsymbol{\xi}}(t) = \mathbf{A}_{|\mathbf{x}_e}\boldsymbol{\xi}(t) + \mathbf{B}_{|\mathbf{x}_e}\boldsymbol{\xi}(t_{i-1}), \quad t \in [t_i, t_{i+1}]. \tag{3.13}$$

Again the state vector is $\mathbf{x} = [\mathbf{q},\, \dot{\mathbf{q}}]^{\mathrm{T}}$ and $\boldsymbol{\xi} = \mathbf{x} - \mathbf{x}_e$. The solution of Eq. (3.13) for the state variables at the end of the i^{th} sampling interval is calculated as

$$\mathbf{x}(t_{i+1}) = \mathbf{A}_{\mathrm{d}}\mathbf{x}(t_i) + \mathbf{B}_{\mathrm{d}}\mathbf{x}(t_{i-1}), \tag{3.14}$$

where $\mathbf{A}_{\mathrm{d}}$ and $\mathbf{B}_{\mathrm{d}}$ can be calculated utilizing the following property [59]

$$e^{\mathbf{W}T_s} = \begin{bmatrix} \mathbf{A}_{\mathrm{d}} & \mathbf{B}_{\mathrm{d}} \\ \mathbf{0} & \mathbf{I} \end{bmatrix}, \tag{3.15}$$

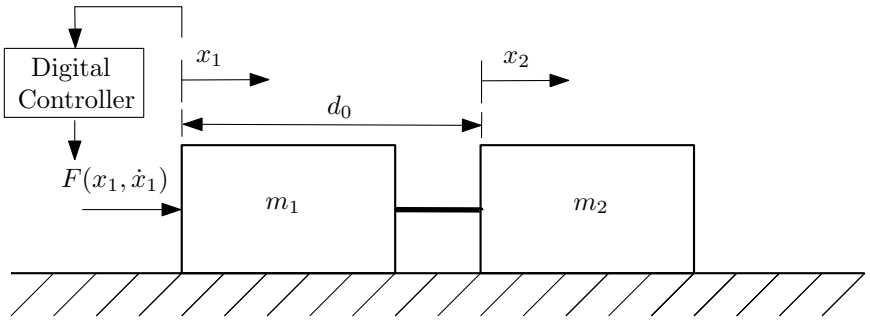

FIGURE 3.5. Constrained system example

where T_s is the sampling time of the digital controller, and matrix $\mathbf{W}$ is

$$\mathbf{W} = \begin{bmatrix} \mathbf{A} & \mathbf{B} \\ \mathbf{0} & \mathbf{0} \end{bmatrix}. \tag{3.16}$$

Then by introducing the new discrete state variable $\mathbf{z}_j = [\mathbf{x}_j,\ \mathbf{x}_{j-1}]^{\mathrm{T}} \in \mathbb{R}^{4n}$, the stability of the digitally controlled system can be investigated by calculating the eigenvalues of the discrete mapping constructed from the piecewise solution of the equation of motion [59]

$$\mathbf{z}_{j+1} = \mathbf{C}\,\mathbf{z}_j \ \text{ with } \mathbf{C} = \begin{bmatrix} \mathbf{A}_d & \mathbf{B}_d \\ \mathbf{I} & \mathbf{0} \end{bmatrix}. \tag{3.17}$$

The convergence of the multi-dimensional geometric series described in Eq. (3.17) is equivalent to the asymptotic stability of the desired motion of the controlled system [65]. Thus, to ensure stability, the eigenvalues of $\mathbf{C}$ have to be located within a unit circle of the complex plane [59].

When the system is modelled with non-minimum set of descriptor coordinates, as in Eq. (1.10), the mathematical description results in non-physical eigenvalues, similarly to the continuous case. Here, again, m number of constraints are present. Since the mapping matrix have $4\,n$ number of eigenvalues, in this case $4\,m$ eigenvalues have to be separated.

If we apply stability analysis technique to the first order form of the constraint equations (3.7), $2\,m$ number of zeros and $2\,m$ number of ones are obtained. These $2\,m$ number of zero eigenvalues are not separated, because they are necessarily in a unit circle and hence do not influence the stability.

Using the sensitivity function (3.8) $2\,m$ number of eigenvalues -the ones- of the mapping matrix $\mathbf{C}$ depends on the value of a_1 and a_2. The procedure of their elimination is the same as in case of continuous case. The only difference is that the size of Jacobian $\mathbf{T} \in \mathbb{R}^{2\times 4n}$ in Eq. (3.9) is the double.

3.2.1 Example for sampled systems

Similarly to the continuous case, a demonstrative example will be used to introduce the proposed method. The benchmark problem shown in 3.2 is modified for the demonstration. Hence the spring and the damper is replaced with a simple digital Proportional Derivative (PD) controller as it is shown in Fig. 3.5. Governing equation of motion using the dependent coordinates is modified as

$$\begin{bmatrix} m_1 & 0 \\ 0 & m_2 \end{bmatrix} \begin{bmatrix} \ddot{x}_1 \\ \ddot{x}_2 \end{bmatrix} + \begin{bmatrix} 1 \\ -1 \end{bmatrix} \lambda = \begin{bmatrix} f_c \\ 0 \end{bmatrix}. \tag{3.18}$$

In the benchmark example it is assumed that the control force f_c is calculated using a zero order holder as

$$f_c = -P\, x_1(t_{i-1}) - D\, \dot{x}_1(t_{i-1}), \quad t \in [t_i, t_{i+1}). \tag{3.19}$$

The masses are $m_1 = m_2 = 1\,[\mathrm{kg}]$, while the control parameters for the test calculation were selected as: $P = 1\mathrm{N/m}, \mathrm{D}{=}1\mathrm{Ns/m}$. Using the dependent coordinates based description, the eigenvalues can be calculated as it is proposed above. Fig. 3.6 shows the elements of Jacobian $\mathbf{T}$. The first and second rows also show that here the 5rd and 6th eigenvalues have to be eliminated. The absolute value of the complex eigenvalues are presented in Table 3.2. In order to show that the proposed method does not change the real eigenvalues of the system the eigenvalues are calculated with different a_1 parameters. The Fig. 3.7 shows that only the two non-physical eigenvalues are changed. These eigenvalues are shown in red colour.

As a comparison, let us formulate the ODE equation of the controlled system using the minimum set of descriptor coordinates (x_1) as

$$(m_1 + m_2)\, \ddot{x}_1(t) = -P\, x_1(t_{i-1}) - D\, \dot{x}_1(t_{i-1}), \quad t \in [t_i, t_{i+1}). \tag{3.20}$$

The eigenvalues of this ODE based discrete-time system can be computed as it is described by Eqs. (3.13)-(3.16). These eigenvalues are summarized in the right column of Table 3.2. With proposed method using the dependent coordinates based (DAE) description the same results could be obtained as with independent coordinates (ODE) based description.

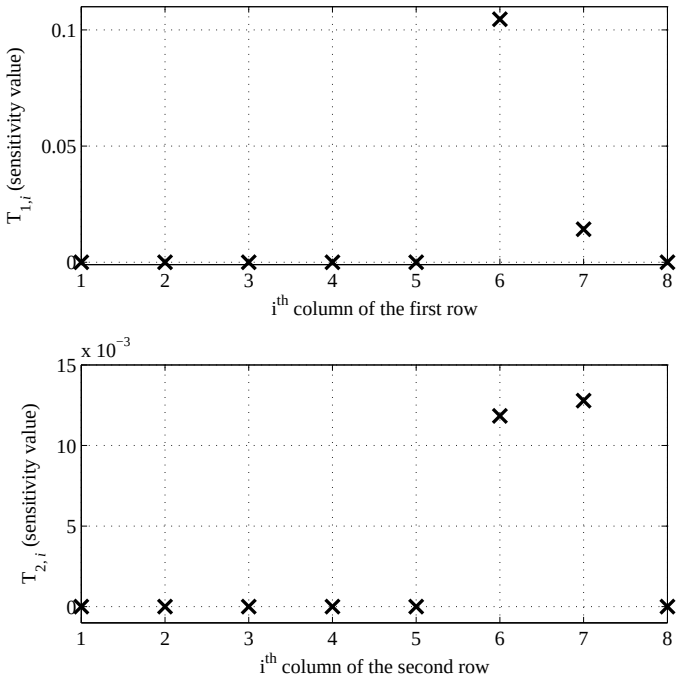

FIGURE 3.6. Jacobian $\mathbf{T}$ of the sensitivity function in case of the two-mass example in discrete case

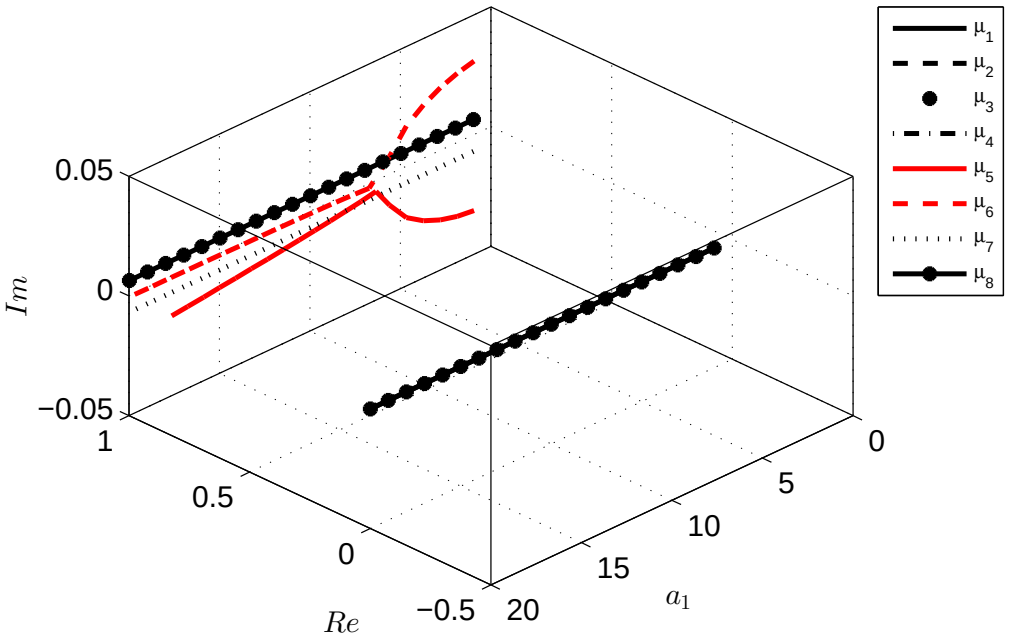

FIGURE 3.7. Changing of the calculated eigenvalues in discrete case

TABLE 3.2. Calculated eigenvalues of the two-mass example in sampled case

	DAE based solution	ODE based solution
eigenvalue of the physical system	0.9975	0.9975
eigenvalue of the physical system	0.9975	0.9975
eigenvalue of the physical system	0.0050	0.0050
eigenvalue of the physical system	0	0
eigenvalue due to the constrained dynamics	−8.8730	-
eigenvalue due to the constrained dynamics	−1.1270	-
eigenvalue due to the constrained dynamics	0	-
eigenvalue due to the constrained dynamics	0	-

3.3 New results

When holonomic multibody systems are modeled with dependent coordinates their dynamics is described by a system of index-3 differential algebraic equations (DAE). The direct eigenvalue analysis of these systems results in spurious, non-physical eigenvalues due to the applied geometric constraints. Therefore, for the stability analysis the modeled system is often re-parametrized in terms of minimum set of generalized coordinates. This requires an additional step and the non-unique selection of the new generalized coordinates.

Thesis 1.

The method proposed in this thesis makes the eigenvalue analysis possible without the re-parametrization of the dynamic equations as follows:

- **Index reduction is carried out to obtain an index-1 DAE.**
- **The acceleration level constraint equations are modified by a sensitivity function.**
- **The first order form system is linearized around the investigated equilibrium.**
- **The eigenvalues are calculated.**
- **Applying a sensitivity analysis as a final step the non-physical eigenvalues are discarded.**

In case of a sampled data system prior to the eigenvalue investigation, the solution for one sampling period is generated and the discrete state transition mapping is constructed. Then the spurious eigenvalues can be discarded with the sensitivity analysis. It is a practical, convenient selection, if the sensitivity parameters are equal to or smaller than the Baumgarte-parameters which fit to the investigated system.

Related journal publication:

L. Bencsik, L.L. Kovács, and A. Zelei, "Stabilization of internal dynamics of underactuated systems by periodic servo-constraints," *International Journal of Structural Stability and Dynamics*, 2017, 14 pages, paper id: 1740004.

Other related publication:

[67]

Chapter 4

Application of the method of blended servo-constraints

The generalization of the computed torque controller for underactuated systems (2.21) has a general form, however the direct application of the introduced techniques has difficulties. In case of an underactuated system, the problem is caused by the unstable internal dynamics [1]. The definition of the internal dynamics is given in Sec. 2.1.3. In a given system the internal dynamics depends on the chosen output only. Accordingly, in case of unstable internal dynamics, stable operation requires the modification of the original output (servo-constraint). In the related literature [1], [21], [68], [69] this intuitive modification is formulated for robots with open kinematic chain only. There the linear combination of the active and passive joints are considered as an output which have to be controlled.

Instead, here I propose a more general formalism along the lines of Alpha-blending method [70], which is used in computer graphics. In the followings, this method is mentioned as *method of blended servo-constraints* . The new servo-constraint is the combination of the original servo-constraint $\widehat{\boldsymbol{\gamma}}$ and the newly introduced stabilizing term $\boldsymbol{\gamma}_s$. The reformulated servo-constraint vector is written as

$$\boldsymbol{\gamma} = \kappa\,\widehat{\boldsymbol{\gamma}} + (1-\kappa)\,\boldsymbol{\gamma}_s, \tag{4.1}$$

where κ is the blending factor. In order to choose a servo-constraint set, which makes the stable operation possible, first the stability analysis of the internal dynamics is discussed. Thereafter, a benchmark problem and a real robotic system are investigated in detail.

4.1 Analysis of the internal dynamics

The behaviour of the internal dynamics is a key question in underactuated systems. Below two methods will be presented for the characterization of the internal dynamics. The first method requires the introducing of a new parametrization. In contrast, the second newly proposed method is based on a DAE formalism which could be more beneficial in complex systems.

Intuitive separation of coordinates

The systematic separation of controlled (also referred as driven in [1]) and internal dynamics makes possible the prudent analysis of the internal dynamics as it is also published in [68]. A new set of coordinates has to be introduced for this separation. Outputs $\boldsymbol{\gamma} \in \mathbb{R}^l$ (servo-constraints) and the

intuitively chosen internal states $\boldsymbol{\eta} \in \mathbb{R}^{n-l}$ are the new set of coordinates $\widetilde{\mathbf{q}} = [\boldsymbol{\gamma}, \boldsymbol{\eta}]^{\mathrm{T}} \in \mathbb{R}^n$. From the servo-constraint at the acceleration level Eq. (2.17) and from the equation of motion (2.13) the controlled dynamics can be expressed as

$$\ddot{\boldsymbol{\gamma}} = \boldsymbol{\Gamma}(\mathbf{M}^{-1}(\mathbf{c} - \mathbf{Q} + \mathbf{H}\mathbf{u})) + \dot{\boldsymbol{\Gamma}}\dot{\mathbf{q}} - \dot{\mathbf{g}} \,. \tag{4.2}$$

From Eq. (4.2) the nominal control, which theoretically produce the required input, can be calculated

$$\bar{\mathbf{u}} = (\boldsymbol{\Gamma}(\mathbf{M}^{-1}\mathbf{H}))^{-1}(\boldsymbol{\Gamma}(\mathbf{M}^{-1}(\mathbf{Q} - \mathbf{c}) - \ddot{\boldsymbol{\gamma}} - \dot{\boldsymbol{\Gamma}}\dot{\mathbf{q}} + \dot{\mathbf{g}} \,) \,. \tag{4.3}$$

From the original coordinates the descriptor coordinates of the internal dynamics can be selected as $\boldsymbol{\eta} = \mathbf{S_u q}$, where $\mathbf{S_u}$ is a selector matrix. Using the original equation of motion (2.13), and the nominal control torque Eq. (4.3) the internal dynamics can be expressed as

$$\ddot{\boldsymbol{\eta}} = \mathbf{S}_u(\mathbf{M}^{-1}(\mathbf{c} - \mathbf{Q} + \mathbf{H}\bar{\mathbf{u}}) = \boldsymbol{\alpha}(\boldsymbol{\eta}, \dot{\boldsymbol{\eta}}, \boldsymbol{\gamma}, \dot{\boldsymbol{\gamma}}, \ddot{\boldsymbol{\gamma}}). \tag{4.4}$$

This equation shows that the internal dynamics is nonlinear and it depends on the desired output $\mathbf{h}(t)$ (see Eq. 2.16) , which explicitly depends on time. Then for the analysis of the internal dynamics the concept of zero dynamics [47] [71] is used. For this, a constant system output $\dot{\mathbf{h}}(t) \equiv \mathbf{0}$ is considered which reduces the original problem to the investigation of a time-invariant nonlinear system. The local stability of the zero dynamics can be analyzed by considering the corresponding linearized system.

In case of a complex system, it is hard to intuitively select the coordinates $\boldsymbol{\eta}$, which represent the internal dynamics. This selection is not unique similarly to the selection of minimum set of descriptor coordinates in the dynamical modelling. In the related literature, there is no advice for the selection of the coordinates of the internal dynamics.

Proposed analysis of the internal dynamics

In the followings, a new concept is proposed for the analysis of the stability properties of the internal dynamics. The proposed method eliminates the need of the a priori selection of the different coordinates for the parametrization of the controlled and uncontrolled/internal dynamics.

It was shown in Sec. 3 that the stability investigation of a system can be carried out by using the original non-minimum set of descriptor coordinates. In that case, the equation of motion is subjected to geometric constraints and the motion is possible in the admissible directions only and the resulted eigenvalues are related with this admissible motion.

Here, the end-effector of the robot has to follow a desired trajectory. This trajectory is described by the servo-constraints. The motion, which is not restricted by the servo-constraints, belongs to the internal dynamics. We assume that the servo-constraints are perfectly satisfied and it can be substituted with geometric-constraints as Fig. 4.1 shows. With this assumption, the internal dynamics with identical to the admissible motion. Therefore the DAE based eigenvalue analysis can be used (see Sec. 3). Here the admissible dynamics is identical with the zero dynamics when the desired position is constant $\dot{\mathbf{h}}(t) \equiv \mathbf{0}$. In this case, the problem can be defined with the combination of the equation of the controlled motion (2.20) and the sensitivity function (3.8) as

$$\begin{bmatrix} \mathbf{M} & -\mathbf{H} \\ \boldsymbol{\Gamma} & \mathbf{0} \end{bmatrix} \begin{bmatrix} \ddot{\mathbf{q}} \\ \mathbf{u} \end{bmatrix} = \begin{bmatrix} -\mathbf{c} + \mathbf{Q} \\ -\dot{\boldsymbol{\Gamma}}\dot{\mathbf{q}} + \dot{\mathbf{g}} - a_2\dot{\boldsymbol{\gamma}} - a_1\boldsymbol{\gamma} \end{bmatrix}. \tag{4.5}$$

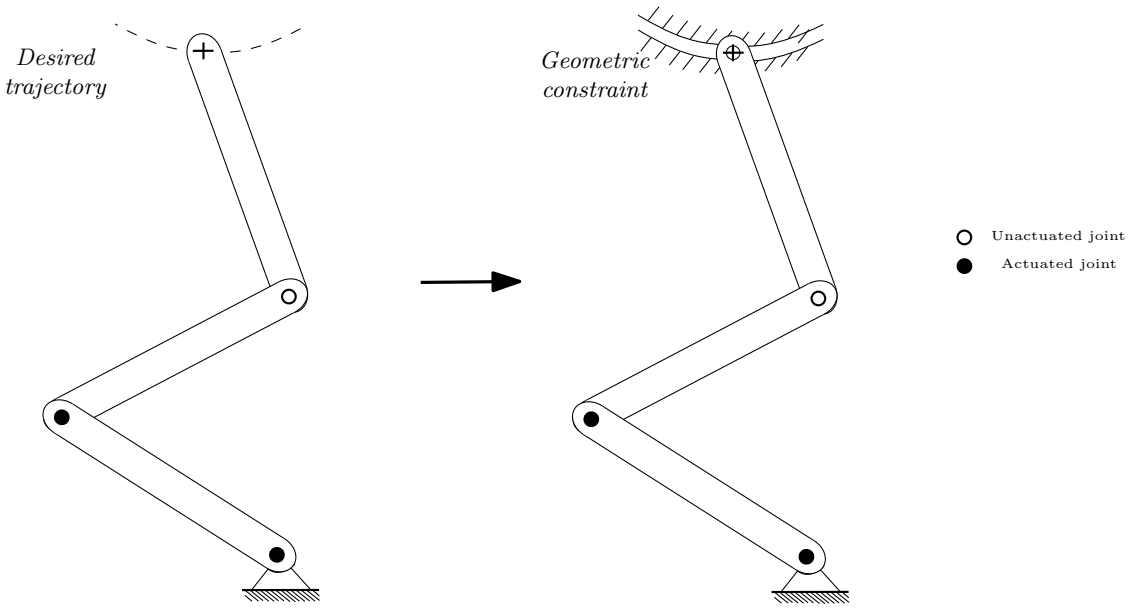

FIGURE 4.1. Underactuated system with different constraints

Here, a_1 and a_2 are the parameters of the sensitivity function which makes possible the elimination of the constrained eigenvalues as it is introduced in Sec. 3. From Eq. (4.5) the admissible accelerations can be expressed. Similarly to Eq. (3.5), it can be linearized around the investigated configuration $\mathbf{x}_0 = [\mathbf{q}_0, \dot{\mathbf{q}}_0]^{\mathrm{T}}$ with the constant desired output $\mathbf{h}$. Then the eigenvalues of the linearized system are computed as it is detailed in Sec. 3.1. Here the DoF is g and the dimension of the output is l and because of the first order form, $2\,l$ eigenvalues have to be discarded and the remaining $2(g-l)$ eigenvalues characterize the internal dynamics.

4.2 Representative benchmark and real world problems

In the following studies this technique will be applied in case of a sliding pendulum system and in order to show the general applicability of the method it will be also applied in case of a more complex robotic device.

4.2.1 Sliding pendulum

In the followings, a planar sliding pendulum (see Fig. 4.2) is analyzed. This benchmark problem can be used as a model of an open chain manipulator with passive last joint [21], [49]. This sliding pendulum could be a model of an overhead crane also.

The system is built up by a slider (linear drive) with mass m_1 and the carried object is symbolized with a homogeneous rod with mass m_2 and length l. The distance between the centre of mass CM and the joint A is r_{CM}. The frictions in the joint of the rod are modelled by a viscous damper b. The horizontal position of the slider and the inclination of the rod are the generalized coordinates $\mathbf{q} = [x_1, \vartheta]^{\mathrm{T}}$ respectively. The equation of motion can be obtained as

$$\begin{bmatrix} m_1 + m_2 & r_{\mathrm{CM}}\, m_2\, \cos\vartheta \\ r_{\mathrm{CM}}\, m_2\, \cos\vartheta & J_{\mathrm{CM}} + 0.25\, m_2\, l^2 \end{bmatrix} \begin{bmatrix} \ddot{x}_1 \\ \ddot{\vartheta} \end{bmatrix} + \begin{bmatrix} -m_l\, \sin\vartheta \dot{\vartheta}^2 \\ r_{\mathrm{CM}}\, g m_l \sin\vartheta + b\,\dot{\vartheta} \end{bmatrix} = \begin{bmatrix} 1 \\ 0 \end{bmatrix} F. \tag{4.6}$$

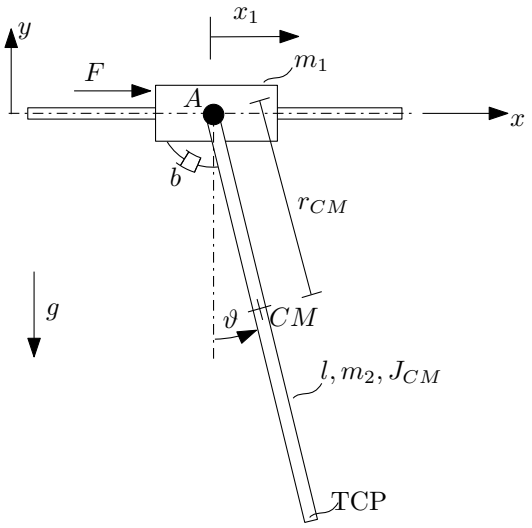

FIGURE 4.2. Sliding pendulum system

The control task is the horizontal positioning of the tip (point TCP). It can be formalised using the servo-constraints as

$$\gamma = x_{\mathrm{TCP}}(\mathbf{q}) - x^d_{\mathrm{TCP}} = x_1 + l\sin\vartheta - x^d_{\mathrm{TCP}}. \tag{4.7}$$

Using Eqs. (4.6), (4.7), the control force can be calculated by means of Eq. (2.20). In this control problem the sum of the elements of the relative degree vector is $\widetilde{r} = 2$. Thus internal dynamics remains in the case of this 2 DoF example. If we apply the control technique given by Eq. (2.20), the system will lose its stability regardless of the applied control gains. This is similar to the instability of the motion of the passive link in references [1] [72] [73] [49], and it is due to the unstable internal dynamics. It can be proven in several ways. The simplest way is if we express the angular acceleration from Eq. (4.6), which does not depend on the input force

$$\ddot{\vartheta} = \frac{r_{\mathrm{CM}}\, m_2\, \cos\vartheta\, \ddot{x}_1 + r_{\mathrm{CM}}\, g m_l \sin\vartheta + b\,\dot{\vartheta}}{J_{\mathrm{CM}} + 0.25\, m_2\, l^2}. \tag{4.8}$$

The horizontal acceleration of the controlled point can be obtained by time differentiating Eq. (4.7) as

$$\ddot{x}_{\mathrm{TCP}} = \ddot{x}_1 - l\cos\vartheta\ddot{\vartheta}. \tag{4.9}$$

The angular acceleration Eq. (4.8) can be substituted into Eq. (4.9). Since a homogeneous rod is considered, the inertia is $J_{\mathrm{CM}} = 1/12\, m\, l^2$ and the centre of gravity is placed at the geometrical centre ($r_{CM} = l/2$). This expression is linearized around the hanging down position. Omitting the gravity and damping, the horizontal acceleration can be expressed as

$$\ddot{x}_{\mathrm{TCP}} = \ddot{x}_1(1 - l\frac{3}{2\,l}) = -\frac{1}{2}\,\ddot{x}_1. \tag{4.10}$$

From Eq. (4.10) we can conclude that positive acceleration requires negative acceleration at the slider. It is easy to see that one can not achieve this for longer (finite) time. This contradictory condition indicates unstable internal dynamics.

Reference [21] and [73] propose to move the controlled point closer to the passive joint. Let the distance of the controlled point from the joint to be $\bar{r}$. In that case Eq. 4.10 modifies to

$$\ddot{x}_{\mathrm{TCP}} = \ddot{x}_1(1 - \bar{r}\frac{3}{2\,l}). \tag{4.11}$$

In this case, the controller will be stable if $\bar{r} < 2/3$. This point is the centre of percussion. With this modification the internal dynamics and therefore the applied computed torque controller will be stable. This modification can be formalized in more general form using the above introduced blended servo-constraint method. According to (4.1) let us choose the position of the slider as the stabilizing term $\gamma_s = x_1 - x^d_{\mathrm{TCP}}$.

Using the blended method, the reformulated servo-constraint can be written as the combination of the original servo-constraint and the stabilizing term

$$\gamma = \kappa\,(x_1 + l\sin\vartheta - x^d_{\mathrm{TCP}}) + (1-\kappa)\,(x_1 - x^d_{\mathrm{TCP}}), \quad \mathbf{\Gamma} = [1, \kappa\,l\cos\vartheta]^{\mathrm{T}}. \tag{4.12}$$

In case of this example, it can be proven that around the hanging down position κ have to be smaller than $2/3$ (similar to Eq. (4.11)) in order achieve that the controlled point is located below the centre of percussion.

In case of a simple example this modification can be made using simple physical intuitions. In case of a more complex system, a detailed study is required for the modification of the servo-constraints. The stability of the internal dynamics is analyzed in the subsequent section.

4.2.1.1 The stability of the internal dynamics

For the following numerical studies, the mechanical parameters of the sliding pendulum are originated from a mobile crane laboratory device which is shown in Fig. 4.3. The mechanical model of the mobile crane is the sliding pendulum system (Fig. 4.2).

That mobile crane is composed by a DC motor driven mobile cart and a passive (not directly driven) rod. The task of the robot is same as the task of the sliding pendulum. The position of the cart is measured via the encoder of the motor, and there is an encoder in the passive joint for measuring the nutation angle. The mechanical parameters used in Eq. 4.6 are summarized in Table 4.1. The task, which considers the original control objective and the original internal dynamics, is formalised in Eq. (4.1).

The eigenvalues of the linearized internal dynamics are investigated as the function of the coupling term κ. In order to formulate the controlled dynamics as it appears in Eq. (2.21), the equation of motion Eq. (4.6) and the servo-constraints Eq. 4.12 are used. The eigenvalues of the controlled (constrained) system can be calculated around the hanging down position $\mathbf{q}_e = [x_e, \vartheta_e]^{\mathrm{T}} = [0,\,0]^{\mathrm{T}}$ with $x^d_{\mathrm{TCP}} = 0$. Fig. 4.4a shows the eigenvalues λ_1, λ_2 of the internal dynamics and the zero eigenvalues $\lambda_{d1}, \lambda_{d2}$ of the driven dynamics. These zero eigenvalues can be discarded using the detailed sensitivity analysis. In Eq. (4.5) the sensitivity parameters were $a_1 = a_2 = 1$. Fig. 4.4b shows the eigenvalues of the internal dynamics after the separation. For the better visibility Fig. 4.4c shows eigenvalues under the stability border κ^*. It can be concluded that the eigenvalues of the real part are negative when $\kappa < 2/3$. Let $\kappa^* = 2/3$ denote the corresponding stability boundary. This boundary is obtained from the physical intuitions based calculations in Eqs. (4.8)-(4.11) also. This result is the same with the results of [68], but here the separation of the internal and controlled dynamics was not necessary.

FIGURE 4.3. Mobile crane experimental device

Above κ^* the internal dynamics is not stable and the computed torque control method given in Eq. (2.21) is not feasible.

TABLE 4.1. Mechanical parameters of the mobile crane experimental device

mass of the cart	(m_1)	6.35 kg
mass of the pole	(m_2)	0.1 kg
length of the pole	(l)	0.9 m
inertia of the pole	(J_{CM})	0.00675 kgm^2
viscous friction	(b)	0.002Ns/m

4.2.1.2 The stability behaviour of the discrete system

While the stability of the internal dynamics is not sufficient for the stability of the whole digitally controlled system, in the followings, the stability of the digitally sampled system will be investigated. The discrete mapping of the digitally controlled system can be constructed as it is detailed from Eq. (3.13) to Eq. (3.17). Similarly to the investigation of the internal dynamics, the linearization was carried out around the hanging down position. In case of the experiment, the sampling time was $T_s = 0.03\,\mathrm{s}$ because of the controller electronics.

The stability calculations were carried out in the space of the proportional and derivative control parameters (see Eq. (2.21)) and the coupling term κ. In order to keep the number of free control parameters low the control gain matrices are selected as $\mathbf{K}_{\mathrm{P}} = K_{\mathrm{P}}\,\mathbf{I}$ and $\mathbf{K}_{\mathrm{D}} = K_{\mathrm{D}}\,\mathbf{I}$, and in the stability investigation carried out in the space of the scalar K_{P}, K_{D} values throughout the whole thesis.

The stability charts of Fig. 4.5 show the domain of stable parameters.

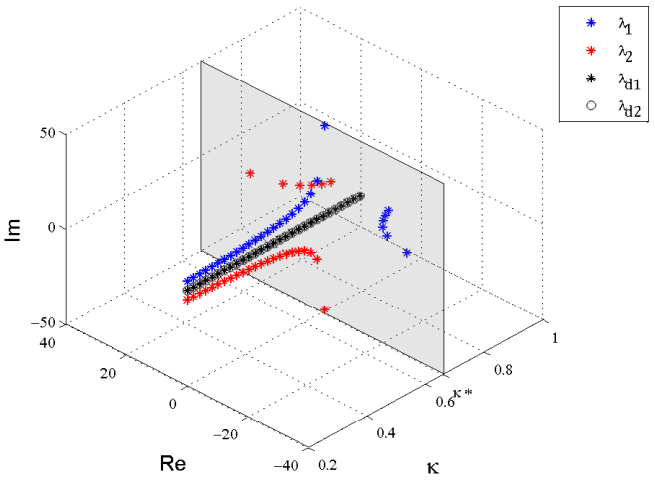

(A) Eigenvalues of the internal dynamics before the separation

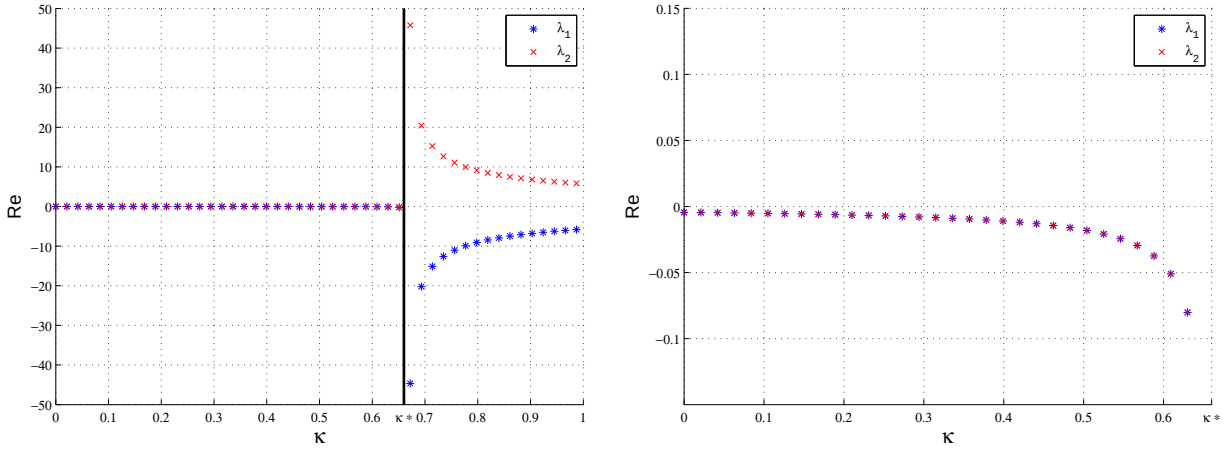

(B) Eigenvalues of the internal dynamics after the separation

(C) The stable eigenvalues of the internal dynamics after the separation

FIGURE 4.4. Eigenvalues of the internal dynamics

In Fig. 4.5a the change of the stability borders are depicted in case of different κ values. In Fig. 4.5b the stability charts are illustrated at characteristic κ values. In that figure, the same shades of gray belong to the same ranges of the spectral radii ρ [59]. Again, the system is stable when the spectral radii ρ of the discrete mapping is less than 1. Based on the stability charts it can be concluded that the fastest decay $\rho_{min} = 0.947$ can be achieved when the coupling term is $\kappa = 0.6$ and the control gains are $K_\mathrm{P} = 142.4[1/\mathrm{s}^2]$, $K_\mathrm{D} = 24.6[1/\mathrm{s}]$.

The area of the stable domains are the largest and therefore the control parameters could be selected from the widest range when $\kappa = 0.5$. The results show that the stability is not guaranteed at $\kappa < 2/3$. Considering the sampled data control, the blending parameter κ should be further reduced. The limit of stability is approximately at $\kappa^* \approx 0.62$.

4.2.1.3 Simulations and experiments

The proposed control algorithm has been tested with numerical simulations and it has been also applied on the introduced laboratory device. The lower end of the rod is commanded to follow a

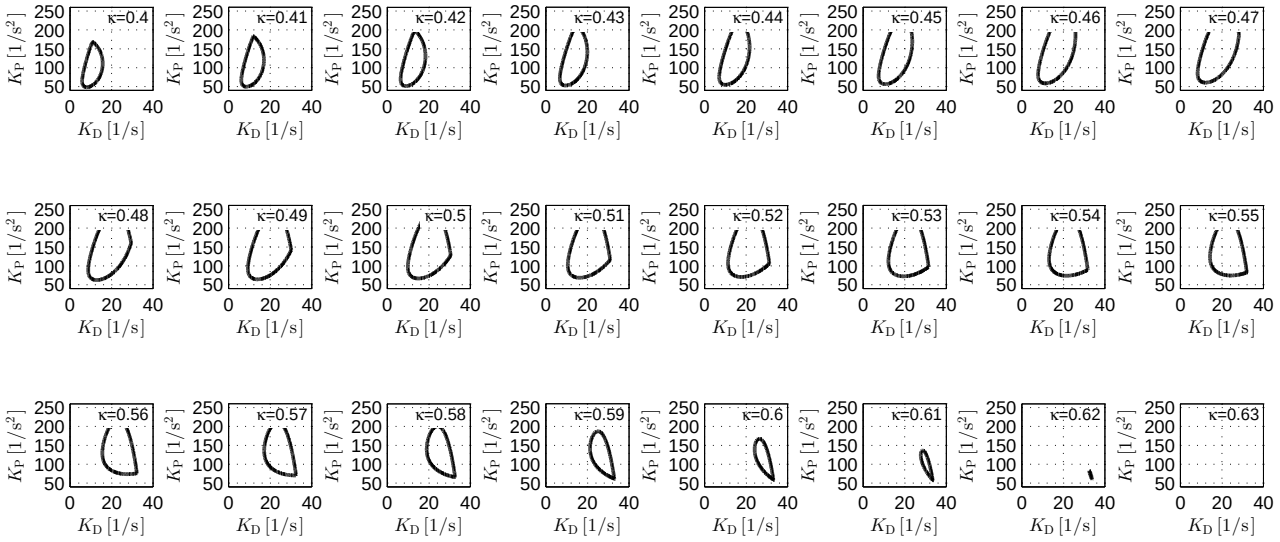

(A) The stable domains of the control parameters

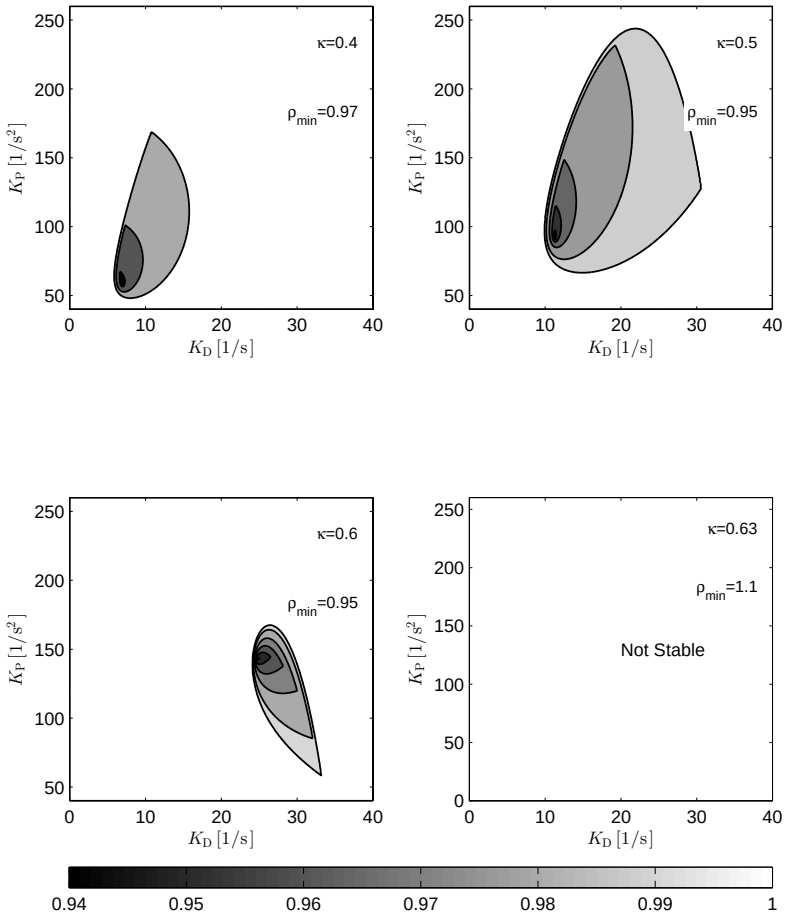

(B) Stability charts at characteristic κ values

FIGURE 4.5. Stability charts of the Sliding pendulum system

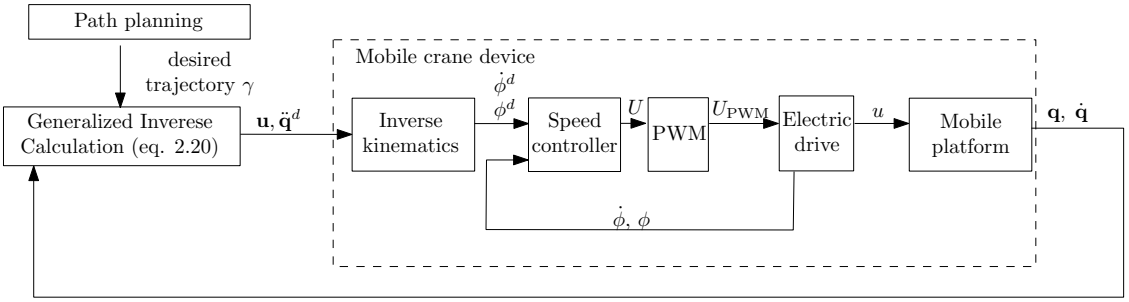

FIGURE 4.6. The scheme of the controller in case of the laboratory device

horizontal trajectory. This is defined by the C^8 continuous polynomial which is widely used in the benchmark problems of underactuated multibody systems [21], [74]

$$x^d_{\mathrm{TCP}}(t) = x_0 + \left(126\left(\frac{t}{\tau}\right)^5 - 420\left(\frac{t}{\tau}\right)^6 + 540\left(\frac{t}{\tau}\right)^7 - 315\left(\frac{t}{\tau}\right)^8 + 70\left(\frac{t}{\tau}\right)^9\right)(x_{\mathrm{END}} - x_0). \quad (4.13)$$

Parameter τ is the time duration of the desired motion between the horizontal position x_0 and x_{END}. In the following study these were set as $\tau = 10\,\mathrm{s}$, $x_0 = 0\,\mathrm{m}$ and $x_{\mathrm{END}} = 0.5\,\mathrm{m}$

The mobile crane experimental device was built for the verification of the simulations of the sliding pendulum model in the frame of a student research project [75]. The mobile platform is driven by a brushed DC gearheadmotor [76]. The gear ratio of the drive is $i_g = 63.3$. The motor drives the shaft of the drive wheel with a toothed belt without speed modification.

The equation of motion of the experimental device is given by Eq. (4.6) with the parameters of Table 4.1. Using Eq. (2.20), the required force and the desired accelerations ($\ddot{\mathbf{q}}^d$) can be calculated. In case of the laboratory device, the source voltage (U) of the motor is commanded. The voltage is adjusted with a PWM (Pulse-Width-Modulation)[77] controller. The PWM frequency was 18kHz, it is outside the audible frequency range and allows for quiet motor operation. The voltage is determined in a such way that the motor speed converges to a desired value. Thus at i^{th} sampling, the control voltage is calculated as

$$U_i = P\,(\dot{\phi}^d_i - \dot{\phi}_{i-1}) + I\,,(\phi^d_i - \phi_{i-1}), \quad (4.14)$$

where P and I are the proportional and integral gains respectively, and ϕ is the angular position of the motor. The control gains of the speed controller is tuned using the Ziegler-Nichols method [78] and these parameters are $P = 2.3[\mathrm{V/s}]$, $I = 4.2[\mathrm{V}]$. The angular velocity $\dot{\phi}$ is determined with numerical differentiation.

The desired angular velocity and position of the mobile platform can be determined from the desired acceleration ($\ddot{x}^d_1$) as

$$\dot{\phi}^d_i = \int \frac{\ddot{x}_1}{r_w}\, i_g \quad \phi^d_i = \int\int \frac{\ddot{x}_1}{r_w}\, i_g, \quad (4.15)$$

where $r_w = 0.03\mathrm{m}$ is the radius of the drive wheel. The integrations are carried out with numerical schemes using the rectangular rule. As a summary Fig. 4.6 shows the whole control loop. The outer loop is a computed torque controller as in Fig. 2.5. The inner loop is a speed controller which results the control voltage, which is tuned by a PWM controller.

The control gains of the compute torque controller are selected based on the stability investigations (see Fig. 4.5). Thus the selected proportional gain was $K_{\mathrm{P}} = 142\,[1/\mathrm{s}^2]$ the derivative gain was $K_{\mathrm{D}} = 24\,[1/\mathrm{s}]$ and the coupling term was $\kappa = 0.6$ providing the fastest decay at $\rho_{min} = 0.96$.

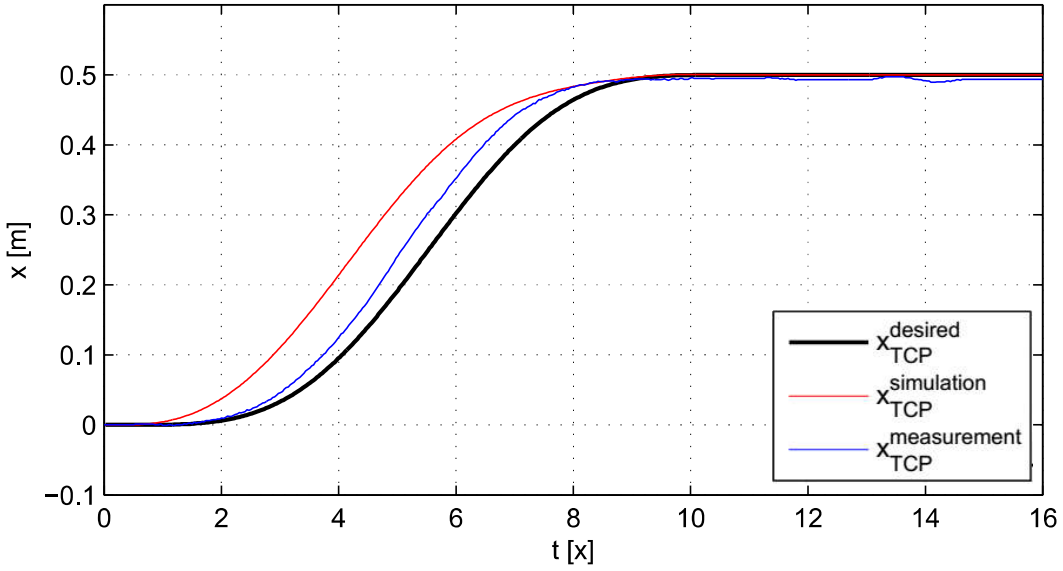

FIGURE 4.7. Simulation and measurement results in case of the sliding pendulum

Fig. 4.7 shows the simulation and experimental results compared to the desired output. The lower end of the rod follows the desired trajectory and it reaches the desired end position in a stable way in both cases. However, the applied blended servo-constraints cause an overshoot. In reference [68] a similiar phenomenon can be noticed in case of the control of a flexible arm.

To show the different mechanisms how the system can lose its stability two additional experiments were conducted. Beside the stable operation for the qualitative review of the stability investigations and to see the different stability losing mechanisms two unstable measurement scenario were analyzed. In the first experiment the control gains were selected from the unstable regions but providing that the internal dynamics is stable ($\kappa = 0.6, K_\mathrm{P} = 100\ [1/\mathrm{s}^2], K_\mathrm{D} = 10\ [1/\mathrm{s}]$). In the second experiment the coupling ratio was changed to $\kappa = 0.67$. In the first case (see Fig. 4.8a) the output oscillates around the desired value with a growing amplitude. This creates similar oscillations in the coordinate ϑ which represents the internal dynamics. In the experiments shown in Fig. 4.8b the system loses its stability in a catastrophic way. It is because the eigenvalues of the internal dynamics are real and have opposite signs (see Fig. 4.4) when $\kappa > 2/3$, which result in a saddle-node type bifurcation [57].

The measurement results are qualitatively the same as the numerical simulations. The results of the measurement and simulations show that the controlled system can be stable when the internal dynamics is stable. The stability of the internal dynamics can be achieved with the application of the blended constraints. The results also verify that if the control parameters are chosen from the stable regions the system works in stable way. The cost of the stability is that the applied blended method cause overshoot in the trajectory following which appears as positioning error. The maximum of the positioning error is 0.0351[m]. The positioning error is the highest when the highest acceleration is required and it tends to zero at the end of the motion. In the following chapter an other technique will be proposed which tries to minimize this positioning error.

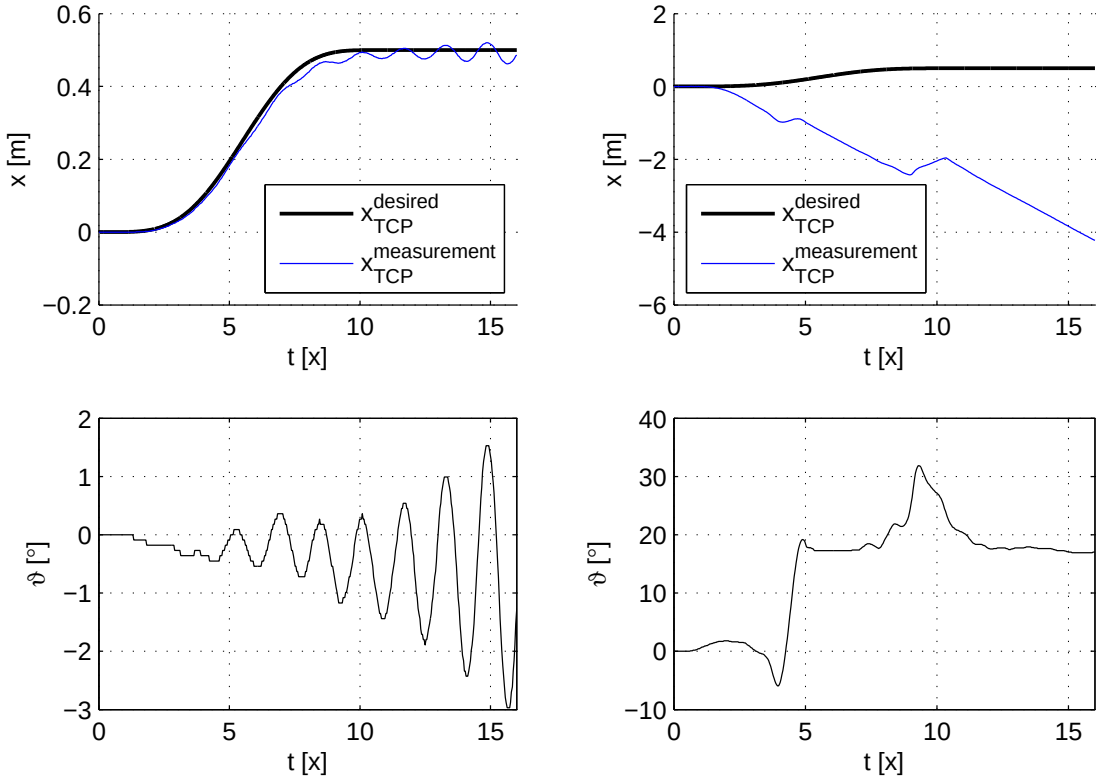

(A) Measurement results with unstable control parameters (B) Measurement results with unstable internal dynamics

FIGURE 4.8. Measurement results with unstable behaviour in case of the sliding pendulum

4.2.2 Planar model of the Acroboter service robot

This section provides a complex planar example for illustrating the application of the proposed stability analysis method. The planar model of the Acroboter service robot is considered [12] (see Fig. 4.9a). This robot is a suspended, pendulum-like underactuated manipulator. Its mechanical structure can be divided into two main units: the climber unit (CU) and the the swinging unit (SU). The CU moves along a suspended structure/ceiling and carries the SU which is supported and hoisted by the main cable and three secondary orienting cables. The main cable and secondary cables are connected via the cable connector (CC). The length of the cables are adjusted by servo motors, and the fine positioning of the SU is assisted by ducted fan actuators.

The analyzed planar model is shown in Fig. 4.9b. In this model the linear drive of the CU guarantees that P_1 follows the desired horizontal position x_{SU}^{d} of the SU. The position of point P_1 is described by an ideal constraint, the controlled dynamics of the CU is neglected. The forces exerted by the main cable, the two secondary cables and the ducted fan (located by $\boldsymbol{\rho}_T$) are the independent control inputs that drive the swinging unit. Since the planar model has five DoFs and the number of independent actuators is only four, the system is underactuated.

The kinematics of this model is parametrized by natural, i.e. fully Cartesian coordinates [14]. These are collected in the generalized coordinate array $\mathbf{q} = [x_2\ y_2\ x_3\ y_3\ x_4\ y_4]^T$, where the last four elements belong to the planar rigid body that represents the SU. With this, the equation of motion of the Acroboter system can be written in the basic DAE form of Eq. (1.10). According to [14] the mass matrix of the planar Acroboter model can be assembled as a constant block diagonal matrix

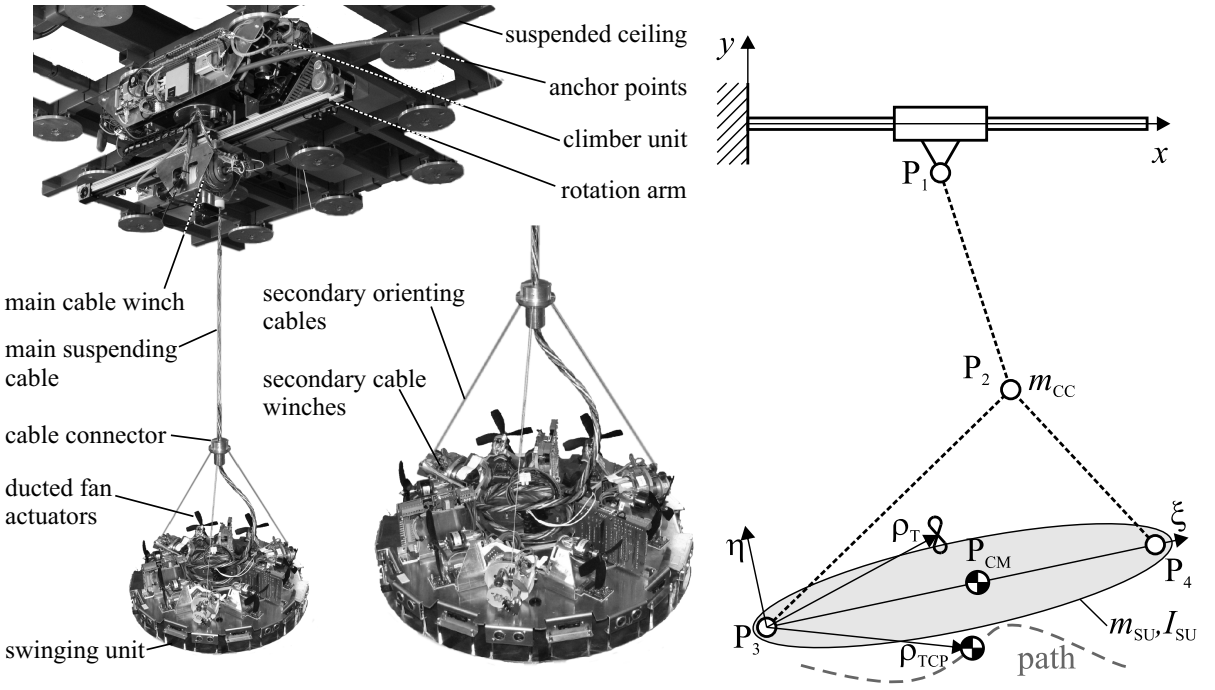

(A) The prototype of Acroboter platform (B) The planar model of Acroboter platform

FIGURE 4.9. The prototype of Acroboter platform

TABLE 4.2. Mechanical parameters of the planar Acroboter model

m_{CC}	0.1 kg
m_{SU}	4 kg
l_{SU}	0.5 m
$J_{\zeta\mathrm{SU}}$	0.8kgm^2
ξ_{CM}	0.25 m
η_{SU}	0 m
ξ_T	0.25 m
η_T	0.05 m

$\mathbf{M} = \mathrm{diag}(\mathbf{M}_{CC}\ \mathbf{M}_{SU})$ with the blocks $\mathbf{M}_{CC} = m_{CC}\,\mathbf{I}$, where $\mathbf{I}$ is the 2 by 2 identity matrix, and

$$\mathbf{M}_{SU} = \begin{bmatrix} \frac{m_{SU}(l_{SU}-2\xi_{CM})}{l_{SU}} + \frac{J_{\zeta\mathrm{SU}}}{l_{SU}^2} & 0 & \frac{m_{SU}\xi_{CM}}{l_{SU}} - \frac{J_{\zeta\mathrm{SU}}}{l_{SU}^2} & -\frac{m_{SU}\eta_{CM}}{l_{SU}} \\ 0 & \frac{m_{SU}(l_{SU}-2\xi_{CM})}{l_{SU}} + \frac{J_{\zeta\mathrm{SU}}}{l_{SU}^2} & \frac{m_{SU}\eta_{CM}}{l_{SU}} & \frac{m_{SU}\xi_{CM}}{l_{SU}} - \frac{J_{\zeta\mathrm{SU}}}{l_{SU}^2} \\ \frac{m_{SU}\xi_{CM}}{l_{SU}} - \frac{J_{\zeta\mathrm{SU}}}{l_{SU}^2} & \frac{m_{SU}\eta_{CM}}{l_{SU}} & \frac{J_{\zeta\mathrm{SU}}}{l_{SU}^2} & 0 \\ -\frac{m_{SU}\eta_{CM}}{l_{SU}} & \frac{m_{SU}\xi_{CM}}{l_{SU}} - \frac{J_{\zeta\mathrm{SU}}}{l_{SU}^2} & 0 & \frac{J_{\zeta\mathrm{SU}}}{l_{SU}^2} \end{bmatrix}, \tag{4.16}$$

where l_{SU} is the distance between the basic points P_3 and P_4, m_{CC} and m_{SU} are the masses of the CC and SU, respectively, and $J_{\zeta\mathrm{SU}}$ is the mass moment of inertia of the SU with respect to point P_3. In addition, ξ_{CM} and η_{CM} give the location of the center of mass of the SU in the body fixed frame $\{P_3; \xi, \eta, \zeta\}$. The corresponding physical parameters are summarized in Table. 4.2. The dependent coordinates are subjected to the kinematic constraint

$$\varphi = \frac{1}{2}\left((x_3 - x_4)^2 + (y_3 - y_4)^2 - l_{SU}^2\right)\ , \tag{4.17}$$

where the selection of the quadratic constraint expression leads to a constraint Jacobian which is linear in terms of the dependent coordinates

$$\mathbf{\Phi} = [0 \;\; 0 \;\; x_3 - x_4 \;\; y_3 - y_4 \;\; x_4 - x_3 \;\; y_4 - y_3] \,. \tag{4.18}$$

The system of applied forces consists of the non-inertial forces and the control forces. Here the only non-inertial force is the gravity force. Using the natural coordinate representation it has a simple constant form:

$$\mathbf{Q}_{ex} = \left[0 \quad -m_{\mathrm{CC}}\, g \quad \frac{m_{\mathrm{SU}} g \eta_{\mathrm{CM}}}{l_{\mathrm{SU}}} \quad \frac{m_{\mathrm{SU}} g (\xi_{\mathrm{CM}} - l_{\mathrm{SU}})}{l_{\mathrm{SU}}} \quad -\frac{m_{\mathrm{SU}} g \eta_{\mathrm{CM}}}{l_{SU}} \quad -\frac{m_{\mathrm{SU}} g \xi_{\mathrm{CM}}}{l_{\mathrm{SU}}}\right]^{\mathrm{T}} . \tag{4.19}$$

The control forces are collected in the vector $\mathbf{u} = [F_1 \;\; F_2 \;\; F_3 \;\; F_T]^{\mathrm{T}}$, where F_1 is the tension in the main cable, F_2 and F_3 are the cable forces applied through the orienting cables and F_T is the thrust force provided by the ducted fan actuator. The point of action of the thrust force is given by the parameters ξ_T and η_T in the body fixed frame. With this, the applied control forces can be expressed by the term $\mathbf{Hu}$, where the control input matrix $\mathbf{H}$ has the form

$$\mathbf{H} = \begin{bmatrix} -\frac{x_2}{l_1} & \frac{x_3-x_2}{l_2} & \frac{x_4-x_2}{l_3} & 0 \\ -\frac{y_2}{l_1} & \frac{y_3-y_2}{l_2} & \frac{y_4-y_2}{l_3} & 0 \\ 0 & \frac{x_2-x_3}{l_2} & 0 & \frac{(\xi_T - l_{SU})x_3 + (l_{SU} - \xi_T)x_4 + \eta_T(y_3-y_4)}{l_{\mathrm{SU}}^2} \\ 0 & \frac{y_2-y_3}{l_2} & 0 & \frac{\eta_T x_4 - \eta_T x_3 - (l_{SU} - \xi_T)(y_3-y_4)}{l_{\mathrm{SU}}^2} \\ 0 & 0 & \frac{x_2-x_4}{l_3} & \frac{\xi_T x_4 - \xi_T x_3 + \eta_T(y_4-y_3)}{l_{\mathrm{SU}}^2} \\ 0 & 0 & \frac{x_2-x_4}{l_3} & \frac{\eta_T x_3 - \eta_T x_4 - \xi_T y_3 + \xi_T y_4}{l_{\mathrm{SU}}^2} \end{bmatrix} \tag{4.20}$$

and l_i, $i = 1,2,3$ denote the varying lengths of the main and the orienting cables. These lengths can conveniently be expressed as functions of the dependent coordinates.

4.2.2.1 The stability of the internal dynamics

In the followings, the internal stability of the planar Acroboter model will be analyzed by applying the method of blended constraints in the form of Eq. (4.1). In the presented test case the planar Acroboter is commanded to follow a desired trajectory with horizontal orientation and the CC is required to be above the SU at the relative height $h_{\mathrm{CC}}^{\mathrm{d}}$. The passive (lateral) motion of the CC is not specified by the servo-constraints, hence this motion constitutes the internal dynamics. The original and modified-stabilizing servo-constraints that describe the desired trajectory are given by

$$\widehat{\boldsymbol{\gamma}} = \begin{bmatrix} y_{\mathrm{CC}} - \frac{y_3+y_4}{2} - h_{\mathrm{CC}}^{\mathrm{d}} \\ \frac{x_3+x_4}{2} - x_{\mathrm{SU}}^{\mathrm{d}} \\ \frac{y_3+y_4}{2} - y_{\mathrm{SU}}^{\mathrm{d}} \\ y_3 - y_4 \end{bmatrix} \text{ and } \boldsymbol{\gamma}_s = \begin{bmatrix} y_{\mathrm{CC}} - \frac{y_3+y_4}{2} - h_{\mathrm{CC}}^{\mathrm{d}} \\ x_2 - x_{\mathrm{SU}}^{\mathrm{d}} \\ \frac{y_3+y_4}{2} - y_{\mathrm{SU}}^{\mathrm{d}} \\ y_3 - y_4 \end{bmatrix} . \tag{4.21}$$

The introduced dynamical model uses independent coordinates, thus for the analysis of the internal dynamics apart from eigenvalues which belong to the servo-constraints here the eigenvalues which belong to geometrical constraints are also have to be discarded.

In general in the dynamical model n number of coordinates are used, among which m number of geometric conditions appear and the dimension of the task is l. Because of the first order form

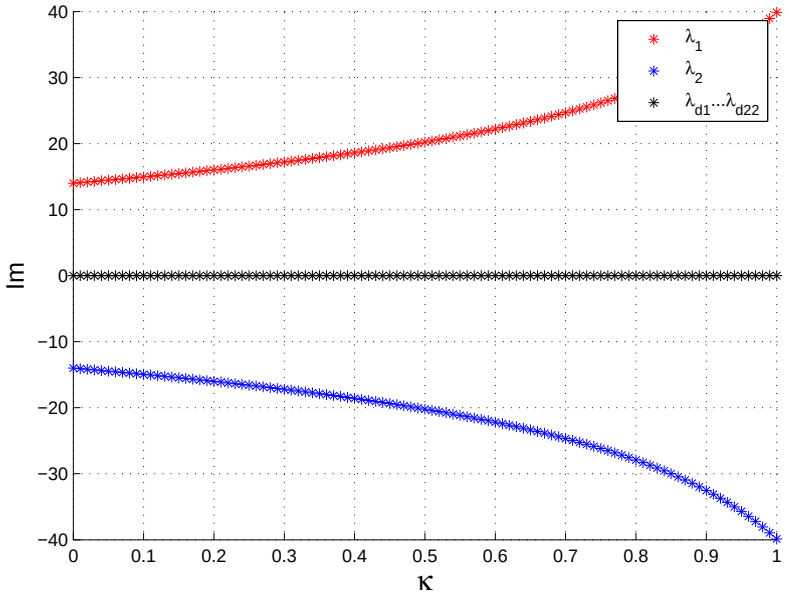

FIGURE 4.10. Eigenvalues of the internal dynamics in case of the Acroboter system

$2\,(l+m)$ eigenvalues have to be discarded and the remaining $2(n-l-m)$ eigenvalues characterize the internal dynamics if the relative degree is 2 for all input-output pairs.

Based on Eq. (2.21) the equation of the specified motion can be formulated as

$$\begin{bmatrix} \mathbf{M} & \mathbf{\Phi}^{\mathrm{T}} & -\mathbf{H} \\ \mathbf{\Phi} & \mathbf{0} & \mathbf{0} \\ \mathbf{\Gamma} & \mathbf{0} & \mathbf{0} \end{bmatrix} \begin{bmatrix} \ddot{\mathbf{q}}_{\mathrm{d}} \\ \boldsymbol{\lambda} \\ \mathbf{u} \end{bmatrix} = \begin{bmatrix} -\mathbf{c} + \mathbf{Q}_{ex} \\ -\dot{\mathbf{\Phi}}\dot{\mathbf{q}} - \dot{\boldsymbol{\pi}} - a_2\dot{\boldsymbol{\varphi}} - a_1\boldsymbol{\varphi} \\ -\dot{\mathbf{\Gamma}}\dot{\mathbf{q}} + \dot{\mathbf{g}}(t) - a_2\dot{\boldsymbol{\gamma}} - a_1\boldsymbol{\gamma} \end{bmatrix}, \tag{4.22}$$

where a_1 a_2 terms are the sensitivity analysis parameters used for separating the physical and artificial eigenvalues due to the applied redundant parametrization.

From the Eq. (4.22) the admissible accelerations can be expressed. Similarly to Eq. (3.5) it can be linearized around the investigated $\mathbf{x}_e = [\mathbf{q}_e, \dot{\mathbf{q}}_e]^{\mathrm{T}}$ with the corresponding desired output $\mathbf{h}$. Then the eigenvalues of the linearized system have to be computed as it is detailed in Sec. 3.1.

In case of the planar model of the Acroboter the number of descriptor coordinates is $n = 6$, and $m = 1$ geometric constraint is defined Eq. (4.17) and the dimension ot task is $l = 4$ (Eq. (4.21)), thus 2 eigenvalues belongs to the 1 dimensional internal dynamics.

Analysis of the internal stability was carried out in the hanging down (zero nutation) position. The corresponding generalized coordinate values are $\mathbf{q}_e = [0,\ -1,\ -0.25,\ -1.5,\ 0.25,\ -1.5]^{\mathrm{T}}\,\mathrm{m}$ and based on the servo-constraint Eq. (4.21) the desired output is $\mathbf{h} = [0.5\,\mathrm{m},\ 0\,\mathrm{m},\ -1.5\,\mathrm{m},\ 0\,\mathrm{m}]^{\mathrm{T}}$ (4.21). Similarly to the Cart-pole example the eigenvalues of the internal dynamics are calculated as the function of the coupling term κ (see Eq. (4.1)).

The Fig. 4.10 shows the eigenvalues of the internal dynamics (λ_1, λ_2) and the eigenvalues of the driven dynamics ($\lambda_{d1} \ldots \lambda_{d22}$), which could be discarded as it is proposed in Sec. 3. In the dynamical model of the Acroboter planar model the damping is not considered, the eigenvalues have only imaginary parts and in this case λ_1, λ_2 are complex conjugate pairs. It can be concluded that the internal dynamics is marginally stable in the full range of κ. The vibration frequency of the internal dynamics is the highest when $\kappa = 1$.

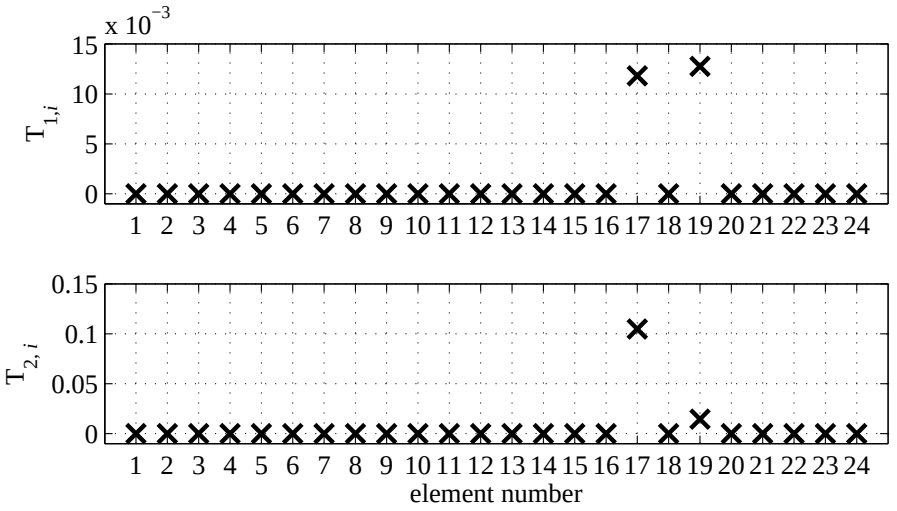

FIGURE 4.11. Elements of the Jacobian matrix **T** in case of the Acroboter system

4.2.2.2 The stability behaviour of the discrete controlled system

For the case of sampled data control realization the stability investigation was also carried out in the hanging down (zero nutation) position as it is proposed in Sec. 4.2.2.1. The sampling time was $T_s = 0.01\,\mathrm{s}$. In reference [19] the stability investigation of this system is carried out with coordinate transformation for the elimination of the constraints. That procedure required the selection of a new set of independent coordinates, which is required for the a priory and intuitive selection of the parametrizing minimum set of generalized coordinates. Furthermore, this coordinate transformation was numerically relatively expensive. Here the stability charts were calculated by discarding the non-physical eigenvalues using sensitivity analysis (see Sec. 3.2). During the elimination process 2 eigenvalues have to eliminated because one geometric constraint exists. It means that $2\,m = 2$ eigenvalues are sensitive for the change of the parameters of the sensitivity function. As a confirmation Fig. 4.11 shows the elements of the Jacobian **T** (3.9) at an arbitrarily selected point, which shows that the sensitivity function has effect on these 2 eigenvalues only.

The stable regions are shown in the plane of the control parameters K_P and K_D at different fixed values of κ in Fig. 4.12. In Fig. 4.12 the same shades of gray belong to the same ranges of the spectral radii $\rho = max(\mu_i)$. With the DAE based eigenvalue analysis technique the averaged computation time of the presented stability charts was $t_{comp} = 1823\,\mathrm{s}$, while the independent coordinate based calculation [19] which uses trigonometrical functions for the transformations requires $t_{comp} = 2420\,\mathrm{s}$. Both computations are made in MATLAB [27] environment on PC with an Intel Core i7-5500 processor. During the computations only the MATLAB ran. The presented values are the averaged value of ten computations in each case.

Based on the stability charts it can be concluded that the system could be stable with original servo-constraints $\widehat{\gamma}$ but introducing of the stabilizing term γ_s has a positive effect on the stability. The stable domains of control parameters are the largest when $\kappa = 0.9$ and has the minimum spectral radii $\rho_{min} = 0.96$. Fastest decay is characterized by $\rho_{min} = 0.94$ and it can be achieved at $\kappa = 0.8$.

4.2.2.3 Trajectory tracking simulations

In order to validate the usability of the proposed controller and demonstrate the vibration attenuation of the investigated controller, a numerical simulation was carried out. In the numerical simulation

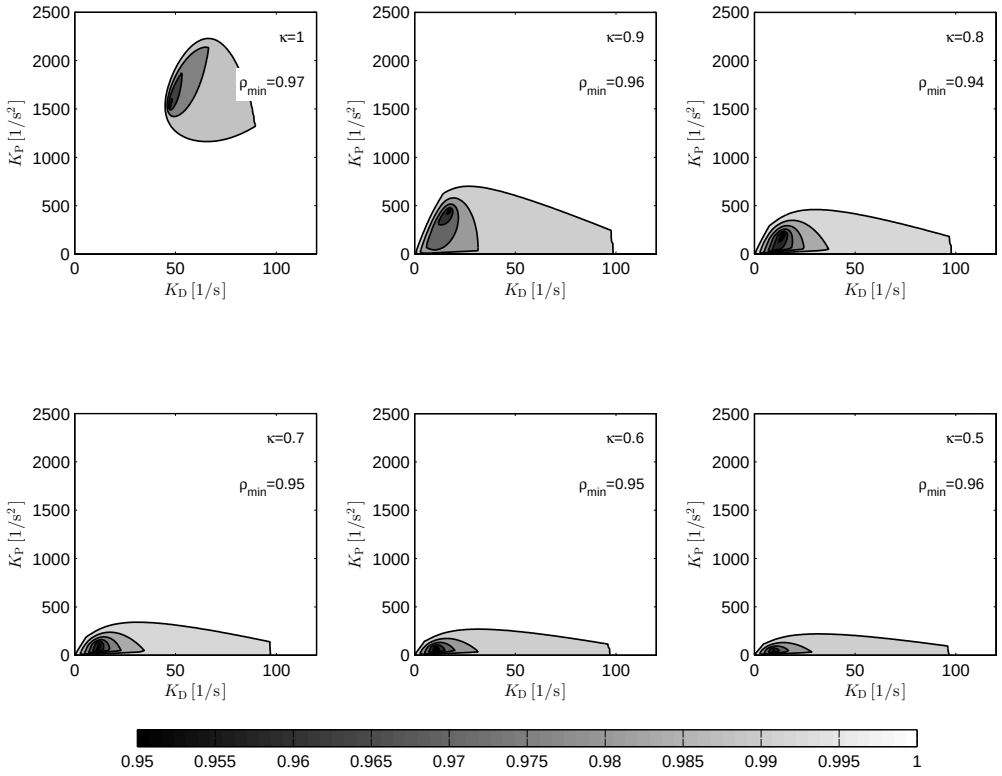

FIGURE 4.12. Stability charts of the Acroboter system

study the desired parameters x^d_{SU} and y^d_{SU} of Eq. 4.21 are prescribed such that the planar Acroboter model has to follow a linear path with trapezoidal velocity profile. The starting point located at $x^d_{\mathrm{SU}}(0) = 0\,\mathrm{m}$, $y^d_{\mathrm{SU}}(0) = -1.5\,\mathrm{m}$ and the endpoint $x^d_{\mathrm{SU}}(5) = 0.5\,\mathrm{m}$, $y^d_{\mathrm{SU}}(5) = -1\,\mathrm{m}$ have to be reached after 5 s. Then the system has to stay in rest until the end of the simulation ($t_{END} = 8\,\mathrm{s}$). During the motion the vertical distance between the cable connector and the swinging unit is required to be constant with a prescribed value of: $h^d_{\mathrm{CC}} = 0.5\mathrm{m}$. During the evaluation of the task the maximal velocity is $v_{max} = 0.5\,\mathrm{m/s}$ while the maximum allowed acceleration is $a_{max} = 0.25\,\mathrm{m/s}^2$. In this study three simulation studies will be introduced.

In the first simulation scenario the control input $\mathbf{u}$ was computed using the original servo-constraints $\widehat{\boldsymbol{\gamma}}$ and the stabilizing terms $\boldsymbol{\gamma}_s$ were not applied. This corresponds to the selection of $\kappa = 1$. Then the fastest decay is provided by $K_{\mathrm{P}} = 1500[1/\mathrm{s}]^2$ and $K_{\mathrm{D}} = 47[1/\mathrm{s}]$ (see: Fig. 4.12). The Fig. 4.13a shows the initial and final configuration of the system and the recorded path of the representative points (P_1, P_2, P_3). The violation of the servo-constraints tends to zero during the simulations which are illustrated in Fig. 4.14a. The control force histories which also show the stable operation, are depicted in Fig. 4.14b. In Fig. 4.14a γ_2 and γ_3 show the time history of the positioning error of the swinging unit in horizontal and vertical direction respectively. The maximal value is less than 2mm in both directions. The trapezoidal nature of the errors is caused by the prescribed trapezoidal velocity profile. The maximal relative height error γ_1 of the cable connector is also less than 2mm. The inclination (relative vertical position of the edges) of the swinging unit represented by γ_4 is less than 0.1mm during the whole simulation.

In order to check the robustness of the controller in the second simulation scenario a perturbation is modelled. The external accidental perturbation can disturb every controlled system but it is

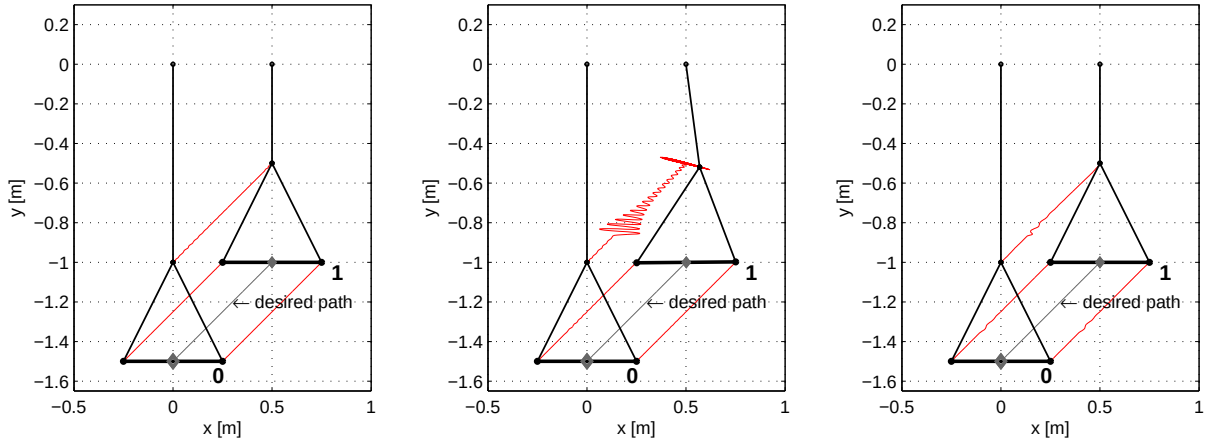

(A) 1. scenario (B) 2. scenario (C) 3.scenario

FIGURE 4.13. Simulational results

specially true for the Acroboter system, as the introduced robot is a service robot and it has to work in an everyday environment closed cooperation with the humans. Considering a human collision as a possible perturbation a horizontal perturbation force (5 N) was applied on the cable connector between $t = 1.0\,\mathrm{s}$ and $t = 1.2\,\mathrm{s}$.

First the control parameters remained the same as in the previous simulation. Fig. 4.13b shows that the applied perturbation could excite the marginally stable internal dynamics and as a result the cable connector developed unacceptable vibrations. The corresponding servo-constraint violations and the applied control forces are shown in Fig. 4.15.

In the third simulation the same perturbation is applied, but the blended servo-constraints are applied according to Eq. (4.1). Using the results of stability investigation the coupling term is selected as $\kappa = 0.8$ and the control gains were $K_\mathrm{P} = 200[1/\mathrm{s}]^2$ and $K_\mathrm{D} = 22[1/\mathrm{s}]$. The results clearly show that despite the perturbation the system operates in a stable way (see Fig. 4.13c and Fig. 4.16) In Fig. 4.13c γ_2 shows the horizontal position error which maximal value is 10 mm. In the vertical direction the maximal servo-constraint violation γ_3 is 3 mm. The peak value of γ_1 is less than 10 mm. Finally the peak value of inclination error γ_1 is 0.5 mm only. Comparing to the first simulation the errors are significantly higher, but on the other hand with application of the blended servo-constraint the control could work in a stable way despite the disturbance.

4.2.3 Concluding remarks

As it is shown in case of the control design of underactuated mechanical systems the internal dynamics have to be taken in to account. Instead of partitioning the controlled (driven) and internal dynamics a new approach was proposed which uses the stability investigation technique of DAE systems (see Sec. 3.1). In order to ensure the stability of the internal dynamics a systematic technique called as the method of blended servo-constraints is introduced. This method combines the controlled and the originally non-controlled (internal) dynamics. This method is applied in case of a sliding pendulum benchmark example. Beside the numerical stability analysis of the internal dynamics and whole controlled system an experimental study was carried out. The experimentally observed dynamical

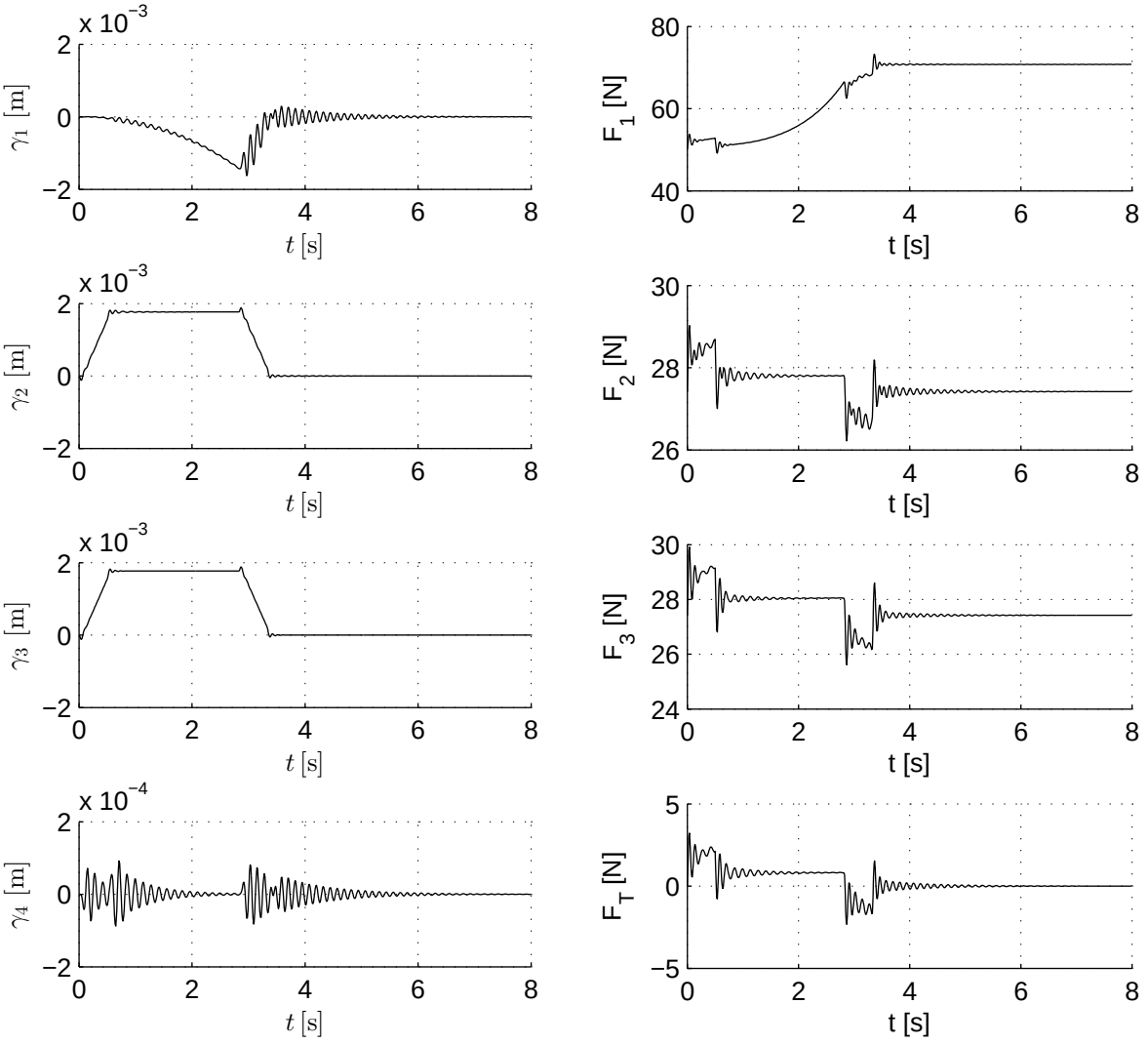

(A) Servo-constraint violation (B) Applied control forces

FIGURE 4.14. Simulational results at $\kappa = 1$

behaviour was consistent with the presented stability analysis. A good qualitative agreement could be shown between the simulated and real motions. A similiar numerical study was carried out in case of the Acroboter platform. Based on the numerical simulations it can be concluded that with the application of the blended method the system can compensate the possible disturbance of the environment effectively.

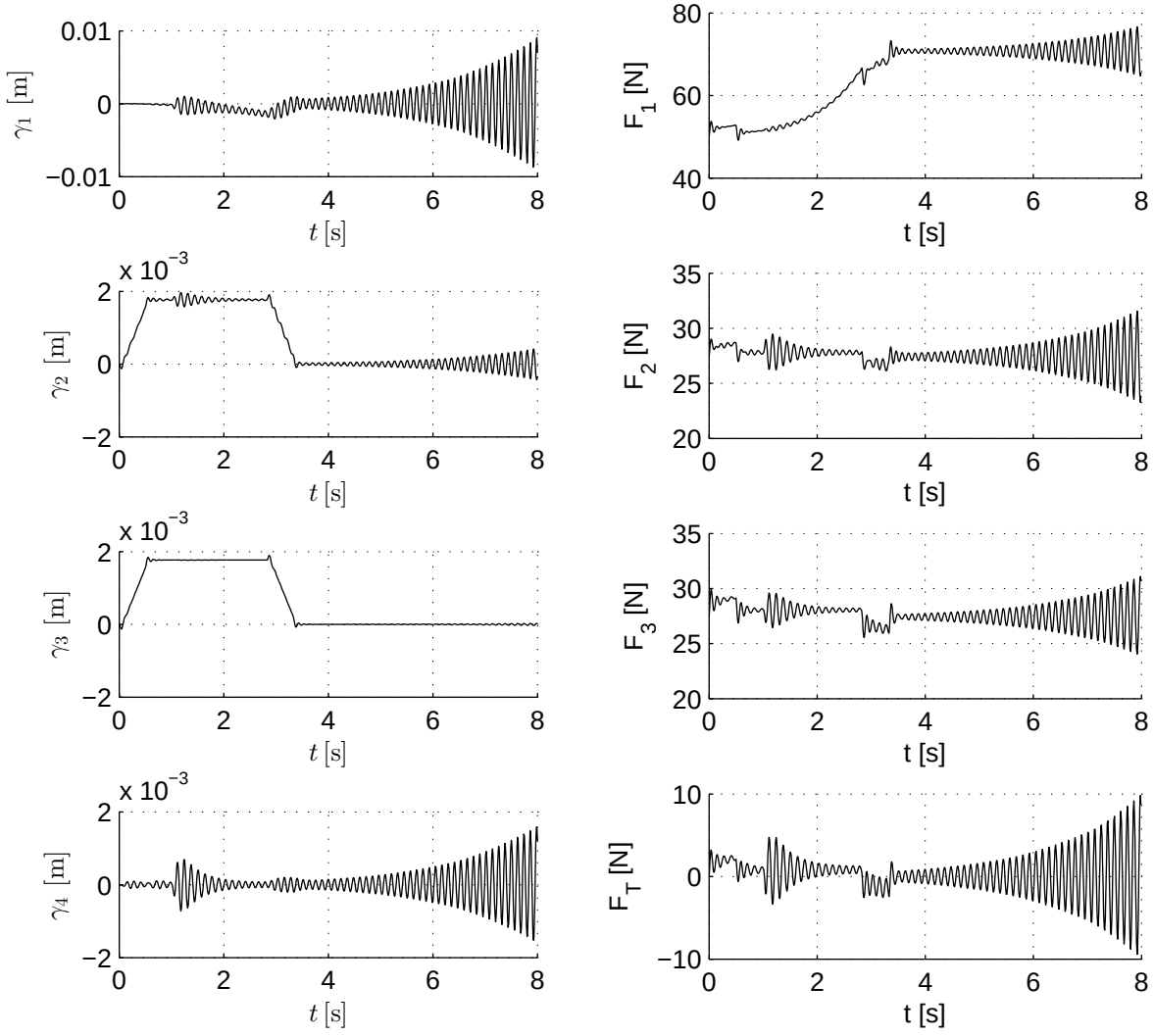

(A) Servo-constraint violation (B) Applied control forces

FIGURE 4.15. Simulational results with perturbation at $\kappa = 1$

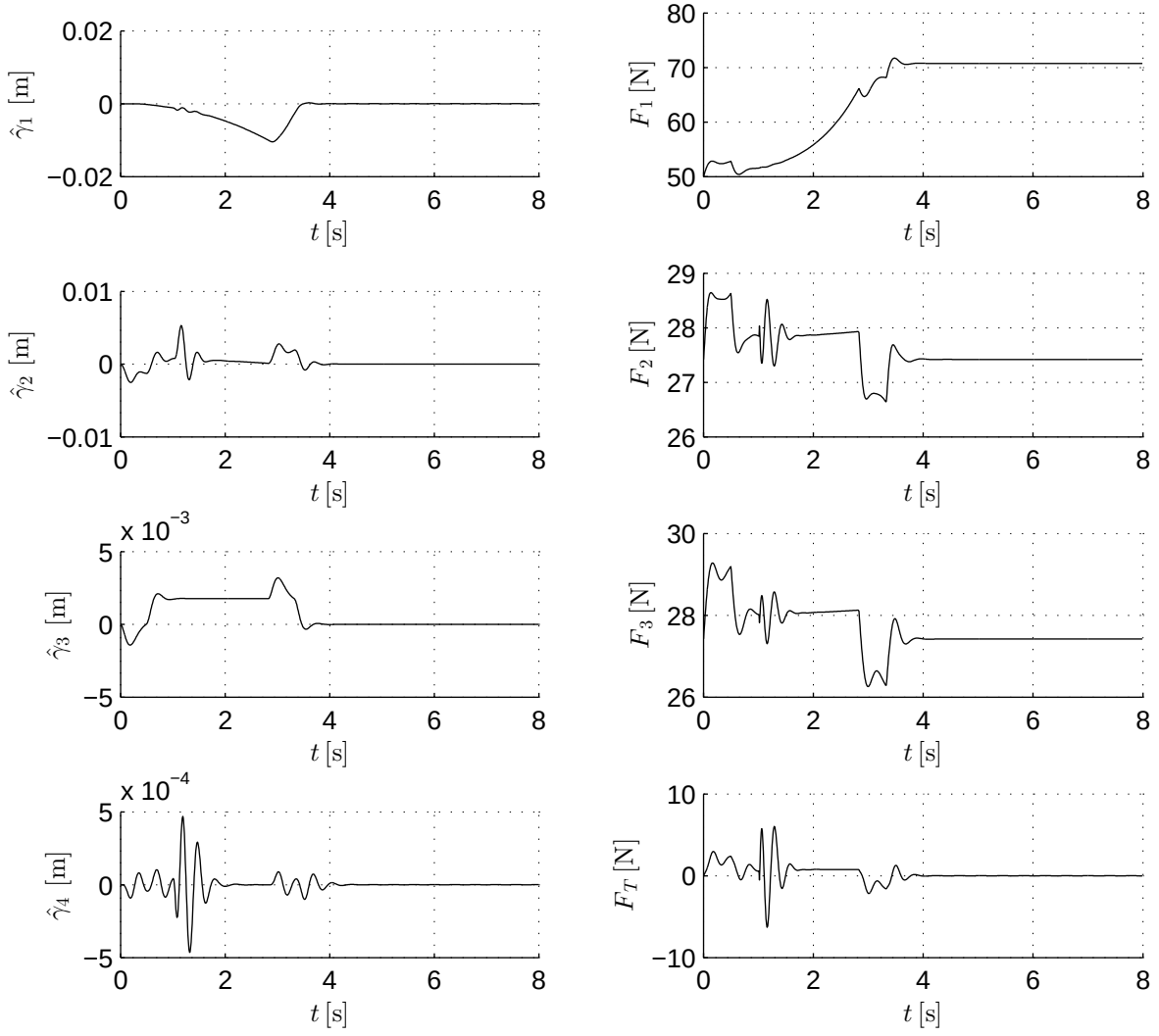

(A) Servo-constraint violation (B) Applied control forces

FIGURE 4.16. Simulational results with perturbation at $\kappa = 0.8$

4.3 New results

In underactuated systems unstable internal dynamics may exist, which makes the classical computed torque trajectory tracking impossible. It is possible to overcome this problem with the following technique which called as the method of blended servo-constraints. The application of the method was demonstrated by simulation using the sliding pendulum benchmark example, and the method was successfully applied for the trajectory control of the same system in an experiment. Furthermore, the method was proved to be useful in the trajectory tracking control of the underactuated service robot Acroboter.

Thesis 2.

The method of blended servo-constraints uses two different sets of servo-constraints: one of these, $\widehat{\boldsymbol{\gamma}}$, describes the desired trajectory, while the other one, $\boldsymbol{\gamma}_s$, modifies the original task such that their linear combination $\boldsymbol{\gamma} = \kappa\,\widehat{\boldsymbol{\gamma}}+(1-\kappa)\boldsymbol{\gamma}_s$ becomes feasible, where κ is an adjustable parameter that can be used to find the balance between accuracy and stability. The stabilizing servo-constraint set $\boldsymbol{\gamma}_s$ must contain the desired values of the coordinates that corresponds to the original internal dynamics.

In case of the sliding pendulum the fastest decay of the oscillations induced by the internal dynamics can be achieved if $\kappa = 0.6$, while in case the Acroboter robot the fastest decay corresponds to the value $\kappa = 0.8$.

Related journal publication:

L.L. Kovács and L. Bencsik, "Stability case study of the acroboter underactuated service robot," *Theoretical and Applied Mechanics Letters*, vol. 2, no. 4, 2012, (Article 043004).

Other related publications:

[79], [80], [81], [82], [83], [84].

Chapter 5

The method of periodically varied servo-constraints

While the geometric constraints are naturally satisfied in a physical system, the servo-constraints are often violated, which violation itself constitutes the control error. Moreover, in certain situations, the internal dynamics of the controlled system can be unstable which prevents the realization of the control task. A possible way to handle this problem is to modify the original servo-constraints in order to get a realizable task. Often the original task is modified by using a linear combination (see Eq. (4.1)) of the original and new servo-constraints that aim to stabilize the internal dynamics of the system. As it was shown in Chapter 4 this is possible by using the linear combination of the original and a suitably selected new set of servo-constraints. In the followings, a new approach will be proposed, which is the method of periodically varied servo-constraints. For short in the following the method is called as the 'method of periodic servo-constraints '.

Dealing with periodic control is motivated by the positive effect of periodic excitations. Since a properly chosen frequency can help in balancing problems [85]. The swing-up problem of an inverted pendulum can be solved with periodic control also [86–88]. In the act-and-wait control strategy [89] the control action is periodically interrupted with a waiting phase when the effect of the control action can be observed. Furthermore in [90] it is shown that the periodic variation of the control gains could improve the dynamical behaviour of the system, and could stabilize the motion successfully.

Based on this previous good practices the main goals of this chapter are to introduce the concept of the periodic servo-constraints, investigate their dynamic effects, and provide details on their implementation in trajectory tracking control tasks. To find the stable control parameters is also among the main objectives. The usefulness of the method is illustrated by two examples. The periodic controllers are implemented for the trajectory tracking control of the previously used sliding pendulum and planar Acroboter model.

5.1 Periodically varied servo-constraints

The servo-constraint based formalism explained in Sec. 2.2 makes it possible to divide the dynamics of underactuated multibody systems into two parts: the controlled dynamics, which is described by the servo-constraints, and the internal dynamics [20], which cannot directly be influenced by the servo-constraints. In order to avoid the unstable internal dynamics in Chapter 4 a new set of servo-constraint was introduced which was linearly combined with the original servo-constraints. This

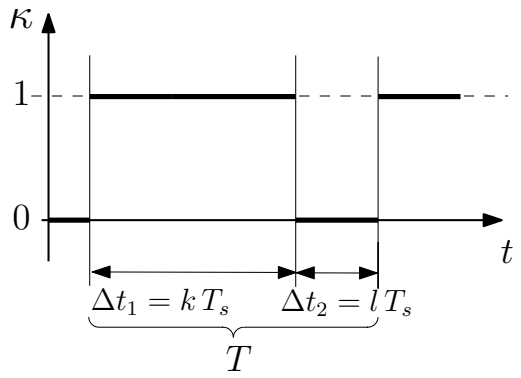

FIGURE 5.1. Servo-constraint switching scheme

linear combination remained the same for the whole duration of the controlled motion see Eq. (4.1). The resulting system was stable and the modified task could be realized with tolerable trajectory following error with respect to the original desired trajectory.

Here an alternative approach is introduced, when the servo-constraints are not simply modified but also periodically changed in time as it is shown in Fig. 5.1. The switching of the servo-constraint is mathematically formulated as

$$\boldsymbol{\gamma} = \kappa(t)\,\widehat{\boldsymbol{\gamma}} + (1-\kappa(t))\boldsymbol{\gamma}_s\,, \tag{5.1}$$

where $\widehat{\boldsymbol{\gamma}}$ is the vector original servo-constraints and $\boldsymbol{\gamma}_s$ represents a new set of servo-constraints, which help to stabilize the internal dynamics. In addition, κ is a time dependent switching parameter. When $\kappa = 1$ the original servo-constraint $\widehat{\boldsymbol{\gamma}}$ is taken into account in a certain fraction of the time period. The controller aims to accurately realize the desired motion during this time interval. The switching parameter $\kappa = 0$ is zero the typically shorter remaining fraction of the time period. A modified servo-constraint $\boldsymbol{\gamma}_s$ is applied during this time interval, and the controller tries to stabilize the unstable internal dynamics, while the realization of the desired task becomes temporarily a secondary objective. The control period in Fig. 5.1 is an integer multiple of the sampling period, T_s, of the digital controller. For k sampling periods $\kappa = 1$ and the original task is realized, and for l sampling periods $\kappa = 0$ and the stabilization of the internal dynamics is in focus.

Instead of small, but permanent modification of the original task, here, the goal is to only change the servo-constraints temporarily, and via that, stabilize the internal dynamics of the controlled system with smaller deviations from the original task.

In the followings, a stability investigations will be carried out in case of the earlier mentioned examples for the selection of the switching pattern.

5.2 Stability analysis of the periodic control

During periodic control the required control torque is also calculated by using the computed torque control method (see Eq. (2.20) or Eq. (2.21)), but one has to consider that the servo-constraints (5.1) can change from one sampling period to the other. For the selection of the control parameters and how the servo-constraints should change, the stability of the system is analyzed assuming a discrete-time controller. When the servo-constraints do not change it is enough to determine the discrete mapping Eq. (3.17) which connects states of the system in two constitutive sampling instants.

In contrast here the control law is switched in time, therefore the transition matrix is also changed during the control. Thus for the stability analysis, the transition matrix has to be derived for the whole time period. It could be determined by combining the solutions as

$$\mathbf{z}_{n+k+l} = \widehat{\mathbf{C}}\,\mathbf{z}_n, \text{ where } \quad \widehat{\mathbf{C}} = \prod_{j=1}^{k+l} \mathbf{C}_{n+k+l-j}. \tag{5.2}$$

The proposed controller initially takes k steps with the original servo-constraints and then l steps with the modified ones. Then the transition matrix of one period is

$$\widehat{\mathbf{C}} = \mathbf{C}(\kappa{=}1)^k\, \mathbf{C}(\kappa{=}0)^l\,. \tag{5.3}$$

The eigenvalues of $\widehat{\mathbf{C}}$ characterize the dynamical behaviour over one period which takes $k+l$ steps. The condition of the stability remains the same, namely all of the eigenvalues μ_i have to be located in a unit circle of the complex plane. But in order to compare the decay rate of the periodically controlled system with that of a conventionally (non-periodic) controlled system a new measure have to be introduced, which can characterize the decay of a single sampling (T_s). Thus from the spectral radii ρ [59] the decay index which is the average decay can be computed as [89]

$$\bar{\rho} = \sqrt[(k+l)]{\rho}\,. \tag{5.4}$$

For large complex multibody systems the calculation of matrix $\mathbf{C}$ is computationally expensive. However it is enough to compute these for a single time step at $\kappa = 0$ and $\kappa = 1$; then the stability of different periodic patterns can be investigated.

The decay index $\bar{\boldsymbol{\rho}}$ of $\widehat{\mathbf{C}}$ can be used for determining stability behaviour as it is discussed in Sec. 3.2.

5.3 Representative benchmark and real world problems

5.3.1 Sliding pendulum

This section revisits the sliding pendulum example discussed earlier. A new periodic controller is applied and the results are compared to the Sec. 4.2.1). In Sec. 4.2.1 it is shown that the internal dynamics is unstable when the endpoint of the pole is controlled. Here first the stability of the controlled system will be analyzed, then it will be shown that with application of the periodic servo-constraint the trajectory following error will be smaller.

System stability

In the stability investigation of the digitally controlled system the mechanical parameters were the same as the parameters used in Sec. 4.2.1. The aim of the stability investigation is to discover the stability behaviour of different periodic patterns. The parameters of the stability calculation were the control gains K_P, K_D (see Eq. (2.21)) and the ratio of the application time of the original servo-constraints $\widehat{\gamma}$ and the stabilizing terms $\boldsymbol{\gamma}_s$. In the study the application time of the original servo-constraints was varied $k = (1,2,..,10)$, while the stabilizing terms in every case were applied for $l = 5$ steps. The different stability charts are determined in plane of proportional K_P and derivative K_D gains at fixed periodic pattern. The eigenvalues of the transition matrices are computed in

300×300 points of the charts. The controlled system is considered stable when the decay index $\hat{\rho}$ is less than one. The stability charts are presented in Fig. 5.2. In Fig. 5.2 the same shades of gray belong to the same ranges of decay index $\bar{\rho}$. In the charts the fastest decaying transient belongs to the smallest decay index $\bar{\rho}_{min}$. Among these $\bar{\rho}_{min} = 0.93$ is the smallest which corresponds also to $k = 2$ at $K_{\mathrm{P}} = 169[1/\mathrm{s}]$ and $K_{\mathrm{D}} = 15[1/\mathrm{s}^2]$. In this case the original servo-constraint $\widehat{\boldsymbol{\gamma}}$ is replaced by $\boldsymbol{\gamma}_s$ for $l = 5$ steps in every second sampling period. The other performance measure could be the area of the stable domains. Since in case of larger stable domains, since the parameter uncertainties cause instability with less probability. The area of the stable domains i.e., $\rho \leq 1$, were determined by numerical integration using the Greens theorem [91]. It can be concluded that the stable domain is the largest, when $k = 2$. In that case the control parameters can be chosen from the widest range.

The internal stability calculation resulted that the coupling of the original constraints and the stabilizing terms have to be $\kappa < 2/3$ (see Sec. 4.2.1.1). Here we can see that in case of the $k = 10$ and $l = 5$ there are no domains of stable parameters and in case of $k = 9$ and $l = 5$ there is a very small domain of stable control parameters. Thus for the whole period the averaged value of the switching function $\kappa(t)$ have to be less than $2/3$ $(l/(k+l))$ also. It could be concluded that the boundary of the application of the periodic servo-constraints is basically the same with the boundary of the blended servo-constraint based method (see Sec. 4.2.1.2).

Compared to the blended servo-constraints here faster decay can be achieved while there the smallest spectral radii was $\rho_{min} = .95$ a here the smallest decay index is $\bar{\rho}_{min} = .93$. In case of the periodic servo-constraint, the maximal area of stable domains is $\widetilde{A}_{periodic} \approx 6.7 \cdot 10^3[1/\mathrm{s}^3]$ and in case of the blended servo-constraints it is $\widetilde{A}_{blended} \approx 1.2 \cdot 10^3[1/\mathrm{s}^3]$ only. Thus the maximum area of the stable domains are larger in case of the periodic controller.

Simulation study

In order to confirm the results of the stability investigation a numerical simulation was carried out. In this study the lower end of the rod is commanded to follow a horizontal trajectory. This trajectory is a C^8 continuous polynomial which is defined in Eq. (4.13). This control task and the other circumstances are the same with those in case of the blended servo-constraints (see Sec. 4.2.1.3)

The control parameters are selected based on the results of the stability investigations as $K_{\mathrm{P}} = 169[1/\mathrm{s}]$ and $K_{\mathrm{D}} = 15[1/\mathrm{s}^2]$. In one period of the periodic-control the original servo-constraints are used for $k = 2$ and then it is replaced with the stabilizing terms for $l = 5$ steps. The motion of the controlled point (end of the robot) is shown in Fig. 5.3 where the desired task and result of the blended method are also presented. In Fig. 5.3 it can be seen that the realized motion overshoots on the desired one. The average overshoot is smaller in case of the periodic control which results in smaller trajectory following error. When the periodic controller was applied the maximum trajectory following error is $|\widehat{\boldsymbol{\gamma}}| = 0.0059[\mathrm{m}]$. With the method of blended servo-constraints it is $|\widehat{\boldsymbol{\gamma}}| = 0.0085[\mathrm{m}]$. To quantify the whole motion the Root-Mean-Square (RMS) value [58] is used for the comparison, which can be calculated as:

$$\mathrm{RMS} = \sqrt{\frac{1}{n}\sum_{i=1}^{n}\gamma(t_i)^2}, \tag{5.5}$$

where n is the number of samplings. Based on these values the method of periodic servo-constraints could decrease the error of trajectory tracking with 38% respect to the controller of the previous chapter. The applied performance measures of the periodic servo-constraints and linearly modified servo-constraints are summarized in Table 5.1.

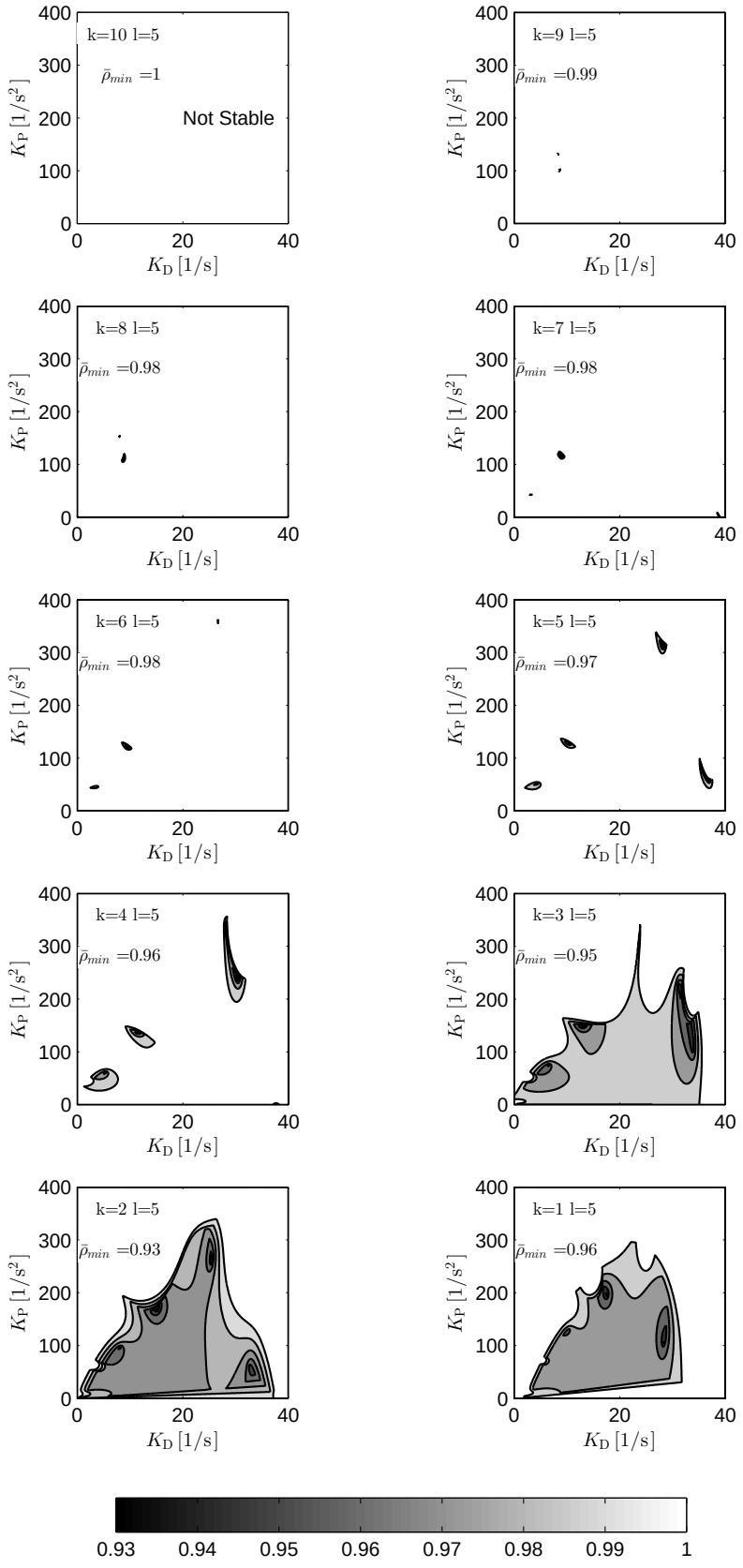

FIGURE 5.2. Stability charts of the sliding pendulum with periodic servo-constraints

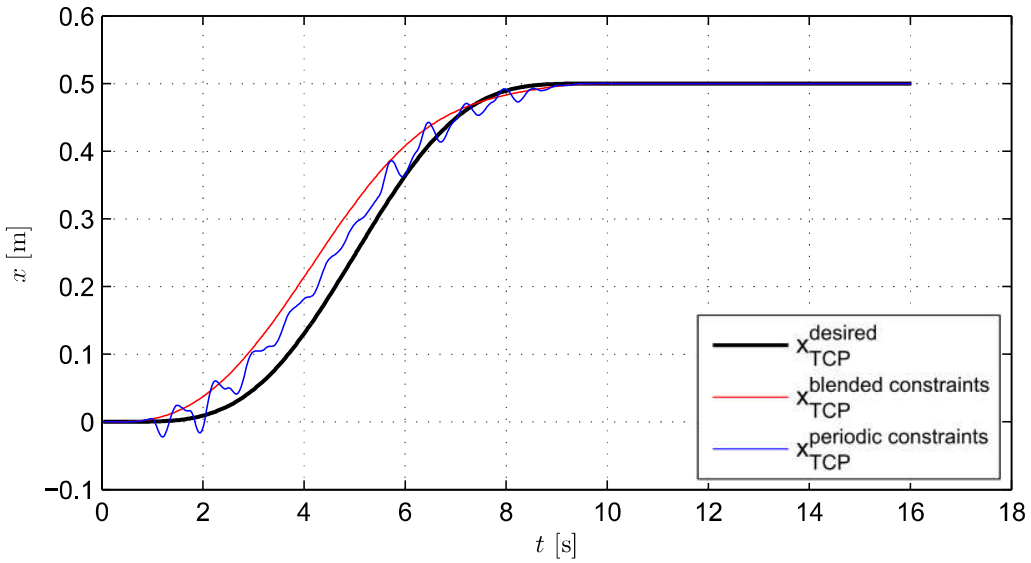

FIGURE 5.3. Simulational results of the periodic servo-constraints in case of the sliding pendulum

TABLE 5.1. Stability and simulation results in case of the sliding pendulum example

	Blended servo-constraints	Periodic servo-constraints
max. area of stable domains $[1/s^3]$	$6.7 \cdot 10^3$	$1.2 \cdot 10^3$
min.(ρ_{min})[-]	0.95	0.93
max($\|\gamma\|$) [m]	0.0085	0.0059
RMS [m]	0.0351	0.0221

5.3.2 The Acroboter service robot platform

In this section the method of periodic servo-constraints is applied to the trajectory following control of the planar model of the Acroboter system introduced earlier in Sec. 4.2.2. The goal here is to show the applicability of a more complex, multibody system parametrized by non-minimum set of generalized coordinates.

System stability

As it was shown earlier in Sec. 4.2.2, the main challenge in the control of the Acroboter system is to stabilize the marginally stable internal dynamics and make the robot move on the desired trajectory at the same time. With the given limited number of actuators these objectives require two different set of servo-constraints: one that is moving the robot on the prescribed trajectory, and an other which stabilizes the internal dynamics while still keeping the controlled point of reference close to the desired path.

The stability investigation was carried out in the hanging down (zero nutation) position. The stability calculation was carried out as it described in Sec. 5.2. Since the generalized coordinates are dependent non-physical eigenvalues appear. Here only one geometric constraint is present. It means that in case of the stability analysis of the sampled system $4\,m = 4$ eigenvalues have to be separated. The basis of the separation of the non-physical eigenvalues again, is that the spurious, non-physical

ones are sensitive to the change of the artificial constraint stabilization gains in Eq. (3.8). Then spectral radii ρ can be selected and depending on the length of the periodic pattern the decay index $\bar{\boldsymbol{\mu}}$ is calculated.

The stability charts in Fig. 5.4 show the stable domains of operation with different k values ($k = 1,2,\ldots,10$) in the space of the control gain parameters K_P and K_D at the fixed number of stabilizing control periods $l = 1$. In Fig. 6.5 the same shades of gray belong to the same ranges of decay index $\bar{\boldsymbol{\mu}}$. The areas of the stable domains were determined by numerical integration using the Green theorem as in case of the sliding pendulum example. It can be concluded that the stable domain is the largest ($\tilde{A}_{per} = 1.4 \cdot 10^5$), when $k = 4$. In that case the control parameters can be chosen from the widest range. The fastest decaying transient belongs to the smallest decay index $\bar{\rho}_{min}$. Among these $\bar{\rho}_{min} = 0.94$ is the smallest which corresponds to $k = 1$ and $K_\mathrm{P} = 367\,1/\mathrm{s}^2$, $K_\mathrm{D} = 28\,1/\mathrm{s}$. It means that the original servo-constraint $\widehat{\boldsymbol{\gamma}}$ is replaced by $\boldsymbol{\gamma}_S$ in every second sampling period.

5.3.3 Trajectory tracking simulations

In order to see the performance of the trajectory tracking in case of the periodic servo-constraints a simulation study was carried out. In the numerical simulation study the planar Acroboter model has to follow a linear path with a trapezoidal velocity profile. The trajectory tracking task is the same as before (see Sec. 4.2.2.3) and it is defined by Eq. (4.21). Similarly to the previous simulation study of the Acroboter platform in order to check the stability of the controlled system a horizontal perturbation force was applied on the cable connector between $t = 1.0\,\mathrm{s}$ and $t = 1.2\,\mathrm{s}$.

In the previous section it was shown that the applied controller results locally in the fastest decaying transients when $K_\mathrm{P} = 1116\,1/\mathrm{s}^2$, $K_\mathrm{D} = 46\,1/\mathrm{s}$ and $k = 4$ and $l = 1$. These parameters corresponds to the smallest decay index (see Fig. 5.4). That stability investigation corresponds to the initial configuration of the simulation task. In the presented simulations scenario basically only the length of the main rope changes. That is the reason why parameters which are optimized for the initial configuration can be used during the whole motion. When there are significant changes in the configuration, the stability investigation have to be carried out in the characteristic points of the trajectory and the different optimized gains can be linked with a gain scheduling technique [92].

The results of the simulation are presented in Fig. 5.5. The violation of the desired tasks, namely the values of the original servo-constraints $\widehat{\boldsymbol{\gamma}}$ are presented in Fig. 5.5a. The results show that the motion of the investigated system could effectively be stabilized around the desired trajectory with the application of the periodic servo-constraints. In Fig. 5.5a $\widehat{\gamma}_2$ shows the horizontal position error which maximal value is 1.5mm. In the vertical direction maximal servo-constraint violation $\widehat{\gamma}_3$ is 1.8mm. The trapezoidal nature of these errors is caused by the prescribed trapezoidal velocity profile. The peak value of $\widehat{\gamma}_1$ is less than 2mm, which represents the vertical displacement error of the cable connector.

Comparing the results of the periodic servo-constraint based and blended servo-constraint based method (see Fig. 4.16 and Fig. 5.5) it can be concluded that the violation of the servo-constraints is significantly smaller in case of the periodic servo-constraints. For comparing this error the RMS trajectory following errors can be used as before. In the multidimensional case it is defined as [58]

$$\overline{\mathrm{RMS}} = \sqrt{\mathrm{RMS}_i^2}, \tag{5.6}$$

TABLE 5.2. Stability and simulation results in case of the Acroboter platform

	Blended servo-constraints	Periodic servo-constraints
max. area of stable domains $[1/s^3]$	$4.9 \cdot 10^4$	$1.4 \cdot 10^5$
min.(ρ_{min})	0.94	0.94
max($\|\gamma\|$) [m]	0.008	0.002
$\overline{\text{RMS}}$ [m]	0.0036	0.0018

where RMS_i corresponds to original servo-constraints $\widehat{\gamma}_1$. In case of the periodic servo-constraints the calculation gives $\overline{\text{RMS}}_{per} = 0.0015$[m] and for the blended servo-constraints it is $\overline{\text{RMS}}_{blended} = 0.0036$[m], which shows significantly smaller average trajectory following error in case of the periodic controller.

Unfortunately, it has to be noted that the periodic switching causes unwanted oscillations. It could be supposed that in case of real application the dynamics of the actuators can suppress these vibration. If it is not enough the zero to one transition in the switching function have to be smoothed.

The performance measures discussed in this section are summarized and compared to the blended method in Table 5.2.

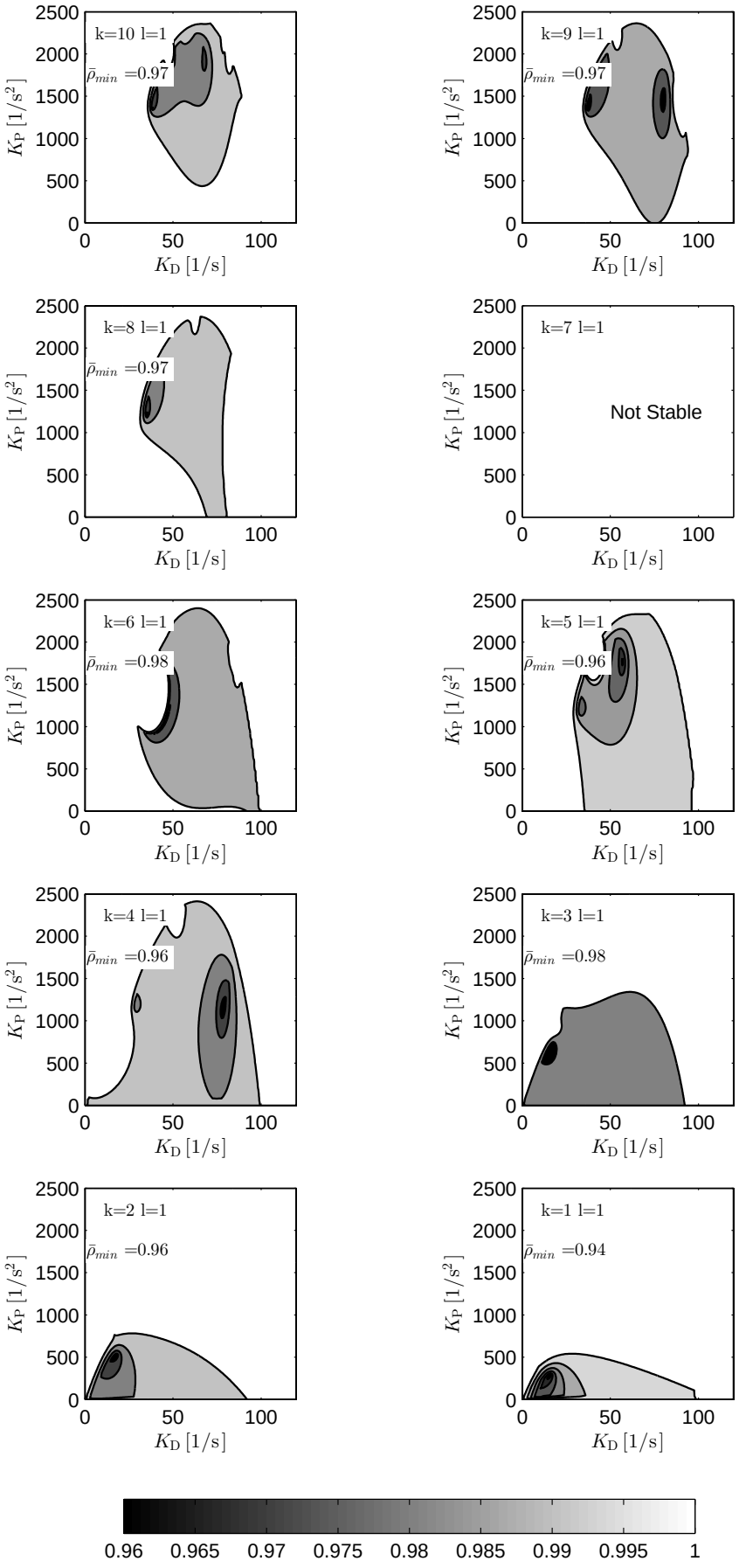

FIGURE 5.4. Stability charts of the Acroboter system with periodic servo-constraints.

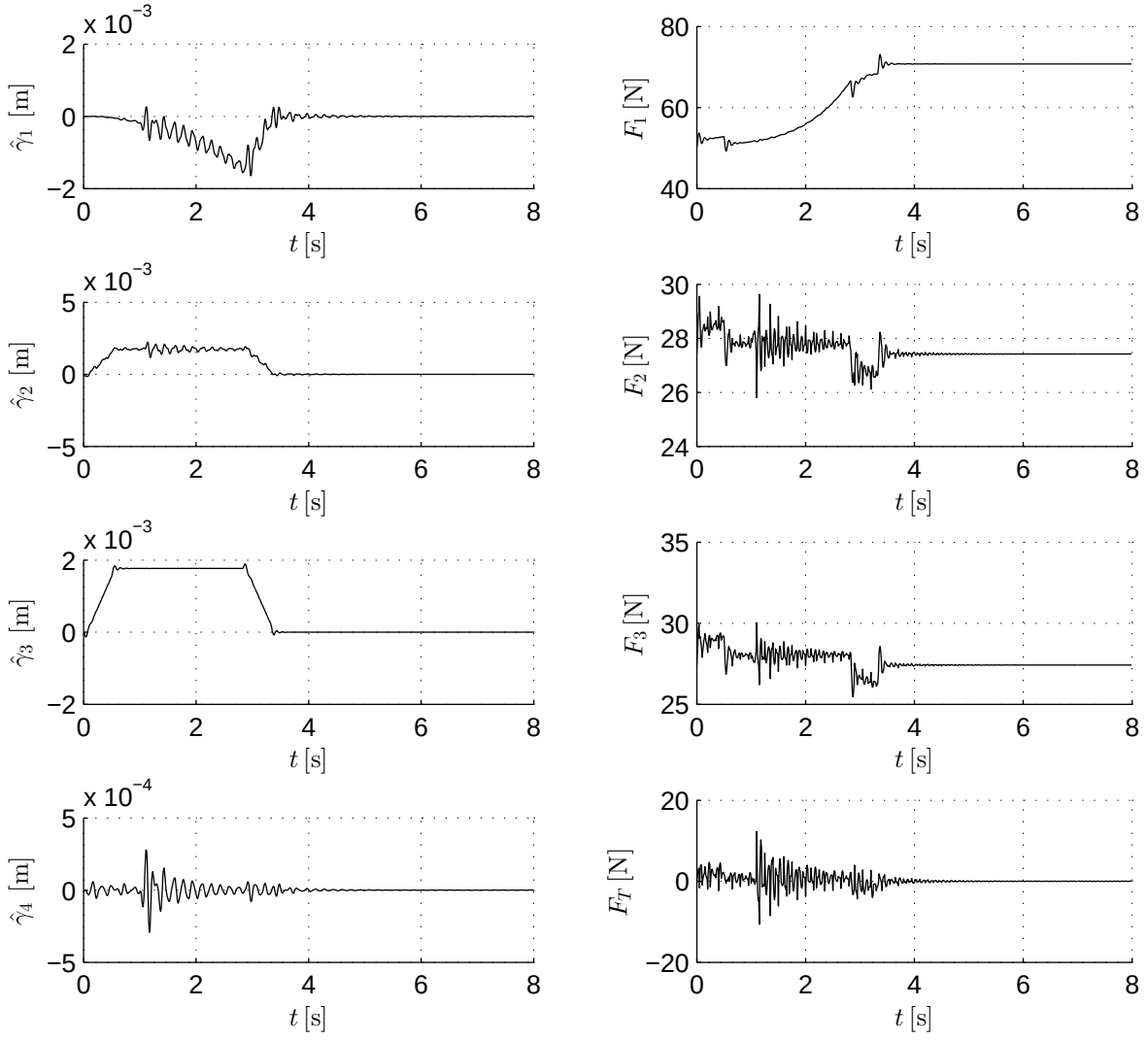

(A) Servo-constraint violation (B) Applied control forces

FIGURE 5.5. Simulational results of the Acroboter system with periodic servo-constraint

5.4 New results

A novel periodically switched controller was proposed for the trajectory tracking control of underactuated mechanical systems with potentially unstable internal dynamics. This technique is called as the method of periodically varied servo-constraints.

The applicability of the method was demonstrated by simulations in case of the sliding pendulum and in case of the Acroboter platform.

Thesis 3.

In the method of periodically varied servo-constraints, the periodic switching between the different control objectives of trajectory following and stabilization is realized by the blended servo-constraints $\boldsymbol{\gamma} = \kappa(t)\,\widehat{\boldsymbol{\gamma}} + (1-\kappa(t))\boldsymbol{\gamma}_s$, where $\widehat{\boldsymbol{\gamma}}$ and $\boldsymbol{\gamma}_s$ represent the original control task and the stabilizing servo-constraints. In addition, $\kappa(t) = \kappa(t+T)$ is a piecewise constant periodic switching function, take only the values of zero or one. It means that within a period, the controller aims to accurately realize the desired motion for a given time and the stabilizing servo-constraints are applied in the rest of the period.

The root mean square value of the trajectory following error is decreased by 37% in case of the sliding pendulum example and it is decreased by 50% in case of the Acroboter platform, when $\kappa(t) = \kappa(t+T)$ periodic switching function is applied instead of the most stabilizing constant κ values.

Related journal publication:

L. Bencsik, L.L. Kovács, and A. Zelei, "Stabilization of internal dynamics of underactuated systems by periodic servo-constraints," *International Journal of Structural Stability and Dynamics*, 2017, 14 pages, paper id: 1740004

Other related publications:

[67], [93].

Chapter 6

Reducing the effect of actuator saturation with periodic control

Actuator saturation occurs when the controller's output exceeds the physical limit of the actuators of a system. In this case the controller can no longer properly realize the desired motion, and as a result, large overshoots and sustained oscillation may develop. These increase the settling time and potentially can lead to an unstable motion. In structured, industrial environments saturation can be prevented by careful trajectory planning based on the well defined task and operational conditions [94]. The use of large, powerful actuators is often also an option. When these are not possible, e.g., in field and service robotics [95] where the environmental conditions and the task are a priori unknown, saturation can result in poor dynamic performance. Performance deterioration resulting from saturation is often called actuator windup [96], and the control methods trying to minimize the undesired effects of saturation are commonly referred to as anti-windup techniques [97–99]. These techniques were originally developed for linear single-input single-output systems [100]. A possible generalization to non-linear multi-input multi-output systems is shown in [101] by using partial feedback linearization. A method that is directly applicable to non-linear mechanical systems is presented in [102].

For trajectory tracking of robotic manipulators, feedback linearization essentially gives the same control forces/torques as the classical computed-torque control method [24] (see Sec. 2.2). Therefore, it is clear that when saturation happens, the nominal computed torques/forces are not available, thus the nonlinear dynamic terms cannot be cancelled entirely and the robot will deviate from the desired trajectory [101, 103]. A common element of the anti-windup control schemes is that the saturating control force is compared to the ideal control force, and based on this, the input of the controller is modified to reduce the trajectory following error. Very often it leads to problem specific and somewhat ad hoc solutions, while model predictive control with constrained optimization can offer a systematic framework to avoid actuator saturation [104]. Inversion of the dynamic model can also make it possible to generate a feed-forward control action, or a modified control input, that eliminates actuator saturation [105, 106].

Instead of taking a preliminary action, in the presented approach the aim is to redistribute the load of the saturating actuator(s) among those which are still functioning in their nominal operating range. This is feasible in robotic systems where typically only a few, but different actuators saturate as the robot follows the commanded end-point trajectory. The posteriori compensation of the effect

of saturation may become necessary when there are unpredictable external forces, which is typical in human-robot interaction scenarios.

Often there are also more actuators available than what the task would require. For example, when cooperating robots are moving an object [107]. Still, depending on the number of saturated actuators, these robots can loose their ability to realize the desired task without redistributing the load on the actuators. In case of a single robot with as many actuators as the task requires, saturation will limit the control capabilities similar to those of the trivially underactuated system with fewer actuators than the degrees-of-freedom.

The following introduced method is a further development of the my co-authored work [108]. In that references, upon saturation the controlled robotic system is considered temporarily underactuated, and a servo-constraint based controller (see: Sec. 2.2) is implemented to distribute the load on the actuators differently with and without actuator saturation. In the saturating phase, a reduced, linearly combined set of servo-constraints is used to minimize the trajectory following error. This is somewhat similar to the method proposed in [101], where the control force is recalculated by preserving the direction of the control action without saturation.

In the following I introduce a periodically switched controller which not only reduces the number of servo-constraints, but also adapts to the dynamics of the system during saturation.

The idea of periodically varied servo-constraint is introduced in the previous chapter (Chapter 5.) There the periodic switching was used for the stabilizing of the internal dynamics. Here the periodic switching makes it possible to regulate all the original servo-constraints over time, one after the other during the saturation, and it may also stabilize the internal dynamics of the temporarily underactuated system.

It will also be demonstrated that a new performance measure, similar to dynamic manipulability, can effectively be used to algorithmically choose and update the periodic control input. The role of this is similar to how gain scheduling [92] accounts for the configuration dependent dynamic behaviour.

6.1 Adaptive periodic control with servo-constraints

When the desired motion is specified in terms of descriptor coordinates Eq. (2.20) or Eq. (2.21) can be solved for the required control efforts as long as there are enough non-saturating actuators to realize the desired motion. When one or more actuators saturate, the solution of Eq. (2.20) or Eq. (2.21) does not provide a feasible control force. Then only a subset of the original servo-constraints can be enforced by the remaining non-saturating actuators, and the system becomes temporarily underactuated with respect to the original task.

The basic problem in implementing a computed torque controller for systems with input torque saturation is that some states of the system will evolve uncontrollably during saturation. The dynamics associated with these uncontrolled states is referred to as the internal dynamics (see Sec. 2.1.3) of the system. It depends not only on the physical properties and the load of a system, but also on the selection of the controlled variables.

Considering sufficiently strong dynamic coupling, a different approach is to implement a switching controller that switches between two or more sets of servo-constraints in a way that the internal dynamics remains stable and the desired trajectory is realized within tolerances.

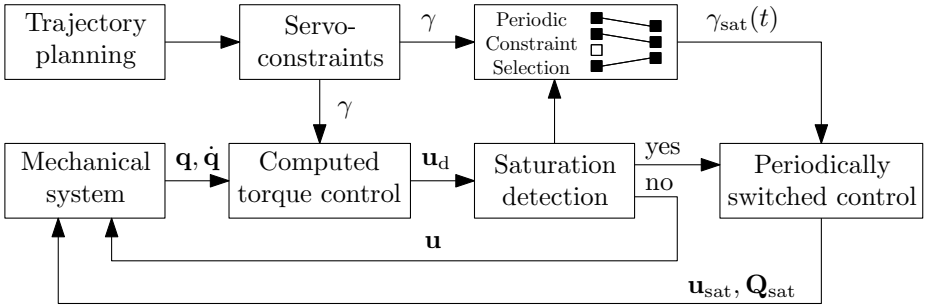

FIGURE 6.1. Block diagram of the proposed controller

A periodically switched controller was successfully applied for the trajectory tracking of different devices previously in (Chapter 5). There the switching pattern and period were selected based on the numerical stability analysis of the systems linearized around a given configuration.

First, the most stabilizing linearly combined inputs were found, and then, the duty cycle of an equivalent periodic controller was constructed.The method relies on local stability results, but can be extended for non-linear systems by using a control parameter scheduling technique [92].

Instead of local stability considerations, here, a more practical method will be proposed which rely only on the actual state of the system, and adjusts the parameters of the periodically switched controller continuously on the course of operation. For system stability, it is assumed that the applied periodic controllers are stable and the parameter update frequency is sufficiently low to let the potentially destabilizing transients dissipate [109]. To determine the time- and update periods of the proposed controller a simulation study will be carried out.

The application procedure of the periodically switched control is outlined in Fig. 6.1. It shows that until saturation occurs the classical computed torque controller is applied (see Sec. 2.2). Then, the number of servo-constraints is appropriately reduced, different sets of servo constraints are formed, and these are varied periodically by a new periodic servo-constraint signal $\boldsymbol{\gamma}_{\text{sat}}(t)$. One possibility to do this is to take the linear combination

$$\boldsymbol{\gamma}_{\text{sat}} = \sum_{i=1}^{N} \kappa_i \, \widehat{\boldsymbol{\gamma}}_i \quad \text{with} \quad \kappa_i(t) = \kappa_i(t+T) \tag{6.1}$$

where array $\boldsymbol{\gamma}_{sat}$ contains a reduced set of servo-constraints with $r < l$ elements, coefficients $\kappa_i(t) = \kappa_i(t+T)$ control the switching between the different sets of servo-constraints with period T, and $N < \binom{l}{r}$ is the number of the considered different sets $\widehat{\boldsymbol{\gamma}}_i$ which are subsets of the original control objectives $\widehat{\boldsymbol{\gamma}}$.

Figure 6.1 also shows that during saturation a reduced size, $r \times 1$, control input $\mathbf{u}_{\text{sat}}$ is considered and the effect of the saturated actuators is represented by the constant external force term $\mathbf{Q}_{\text{sat}}$. With these, and using the subscript *sat* to denote the terms affected by saturation, in case of non- minimum set of coordinates Eq. (2.21) can be rewritten as

$$\begin{bmatrix} \mathbf{M} & \boldsymbol{\Phi}^{\text{T}} & -\mathbf{H}_{\text{sat}} \\ \boldsymbol{\Phi} & \mathbf{0} & \mathbf{0} \\ \boldsymbol{\Gamma}_{\text{sat}} & \mathbf{0} & \mathbf{0} \end{bmatrix} \begin{bmatrix} \ddot{\mathbf{q}} \\ \boldsymbol{\lambda} \\ \mathbf{u}_{\text{sat}} \end{bmatrix} = \begin{bmatrix} \mathbf{Q} + \mathbf{Q}_{\text{sat}} - \mathbf{c} \\ -\dot{\boldsymbol{\Phi}}\dot{\mathbf{q}} - \dot{\boldsymbol{\pi}} \\ -\dot{\boldsymbol{\Gamma}}_{\text{sat}}\dot{\mathbf{q}} + \dot{\mathbf{g}}_{\text{sat}} - \mathbf{K}_{\text{D}}\,\dot{\boldsymbol{\gamma}}_{\text{sat}} - \mathbf{K}_{\text{P}}\,\boldsymbol{\gamma}_{\text{sat}} \end{bmatrix}. \tag{6.2}$$

For a given reduced set of servo-constraints $\boldsymbol{\gamma}_{\text{sat}}$, the required control inputs $\mathbf{u}_{\text{sat}}$ can be calculated based on this equation. For the selection and switching between different, reduced sets of

servo-constraints, a manipulability type performance index is proposed. The performance index is evaluated at certain time instants and a periodic control signal is formed such that more time is allocated for the sets with the higher indices. This way, those servo-constraint sets are prioritized where there is a stronger coupling between the control inputs and the desired accelerations.

The proposed performance index can be introduced by considering the minimum coordinate parameterization of the equation of motion in (6.2) as

$$\mathbf{B}^{\mathrm{T}}\mathbf{M}\mathbf{B}\ddot{\mathbf{p}} + \mathbf{M}\dot{\mathbf{B}}\dot{\mathbf{p}} + \mathbf{B}^{\mathrm{T}}(\mathbf{c} - \mathbf{Q} - \mathbf{Q}_{\mathrm{sat}}) = \mathbf{B}^{\mathrm{T}}\mathbf{H}_{\mathrm{sat}}\mathbf{u}_{\mathrm{sat}}\,, \tag{6.3}$$

where transformation $\dot{\mathbf{q}} = \mathbf{B}\dot{\mathbf{p}}$ defines the new parametrization the same way as the new set of generalized velocities were introduced in Sec. 1.2.1. Note, that $\mathbf{p}$ is conveniently selected as the array of operational space coordinates, the evolution of which are directly prescribed by the servo-constraints. Then, neglecting external forces other than the control input, the linearized equations become

$$\overline{\mathbf{M}}\left(\ddot{\mathbf{p}} - \overline{\mathbf{M}}^{-1}\mathbf{B}^{\mathrm{T}}\mathbf{Q}_{\mathrm{sat}}\right) = \mathbf{B}^{\mathrm{T}}\mathbf{H}_{\mathrm{sat}}\mathbf{u}_{\mathrm{sat}}\,, \tag{6.4}$$

where $\overline{\mathbf{M}} = \mathbf{B}^{\mathrm{T}}\mathbf{M}\mathbf{B}$ is the operational space mass matrix [110], and $\ddot{\mathbf{p}} - \overline{\mathbf{M}}^{-1}\mathbf{B}^{\mathrm{T}}\mathbf{Q}_{\mathrm{sat}}$ is the acceleration due to the non-saturated actuators. By denoting this acceleration with $\bar{\mathbf{a}}$ and introducing $\mathbf{G} = \mathbf{B}^{\mathrm{T}}\mathbf{H}_{\mathrm{sat}}$, the uniformity of the control input to acceleration gain is given by the manipulability ellipsoid [111]

$$\bar{\mathbf{a}}^{\mathrm{T}}\boldsymbol{\mathcal{M}}\,\bar{\mathbf{a}} \leq 1 \quad \text{with} \quad \boldsymbol{\mathcal{M}} = \left(\mathbf{G}^{\dagger}\overline{\mathbf{M}}\right)^{\mathrm{T}}\left(\mathbf{G}^{\dagger}\overline{\mathbf{M}}\right)\,, \tag{6.5}$$

where $\mathbf{G}^{\dagger}$ is the Moore-Penrose pseudo-inverse [44] of the transformed control input matrix $\mathbf{G}$. Also, let $\mathbf{e}_i$ be an l dimensional unit vector, containing r non-zero elements associated with a certain reduced set of servo-constraints. With this, the effect of the control input in a specific direction can be characterized by the performance index

$$z_i = \frac{1}{\sqrt{\mathbf{e}_i^{\mathrm{T}}\,\boldsymbol{\mathcal{M}}\,\mathbf{e}_i}}\,. \tag{6.6}$$

Physically this measure shows the feasible accelerations in the direction of a given servo-constraint set γ_i, and the time to be devoted to the realization of the considered set of servo-constraints within one control period may be obtained as

$$\Delta t_i = \frac{z_i\,T}{\sum_{j=1}^{N} z_j}. \tag{6.7}$$

Thus the activation time Δt_i of a specific servo-constraint set within one period, is proportional to the performance index z_i. Equations (6.6) and (6.7) help to find a physically motivated periodic control signal. This needs to be updated in the course of the motion by considering the current state of the system, or, in off-line calculations, by using the desired values of the servo-constraints.

6.2 Robotic manipulator example

In the followings, as the simplest non-trivial example, we consider the trajectory tracking control of a two-link manipulator. This is similar to the anti-windup control problem of a SCARA robot analysed in [102] and it is often used as a benchmark problem in robot control [94, 103].

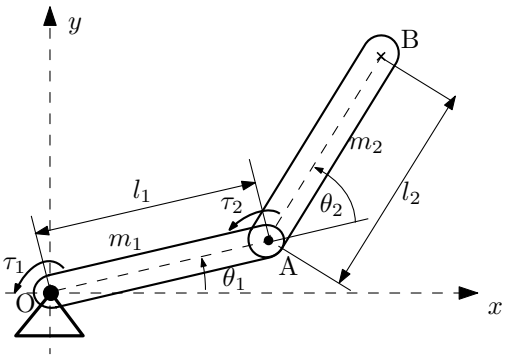

FIGURE 6.2. Two-link planar manipulator

The system shown in Fig. 6.2 has two identical links with $l_1 = l_2 = 0.4\,\mathrm{m}$ and $m_1 = m_2 = 0.2\,\mathrm{kg}$. A homogeneous mass distribution is considered, and the configuration is described by the independent generalized coordinates $\mathbf{q} = [\theta_1, \theta_2]^{\mathrm{T}}$. The manipulator is in the horizontal plane, and its end-effector (point B) is required to follow a circular trajectory with a trapezoidal velocity profile. This is shown in Fig. 6.3 where the base joint of the manipulator is located in the origin, and the circular trajectory is centered at $x = 0$ and $y = 0$. The maximum values of the acceleration and velocity for the trapezoidal velocity profile are $a_{\max} = 1\,\mathrm{m/s^2}$ and $v_{\max} = 0.7\,\mathrm{m/s}$. The corresponding desired operational space trajectories, $x_D(t)$ and $y_D(t)$, are shown in Fig. 6.3. The parameters K_P and K_D in (6.2) are set to $40\,\mathrm{N/m}$ and $30\,\mathrm{Ns/m}$, respectively.When $\tau_{\max} = 0.06\,\mathrm{Nm}$ is selected as the saturation limit for both motors, these parameters ensure that only the first motor will saturate during the prescribed maneuver.

For the considered simple manipulator it is straightforward to derive the equation of motion in operational space coordinates $\mathbf{p} = [x, y]^{\mathrm{T}}$. Because of the initially chosen independent set of relative coordinates $\mathbf{q} = [\theta_1, \theta_2]^{\mathrm{T}}$, there is no need for geometric constraints, and the transformation matrix $\mathbf{B}$ in (6.3) is simply the inverse of the manipulator Jacobian. Also, for input $\mathbf{u} = [\tau_1, \tau_2]^{\mathrm{T}}$, the control input matrix $\mathbf{H}$ is the identity matrix. Taking these into consideration, and assuming that only the shoulder motor with the higher loads will saturate, the components of the linearized equation of motion (6.4) are

$$\overline{\mathbf{M}} = \begin{bmatrix} \overline{m}_{11} & \overline{m}_{12} \\ \overline{m}_{21} & \overline{m}_{22} \end{bmatrix}, \ \mathbf{B} = \begin{bmatrix} b_{11} & b_{12} \\ b_{21} & b_{22} \end{bmatrix}, \ \ddot{\mathbf{p}} = \begin{bmatrix} \ddot{x} \\ \ddot{y} \end{bmatrix}, \ \mathbf{Q}_{\mathrm{sat}} = \begin{bmatrix} \tau_{1\max} \\ 0 \end{bmatrix}, \ \mathbf{H}_{\mathrm{sat}} = \begin{bmatrix} 0 \\ 1 \end{bmatrix} \text{ and } \ \mathbf{u}_{\mathrm{sat}} = \tau_2\,, \tag{6.8}$$

where, for the sake of brevity, the elements of $\overline{\mathbf{M}}$ and $\mathbf{B}$ are only indicated by single symbols. In addition, the circular trajectory shown in Fig. 6.3 is defined by the servo-constraints

$$\boldsymbol{\gamma}(\mathbf{p}(\mathbf{q}), t) = \begin{bmatrix} l_1 \cos(\theta_1) + l_2 \cos(\theta_1 + \theta_2) \\ l_1 \sin(\theta_1) + l_2 \sin(\theta_1 + \theta_2) \end{bmatrix} - \begin{bmatrix} x_D(t) \\ y_D(t) \end{bmatrix}, \tag{6.9}$$

where $x_D(t)$ and $y_D(t)$ define the desired motion of the end-effector of the manipulator. Note, that in the acceleration level equation (2.17) matrix $\boldsymbol{\Gamma} = \partial \mathbf{p}/\partial \mathbf{q}$ is precisely the manipulator Jacobian. It can be also seen that, during saturation, only the remaining single actuator, τ_2, can be used to realize both servo-constraints.

By having a planar motions specification, one can either consider γ_1 or γ_2 as the only elements of two different *reduced sets* of servo-constraints. According to (6.3), these different sets can be

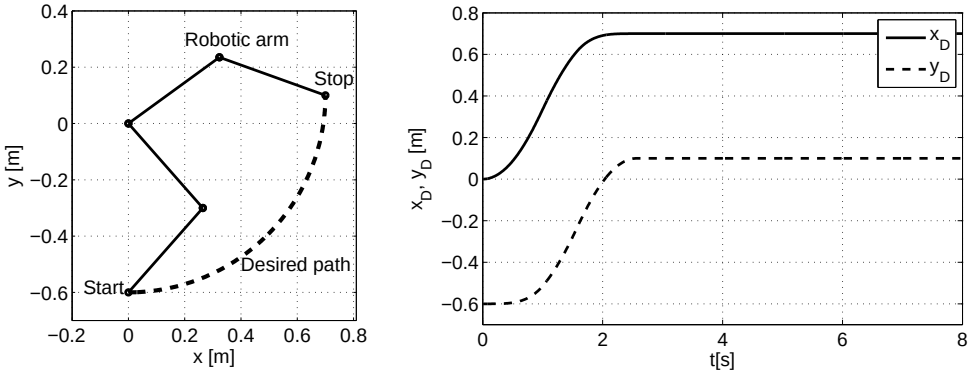

FIGURE 6.3. Desired path (left) and end-effector trajectories (right)

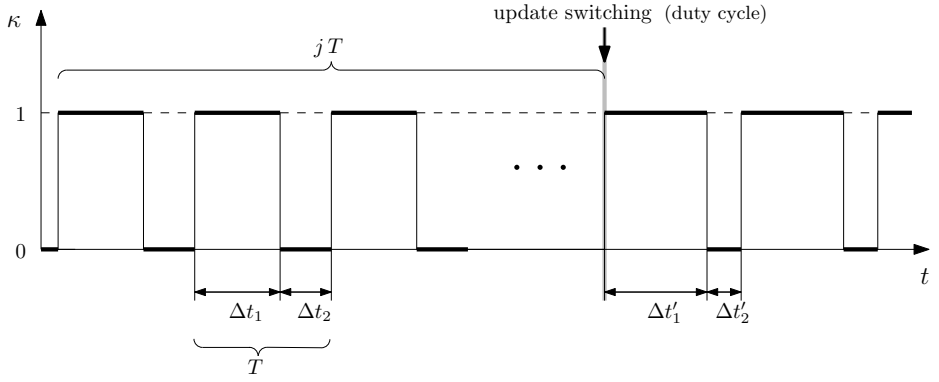

FIGURE 6.4. Switching function for periodic servo-constraint realization

combined in a single expression as

$$\gamma_{\text{sat}} = \kappa(t)\,\widehat{\gamma}_1 + (1-\kappa(t))\,\widehat{\gamma}_2 \tag{6.10}$$

where now $\widehat{\gamma}_i \equiv \gamma_i,\ i = 1{,}2$ and $\kappa(t) = \kappa(t{+}T)$ controls the switching between these servo-constraints. While in the previous chapter the pattern of the periodic switching was not changed during the operation (see Fig. 5.1), here it is updated based on the actual state of the system. This is illustrated in Fig. 6.4 where the update parameter, j, and the time period, T, are free control parameters which need to be tuned. The tuning of these parameters can be done by stability investigations in the different configurations or by simulations or these can be selected empirically. For a certain time period T, the switching between the control objectives represented by each reduced set of servo-constraints can then be determined based on equation (6.7). For the two-link manipulator example, this equation gives the duty cycle parameters, Δt_1 and $\Delta t_2 = T - \Delta t_1$, as follows

$$\Delta t_i = \frac{z_i T}{z_1 + z_2},\ i = 1{,}2 \quad \text{with} \quad z_1 = \frac{b_{21}^2 + b_{22}^2}{|\, b_{21}\overline{m}_{11} + b_2 2\overline{m}_{21}\,|} \quad \text{and} \quad z_2 = \frac{b_{21}^2 + b_{22}^2}{|\, b_{21}\overline{m}_{12} + b_{22}\overline{m}_{22}\,|}\,, \tag{6.11}$$

where $z_i = \left(\mathbf{e}_i^{\mathrm{T}} \boldsymbol{\mathcal{M}}\, \mathbf{e}_i\right)^{-1/2}$, and unit vectors $\mathbf{e}_1 = [1,0]^{\mathrm{T}}$ and $\mathbf{e}_2 = [0,1]^{\mathrm{T}}$ represent the different *servo-constraint directions*. When there is no actuator saturation, the required control input can be determined based on equations (2.20) and (6.9). During saturation, equations (6.2) has to be considered with the terms defined in equations (6.8) and (6.9), and using the periodic servo-constraints given by equations (6.10) and (6.11).

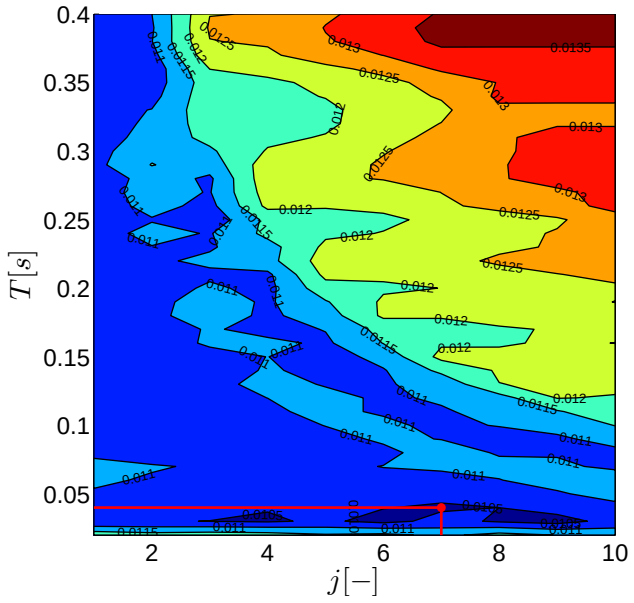

FIGURE 6.5. Average trajectory following error with different control parameters

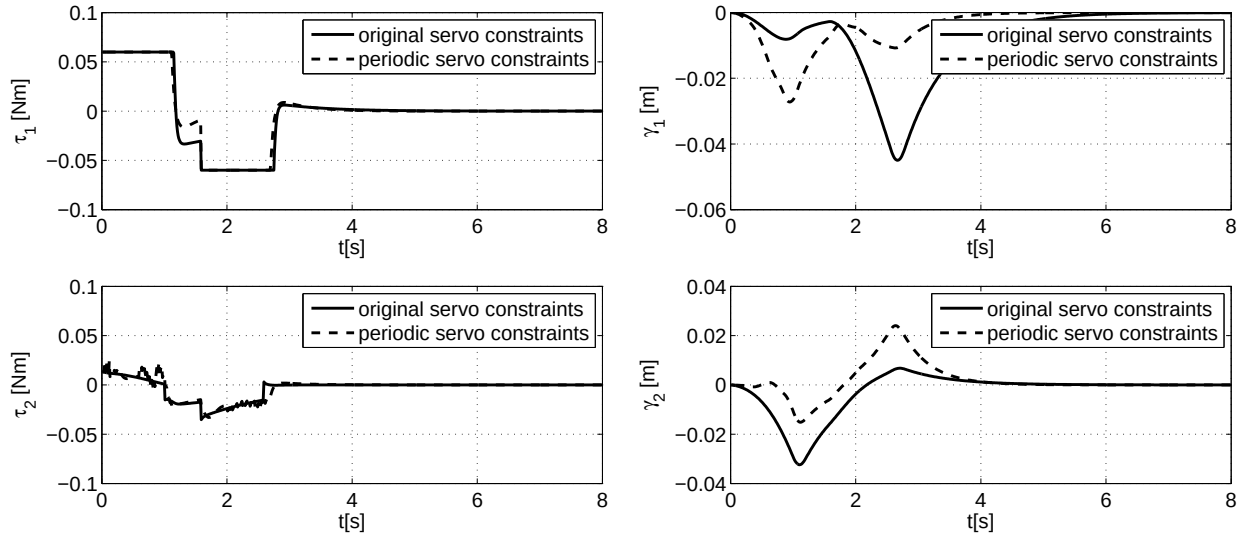

FIGURE 6.6. Actuator efforts (left) and servo-constraint violations (right)

For tuning the periodic controller, a possible procedure is to simulate the system with different j and T pairs, and use the RMS (see Eq. (5.6)) value of the trajectory following error to assess the control performance. For the trajectory considered (see Fig. 6.3), this results in the contour plot shown in Fig. 6.5. It can be seen that the pair $j = 7$ and $T = 0.04\,\mathrm{s}$ can provide a good tracking performance, where the chosen larger value of parameter j is for reducing the computational efforts. Also, the trajectory following error is bounded everywhere in the investigated domain of control parameters and therefore the system is stable in this domain.

Simulation results obtained with the selected parameters are compared to those of the classical computed torque control in Fig. 6.6. It can be seen that both methods have simultaneous, but different magnitude peaks in the constraint violations. The periodic controller seems to outperform the other in the second half of the simulation, and the system recovers from the saturation slightly

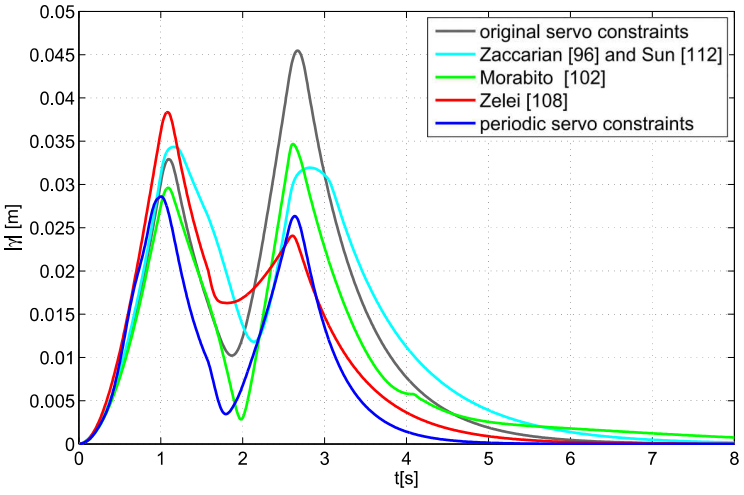

FIGURE 6.7. Norm of servo-constraint violations for different methods with $a_{max} = 1\,m/s^2$

TABLE 6.1. Peak and average trajectory tracking errors ($a_{max} = 1\,m/s^2$)

Control method	$\max \gamma$ $[m]$	$\overline{\text{RMS}}$ $[m]$
Original servo-constraints	0.046	0.0164
Zaccarian [96] and Sun [112]	0.033	0.0158
Morabito [102]	0.034	0.0130
Zelei [108]	0.038	0.0134
Periodic servo-constraints	0.031	0.0105

faster when periodic servo-constraints are applied (see τ_1 in Fig. 6.6). When the Euclidean norm of the servo-constraint violation is considered, the better performance of the periodic controller is obvious. This is shown in Fig. 6.7 and in Tab. 6.1, where the results obtained with three other methods are also compared.

The method proposed in our previous work [108] is similar to this method in the sense that when saturation happens a reduced set of servo-constraint is constructed, which is then used until the system recovers from saturation. The main difference between that and the proposed approach is the periodic variation of different reduced sets of servo-constraint as opposed to using only one. Also, in the present work I propose an algorithmic approach to select to which extent the different sets of servo-constraints, representing different control objectives, are considered in the periodic control signal. In Fig. 6.7 it is shown that the two methods perform similarly in the beginning and at the end of the simulated motion, but the use of periodic servo-constraints could considerably reduce the trajectory tracking error in the middle. This is the part of the trajectory which changes the most (see Fig. 6.3). We also note that the results are directly comparable as the method in [108] does not require any additional control parameters to be defined.

As a second method to compare with, let us consider a specific anti-windup control scheme presented in [102]. Among the many general purpose anti-windup schemes, this one is specifically developed for Euler-Lagrange systems. It is well suited for robotic mechanical systems, which makes

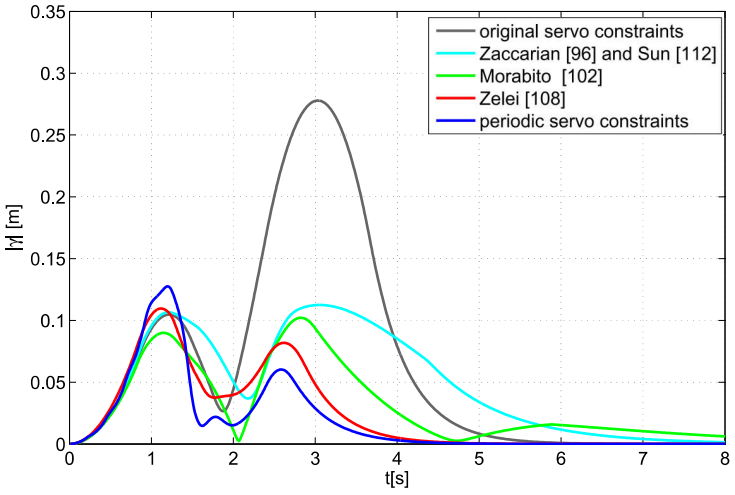

FIGURE 6.8. Norm of servo-constraint violations for different methods with $a_{max} = 1.2\,m/s^2$

the comparison clearer. For the implementation of the method, in the present example, three additional control parameters had to be chosen. By keeping the notations of the referenced paper, these anti-windup design parameters are $K_g = 0.99$, $K_q = 10$ and $K_0 = 1$. Parameter K_g is selected to the same value used in [102] in a similar example, while the PD type control gains K_q and K_0 were tuned empirically to achieve the smallest trajectory tracking error. This method and the use of periodic servo-constraints result in similar trajectory following errors almost in the entire course of the motion, but the periodic controller shows a much better convergence to the desired zero steady state error.

The third and last comparison was made with a classical anti-windup control scheme [96] by following the implementation used in reference [112]. The method is exclusive to single-input single-output systems, and therefore it was only applied to the saturating actuator (shoulder motor) of the robot by using joint space position control during saturation. The anti-windup control gains were empirically selected as $k_{01} = 0.6$ and $k_l = 10$, where the original notations used in [112] are kept. When there was no saturation, the servo-constraint based computed torque controller (2.20) was used. In summary, this classical approach could also reduce the effect of actuator saturation, but it turned out to be less efficient that the other methods in the considered benchmark example.

When the tracking error of the four different methods are compared, Fig. 6.7 suggests that the best results can be achieved with the method of periodic servo-constraints. This is confirmed by the RMS values presented in Tab. 6.1. The RMS value is accepted as a characteristic measure in other works [113] as well. It is clearly shown that the methods in [96], [102] and [108] have a similar overall performance, while the method of periodic-servo constraints gives both the lowest peak- and average tracking errors. With respect to the use of the original servo-constraints, the average tracking error is improved by 36%, and the improvement compared to the other controllers is about 20% (see Table 6.1). The differences between the methods are revealed better when a higher acceleration $a_{\max} = 1.2m/s^2$ is set for the desired trajectory. The corresponding results are summarized in Fig. 6.8 and in Tab. 6.2. The proposed switched periodic controller outperforms the others almost everywhere except at the beginning of the motion, and it has the best performance in terms of the average tracking error (see Tab. 6.2). It is also important to note that for the higher

TABLE 6.2. Peak and average trajectory tracking errors with $a_{max} = 1.2\,m/s^2$

Control method	$\max \gamma$ $[m]$	$\overline{\text{RMS}}$ $[m]$
Original servo-constraints	0.27	0.1083
Zaccarian [96] and Sun [112]	0.120	0.0633
Morabito [102]	0.105	0.0445
Zelei [108]	0.110	0.0401
Periodic servo-constraints	0.130	0.0364

acceleration trajectory the same periodic control parameters ($j = 7$ and $T = 0.04\,\text{s}$) were used as before. This can explain the initially larger errors, and also show the robustness of the method with respect to changing the desired trajectory.

6.3 New results

Driving torque saturation is an undesired event in trajectory tracking control of mechanical systems, which makes the controlled system temporarily underactuated. To reduce the undesired dynamic effects due to this underactuation, a period motion controller was proposed. For the algorithmic tuning of the controller a new manipulability type performance measure was introduced. A detailed comparison with other techniques was carried out in case of a planar robot application. The proposed controller is described in the next thesis.

Thesis 4.

The proposed control concept for driving torque saturation in trajectory tracking control is detailed in the followings. Until saturation occurs the classical computed torque controller is applied. During saturation, the number of servo-constraints is appropriately reduced, different sets of servo-constraints are formed, and combined into a new periodic servo-constraint signal $\boldsymbol{\gamma}_{\mathrm{sat}}(t)$. The periodic servo-constraint signal is formed as

$$\boldsymbol{\gamma}_{\mathrm{sat}} = \sum_{i=1}^{N} \kappa_i \, \widehat{\boldsymbol{\gamma}}_i \quad \textbf{with} \quad \kappa_i(t) = \kappa_i(t+T),$$

where $\kappa_i(t)$ controls the switching between the different sets of servo-constraints, and $N < \binom{l}{r}$ is the number of the considered different sets, $\widehat{\boldsymbol{\gamma}}_i$, which are subsets of the original control objectives, $\widehat{\boldsymbol{\gamma}}$. The algorithmic selection of a suitable periodic control signal is based on the introduced performance measure, which rates the different servo-constraint sets, $\widehat{\boldsymbol{\gamma}}_i$, based on their effects and importance.

Compared to different classical methods taken from the literature the average tracking error is improved by at least 20%. The maximum trajectory following error is decreased by 7% compared to the best performing classical method investigated.

Related journal publications:

[1] L. Bencsik and L.L. Kovács, "Reduction of the effect of actuator saturation with periodic servo-constraints," *Proceedings of the Institution of Mechanical Engineers, Part C: Journal of Mechanical Engineering Science*, 2016, published online in October 20, 2016, 10 pages.

[2] A. Zelei, L. Bencsik, and G. Stépán, "Handling actuator saturation as underactuation: Case study with acroboter service robot," *Journal of Computational and Nonlinear Dynamics*, vol. 12, no. 3, 2017.

Other related publication: [115]

Chapter 7

Constrained motion analysis of human running

The mechanical analysis of running requires algorithmic tools due to the continuous change of topology. That is the reason why the constrained based techniques of multibody systems are useful tools in the analysis of running or walking. The human leg has a sophisticated muscular structure [116] and it contains much higher number of muscles than its degrees of freedom [117]. At the same time, human walking and running motion is partially passive, underactuated.

In order to discover this matter, many researchers study the behaviour and dynamical characteristics of passive [118] or partially passive [119] walkers which are typically underactuated devices. Energy efficiency of underactuated walker devices are obviously better than that of the fully actuated and controlled robots. Energy efficiency is important in general. Therefore the source of energy losses needs to be investigated. In case of normal circumstances, the dissipation effect of aerodynamical forces and other damping forces can be neglected. The main energy dissipation mechanism is related to how the foot strikes the ground. This is why energy efficient running requires years of training which changes the running gait in a way that the momentum of the runner is better preserved in the horizontal direction.

Many studies like [120] and [121] help to understand bipedal locomotion, human walking and running. Several approaches have been developed which try to realize the healthy, injury preventing, energy efficient and natural way of running in practice [122–124].

Many biomechanical models [125], [126] of different complexity are used to understand the dynamics of human running, including impact dynamics. Here the goal is to introduce a minimally complex biomechanical model which can characterize the dynamic effects of foot strike pattern and shank angle at foot touchdown.

7.1 Minimally complex mechanical model

The *foot strike pattern* and the dynamical and kinematical differences between barefoot and shod running were discussed in [127]. The related experimental results were interpreted from a mechanical point of view by [125]. A low DoF model was introduced for investigating the effect of foot strike pattern on impact intensity. The impact intensity is related to the magnitude of the reaction forces due to foot-touchdown. Foot strike pattern is described by the dimensionless parameter s called *strike index* which interprets the centre of pressure of the ground foot contact for the planar model [128].

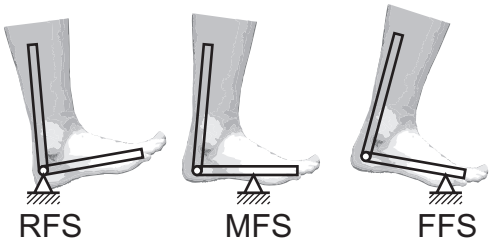

FIGURE 7.1. Strike patterns: rearfoot (RFS), midfoot (MFS) and forefoot (FFS) strike

Based on the initial contact the strike patterns are sorted into rearfoot/heel (RFS, $s = 0 \dots 0.33$), midfoot (MFS, $s = 0.33 \dots 0.66$) or forefoot (FFS, $s = 0.66 \dots 1$) strike as the simplified interpretation shows in Fig. 7.1.

Fig. 7.2a shows a planar model with horizontal foot and vertical shank. The ground contact location (point O) is defined by s respect to the ankle. Stiff and compliant ankle joints (point B) were considered. The pre-impact velocity was considered vertical. The authors drew the conclusion that forefoot landing provides lower impact intensity.

An extended analysis of the same mechanical model was carried out and a more algorithmic mechanical approach was applied in [126]. As Fig. 7.2b shows, this model still contains the foot and the shank, but the foot and shank angles (α and β) are new parameters. The calculations were based on the consideration that ground contact is represented by geometric constraints. The kinetic energy content associated with the constrained motion, which serves as an indicator of foot impact intensity, was calculated. The authors confirmed the results of [125] and arrived to the conclusion that the shank angle β, which is responsible for foot positioning, does not affect the impact intensity in case of FFS and has limited effect for the case of RFS.

The model shown in Fig 7.2b is still not detailed enough to be able fully describe all the important characteristics of the different running styles. Some experimental observations cannot be explained by the model in Fig. 7.2. For example the effect of shank angle can not be investigated.

Reference [125] states that in case of RFS, ankle compliance has little effect and there is some contribution from mass above the knee, which also encourages us to investigate an extended model which is not limited to shank, foot and stiff ankle only. Considering a compliant ankle can be important as the foot and the shank are connected by muscles and tendons which are flexible. On the other hand the forces exerted by flexible components are typically neglected during impact [126].

The proposed model shown in Fig. 7.2.c consists of 3 segments: thigh, shank and foot joined by ideal, frictionless joints. An additional pointmass m_b is attached representing the mass of the trunk and the other not-modelled body parts, like head, arms and other leg. Inertial and geometric data are collected in Table 7.1 and were adopted from [129–131]. The data correspond to an average 24 years old male person with 73 kg bodyweight and 173 cm height. Segmental centre of gravity (CoG) locations are measured from proximal end of each segment. The moment of inertia around CoG axis of each segment is estimated by assuming a homogeneous rod model.

7.2 Impact characterisation

A feature of legged locomotion systems is the changing topology. For instance, when ground and foot get in contact, new constraints arise and the model will have less DoFs than in the airborne phase of

TABLE 7.1. Inertial and geometric data of body segments

	mass kg	moment of inertia kg m^2	length m	CoG m
trunk	$m_b = 58.5$	-	-	-
thigh	$m_t = 10.3$	$J_t = 139\,10^{-3}$	$l_t = 0.402$	$d_t = 0.164$
shank	$m_s = 3.16$	$J_s = 48.2\,10^{-3}$	$l_s = 0.428$	$d_s = 0.188$
foot	$m_f = 1.00$	$J_f = 0.456\,10^{-3}$	$l_f = 0.274$	$d_f = 0.032$

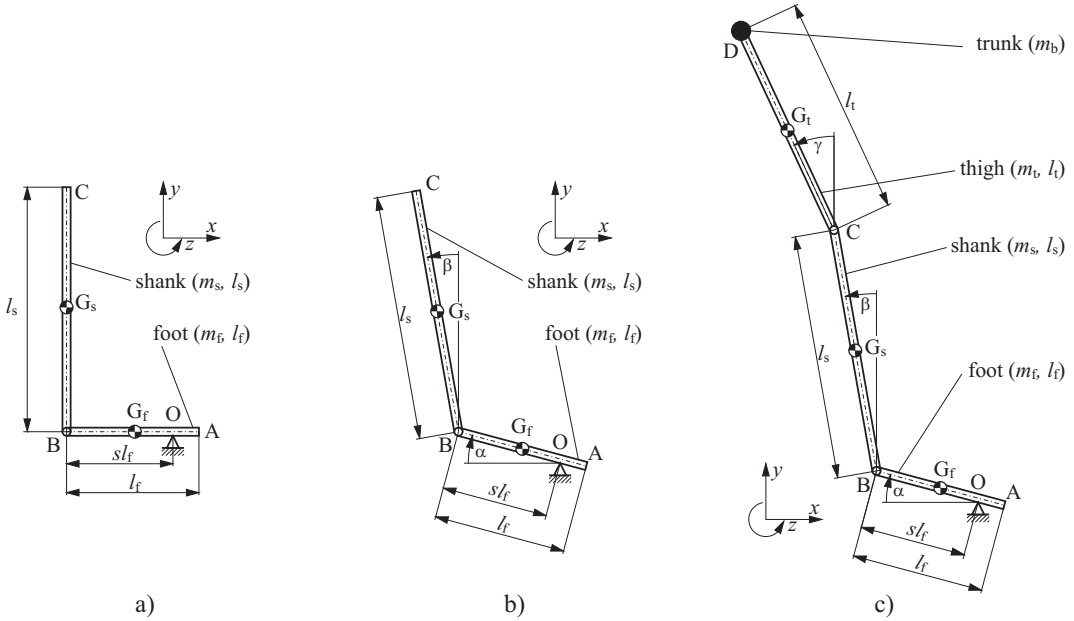

FIGURE 7.2. Single rigid body (a), jointed shank-foot (b) the proposed minimally complex model (c)

running. Besides, foot impact with the ground is also an important phenomenon. We apply a constraint based approach [132] and [126] for handling both challenges. This approach has advantages over the method of angular momentum conservation, which is usually applied when bipedal locomotion systems [125] and passive dynamic walking mechanisms [118, 133–135] are analysed. The main strength of the geometric constraint based approach is the applicability for closed kinematic loops (e.g. walking, when both legs touch the ground for finite time), which is not true for the approach using conservation of the angular momentum [136, 137].

In the presented approach the finite (continuous) dynamics and the discrete collision event (impulsive dynamics) are distinguished in the mechanical description of legged locomotion. It is assumed that the ground-foot collision is instantaneous, which leads to infinitely large instantaneous forces over an infinitesimal time duration so that the net impulse due to the impact force is finite [125, 126, 136, 137]. Completely inelastic collision is also assumed, so that there is no rebound [125, 126]. Considering a normal running, it is assumed that there is no slip of the foot. Between the impacts the dynamics can be described by the classical tools of multibody dynamics as Eq.(1.5). Rewriting Eq. (1.5) the impulsive dynamics can be written in the following form [126] [138]:

$$\mathbf{M}(\dot{\mathbf{q}}^{+} - \dot{\mathbf{q}}^{-}) = \mathbf{I}_{\mathrm{F}}, \tag{7.1}$$

where $\dot{\mathbf{q}}^- = \dot{\mathbf{q}}(t_i^-)$ and $\dot{\mathbf{q}}^+ = \dot{\mathbf{q}}(t_i^+)$ are the generalized velocities right before and after the foot-ground collision, respectively. $\mathbf{I}_\mathrm{F}$ is the net impulse of those constraint forces which cause the sudden topology change, all other active and constraint forces are finite, thus the impulse of those are neglected. If the mass matrix $\mathbf{M}$ is invertible the post-impact generalized velocity vector $\dot{\mathbf{q}}^+$ can be expressed from Eq. (7.1).

In the followings, the focus is on the impulsive event associated with the ground-foot impact.

The ground-foot contact is considered as an instantly arising geometric constraint (1.3) as

$$\boldsymbol{\varphi}(\mathbf{q}) = \begin{bmatrix} \varphi_{tan} \\ \varphi_{norm} \end{bmatrix} = \begin{bmatrix} x_O \\ y_O \end{bmatrix} = \mathbf{0}, \tag{7.2}$$

that expresses the anchoring of point O. For satisfying the no-slip condition the Coulomb friction coefficient must be larger than the critical value [139]:

$$\mu_c = \left| \frac{\boldsymbol{\Phi}_{norm}\mathbf{M}^{-1}\boldsymbol{\Phi}_{tan}^\mathrm{T}}{\boldsymbol{\Phi}_{norm}\mathbf{M}^{-1}\boldsymbol{\Phi}_{norm}^\mathrm{T}} \right|, \tag{7.3}$$

where $\boldsymbol{\Phi}_{tan}$ and $\boldsymbol{\Phi}_{norm}$ are the Jacobians of the tangential and normal direction constraints respectively.

The velocity fields on the impacting bodies change instantaneously, and the change in the configuration is neglected. This is because of the sudden change in topology, which is described by the constraint $\boldsymbol{\varphi}(\mathbf{q}) = \mathbf{0}$ in the model, thus the post-impact velocity have to be admissible by the contact constraint. The separation of admissible and constrained motion spaces was already introduced in Sec. 1.2.3 in detail. Assuming perfectly inelastic collision and based on the expression described in Eq. (1.16) the post impact velocity can be described as

$$\dot{\mathbf{q}}^+ = \mathbf{P}_a\dot{\mathbf{q}}^-, \tag{7.4}$$

where matrix $\mathbf{P}_a$ projects into the space of admissible motion (See: Eq. (1.16)). Substituting the expression (7.4) into (7.1) gives

$$\mathbf{M}(\mathbf{I} - \mathbf{P}_a)\,\dot{\mathbf{q}}^- = \mathbf{I}_\mathrm{F}. \tag{7.5}$$

Using the relation between the admissible and constraint motion space ($\mathbf{P}_c = \mathbf{I} - \mathbf{P}_a$) the following relation can be deduced

$$\mathbf{M}\mathbf{P}_c\,\dot{\mathbf{q}}^- = \mathbf{I}_\mathrm{F}, \tag{7.6}$$

where $\mathbf{P}_c\,\dot{\mathbf{q}}^-$ is the generalized velocity which vanishes due to the perfectly inelastic collision considered.

From the energetic point of view, running can be characterized with the portion of kinetic energy which will be completely dissipated during impact [139]

$$T_c = \frac{1}{2}(\dot{\mathbf{q}}^-)^\mathrm{T}\mathbf{P}_c^\mathrm{T}\mathbf{M}\mathbf{P}_c\dot{\mathbf{q}}^-. \tag{7.7}$$

The quantity T_c is called *constrained motion space kinetic energy* (CMSKE). Considering the related literature [126], [132] as a performance measure the strike intensity can be characteried by the CMSKE.

7.3 Numerical studies

The proposed 5 DoF model is described by the Cartesian coordinates of point A, β and γ are measured relative to the vertical direction and α is measured relative to the horizontal direction

$$\mathbf{q} = \left[\, x_{\mathrm{A}}, \, y_{\mathrm{A}}, \, \alpha, \, \beta, \, \gamma \, \right]^{\mathrm{T}}. \tag{7.8}$$

The mass matrix, appearing in equation (7.7), is shown below. For the sake of brevity the new symbols $m_0 = m_b + m_t + m_s + m_f$, $m_{bts} = m_b + m_t + m_s$ and $m_{bt} = m_b + m_t$ were used. Furthermore, shorthand notation are used as $s_x = \sin x$ and $c_x = \cos x$. It is also introduced that $s^+_{\alpha\gamma} = \sin(\alpha+\gamma)$, $s^+_{\alpha\beta} = \sin(\alpha+\beta)$ and $c^-_{\beta\gamma} = \cos(\beta-\gamma)$.

$$\mathbf{M} = \begin{bmatrix} \mathbf{M}_{11} & \mathbf{M}_{12} \\ \mathbf{M}_{21} & \mathbf{M}_{22} \end{bmatrix}, \tag{7.9}$$

where the sub-matrices are the followings

$$\mathbf{M}_{11} = \begin{bmatrix} m_0 & 0 \\ 0 & m_0 \end{bmatrix},$$

$$\mathbf{M}_{12} = \begin{bmatrix} (l_f m_0 - d_f m_f)s_\alpha & (d_s m_s - l_s m_{bts})c_\beta & (d_t m_t - l_t m_{bt})c_\gamma \\ (l_f m_0 - d_f m_f)c_\alpha & (d_s m_s - l_s m_{bts})s_\beta & (d_t m_t - l_t m_{bt})s_\gamma \end{bmatrix},$$

$$\mathbf{M}_{21} = \begin{bmatrix} (l_f m_0 - d_f m_f)s_\alpha & (l_f m_0 - d_f m_f)c_\alpha \\ (d_s m_s - l_s m_{bts})c_\beta & (d_s m_s - l_s m_{bts})s_\beta \\ (d_t m_t - l_t m_{bt})c_\gamma & (d_t m_t - l_t m_{bt})s_\gamma \end{bmatrix},$$

$$\mathbf{M}_{22} = \begin{bmatrix} J_f^2 + l_f^2 m_0 - (2l_f d_f - d_f^2)m_f & l_f(d_s m_s - l_s m_{bts})s^+_{\alpha\beta} & l_f(d_t m_t - l_t m_{bt})s^+_{\alpha\gamma} \\ l_f(d_s m_s - l_s m_{bts})s^+_{\alpha\beta} & J_s^2 + l_s^2 m_{bts} - (2l_s d_s - d_s^2)m_s & l_s(l_t m_{bt} - d_t m_t)c^-_{\beta\gamma} \\ l_f(d_t m_t - l_t m_{bt})s^+_{\alpha\gamma} & l_s(l_t m_{bt} - d_t m_t)c^-_{\beta\gamma} & J_t^2 + l_t^2 m_{bt} - (2l_t d_t - d_t^2)m_t \end{bmatrix}. \tag{7.10}$$

When the foot is in contact with the ground the geometric constraint vector $\boldsymbol{\varphi}$ is

$$\boldsymbol{\varphi} = \begin{bmatrix} x_{\mathrm{A}} - (1-s)l_{\mathrm{f}}c_\alpha \\ y_{\mathrm{A}} + (1-s)l_{\mathrm{f}}s_\alpha \end{bmatrix}, \tag{7.11}$$

from which the following constraint Jacobian can be calculated as

$$\boldsymbol{\Phi} = \begin{bmatrix} 1 & 0 & (1-s)l_{\mathrm{f}}s_\alpha & 0 & 0 \\ 0 & 1 & (1-s)l_{\mathrm{f}}c_\alpha & 0 & 0 \end{bmatrix}. \tag{7.12}$$

Using these expressions and the formulation developed in Eqs.(7.5)-(7.7), the constraint motion space analysis of different foot strikes can be carried out. Three main cases will be considered. First, some results available in the literature will be reproduced with the proposed model. Then two more accurate models will be analyzed in order to find a model which is able to characterize different running styles.

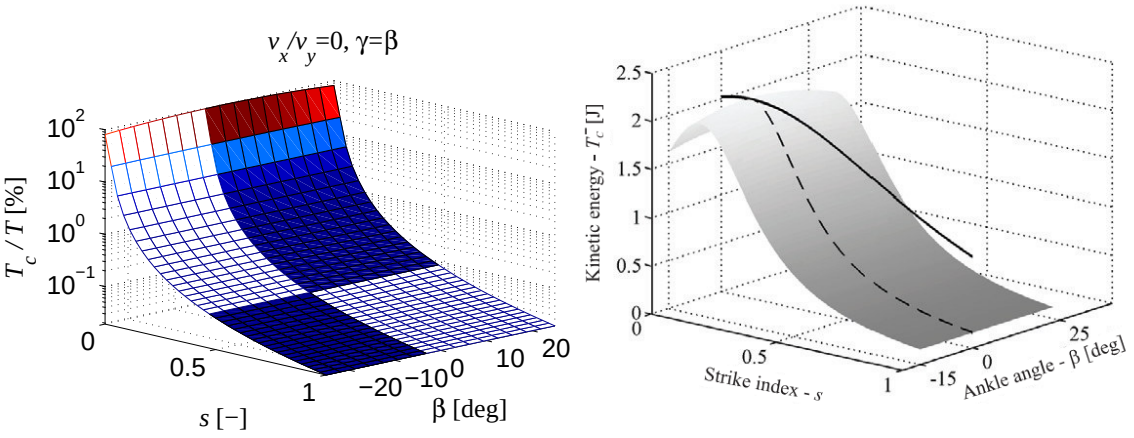

(A) CMSKE in case of the proposed model (B) Result of the corresponding literature [126]

FIGURE 7.3. CMSKE in case of straight leg and vertical pre-impact velocity

Straight leg, vertical pre-impact velocity

Fig. 7.3a shows the calculated CMSKE assuming straight leg and vertical impact velocity. The presented result corresponds to model (c) in Fig. 7.2 with parameters $\alpha = 0$ (horizontal foot), $\beta = \gamma$ (straight leg) and pre-impact velocities $\dot{x}_A = 0\text{m/s}$, and $\dot{y}_A = -1\text{m/s}$. In Fig. 7.3a the CMSKE is normalized with respect to the pre-impact kinetic energy. For the sake of better visibility, logarithmic scale is used in T_c/T axis. The calculations confirm that shank angle β can have a small effect on the impact intensity at low strike index: the scaled impact intensity (T_c/T) is 98% at $\beta = 0$ and 92% at $\beta = 15°$. Furthermore, the impact intensity is a symmetric function of β, which does not fully agree with practical evidences [140], [141]. The positive β value corresponds to overstriding which is a not preferred running form. Fig. 7.3a also confirms that larger strike index s provides smaller impact and higher energy efficiency (the ratio of T_c and T is 0.25% at $s = 1$).

The results qualitatively agree with result of the literature [126] (see Fig. 7.3b). The differences between the two surfaces are caused by the difference of the applied parameters and in case of the Fig. 7.3a the relative value of the CMSKE is proposed.

The practical experiences [122–124] encouraged us to accomplish the following two test cases that are expected to show that the shank angle β has a more important effect on the impact intensity.

Bended knee, vertical pre-impact velocity

In the second study, the angles of the thigh and the foot were set to $\gamma = 15°$ and $\alpha = 0°$ respectively, while the shank angle β was varied in the range of $-15°$ to $15°$. The CMSKE is depicted in Fig. 7.4. The results are contradictory with [126], because β does have a significant effect on T_c. The worst case is rearfoot strike combined with extended knee ($\beta = \gamma$), when almost 100% of the kinetic energy is absorbed by the impact. Overstriding (positive values of β) causes large energy loss and high impact, as it is expected based on practical observations [140]. Because of involving thigh and point mass m_b in the model, the results became much more sensitive to the varied parameters. The results show that overstriding can have energy absorbing effect.

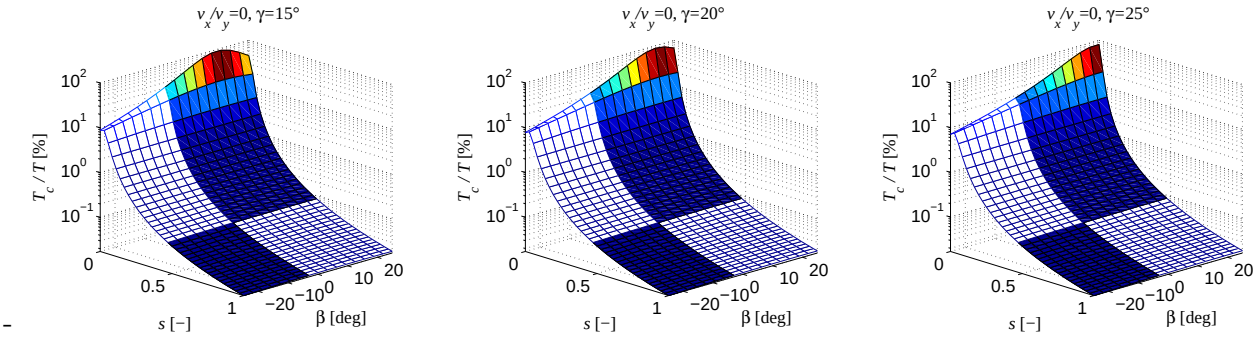

FIGURE 7.4. CMSKE (T_c) as function of strike index (s) and shank angle (β) in case of bended knee and vertical pre-impact velocity

Bended knee, vertical and horizontal pre-impact velocity

In the third study the effect of the horizontal component of the pre-impact velocity is investigated. In the second, previous study it was neglected for the sake of simplicity, but it can have an important effect on the impact intensity. In the horizontal direction three different speed values were considered for point A as $\dot{x}_A = 3\text{m/s}$, $\dot{x}_A = 4\text{m/s}$ $\dot{x}_A = 5\text{m/s}$. The vertical speed $\dot{y}_A = -1\text{m/s}$ is the same as before. The consideration of more realistic pre-impact velocity condition was also encouraged by reference [142] which concludes that the foot placement and velocity is prepared well before touchdown. Fig. 7.5 suggests that the effect of angle β becomes more important as the horizontal velocity component increases. Although only 28% of kinetic energy is lost in maximum. It is because the horizontal speed component of the body does not change too much.

The constrained motion space kinetic energy is minimal, when the strike index is large and the shank angle β is close to zero. In the best situation 2% of the pre-impact kinetic energy is absorbed only. The results of Fig. 7.5 change significantly comparing to Fig. 7.4 and Fig. 7.3a, because the horizontal velocity components cannot be highly influenced by the ground force which acts in vertical direction.

7.4 Concluding remarks

It is known from experience that overstride and RFS is in relation with each other. Usually overstriding impels RFS, and it is natural that FFS occurs if the landing point is nearly below the CoG of the body. Therefore the practically relevant regions are highlighted in Figs 7.3a, 7.4, 7.5. The results indicate that landing below CoG ($\beta < 0$) together with forefoot landing ($s > 0.5$) is preferable, while overstriding ($\beta > 0$) together with RFS ($s < 0.5$) is better to be avoided, from the viewpoint of impact intensity and impact induced kinetic energy loss.

Fig. 7.6 (published in [143]) illustrates the evidence how important the shank angle is. When running downhill, one tries to keep the speed low. The breaking technique is basically the overstriding, because it results in the largest energy absorption. In contrast, a long distance road race runner, whose aim is to save energy, keeps his/her shank in negative angle before foot impact (see Fig. 7.6 right). The results correspond to this practical knowledge.

The Tc/T ratio difference at $\beta = 0°$ and $\beta = \pm 15°$ was 6% only when bended knee and horizontal velocity was not considered (see Fig. 7.3a). Contrarily, in the extended model and the consideration of horizontal velocity component resulted in 26% difference in the kinetic energy ratio when overstriding compared to not overstriding as Fig. 7.5 shows.

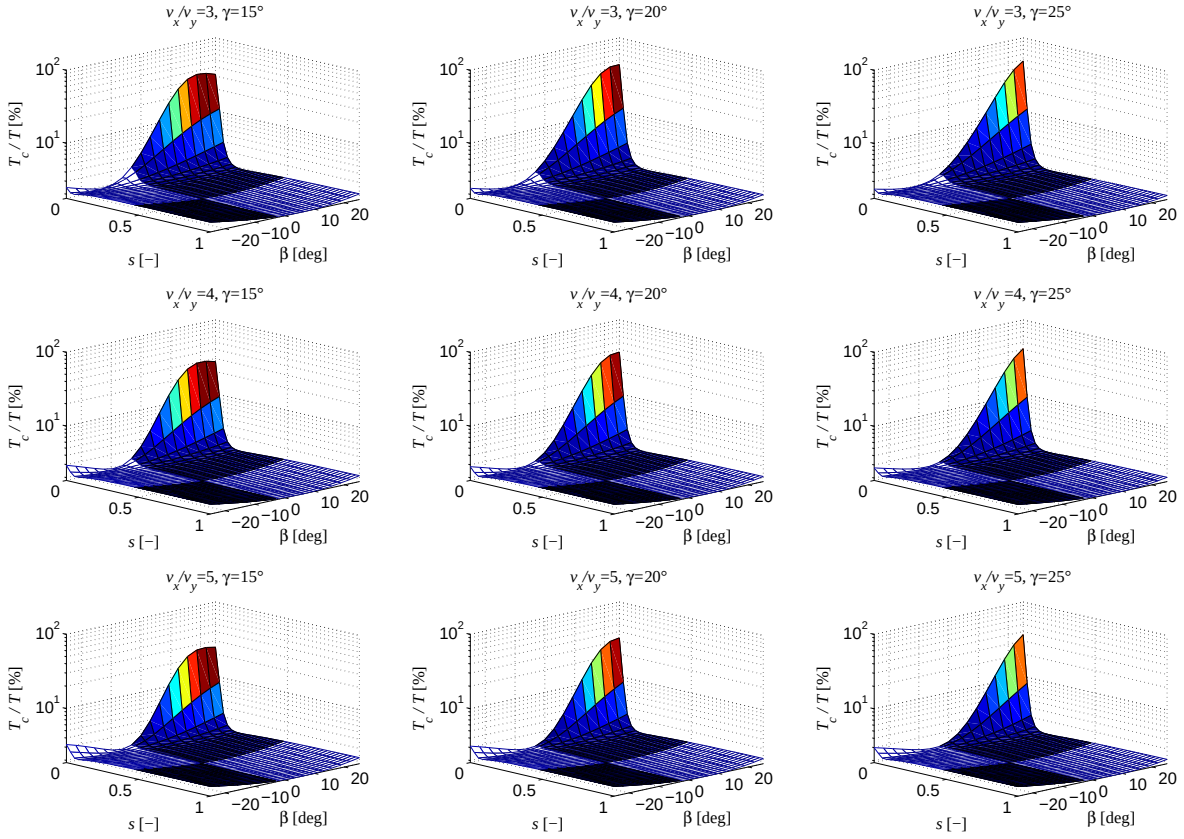

FIGURE 7.5. CMSKE as function of strike index and shank angle using the bended knee model horizontal and vertical pre-impact velocity components

It is showed that more precise results can be obtained, if the foot-shank model is extended with the thigh and the inertia of the other body parts. Also the consideration of horizontal velocity component of the body leads to more realistic results. The results also show that the shank angle is at least as important parameter as the strike pattern. However, the practical meaning of this statement is in total correspondence with the referred literatures [125–127] because proper shank angle induces forefoot strike which was shown to be the best for barefoot running in [125].

Furthermore in contrast to [126] [125], the analysis revealed that shank angle highly affects the impact intensity. Forefoot strike implies lower impact intensity and energy absorption than rearfoot strike, which is in coincidence with the literature [144]. It was shown that the horizontal velocity cannot be neglected when foot impact is analyzed. Dynamical calculations provided information about the effect of strike pattern and foot positioning on the energy efficiency and impact intensity which can be used as a measure for the risk of injuries.

FIGURE 7.6. Different landing strategies are used when running downhill (left) or running on flat track (right) [143]

7.5 New results

The impact intensity in different running modes is characterized by the constrained motion space kinetic energy (CMSKE), which is absorbed by the ground-foot contact. Using the models recently proposed in the literature it is shown that lower ground-foot impact is generated when fore-foot strike occurs than in case of rear-foot strike. The corresponding CMSKE values are independent of the sign of the shank angles. This is in contrast with the specialist literature, where it was shown that landing with a positive shank angle, i.e., overstriding causes larger impacts. Here, an improved planar model was proposed for the analysis of different modes of running, which is a minimally complex representative that describes the phenomenon of overstriding, and the effect of rear- and fore-foot strikes at the same time.

Thesis 5.

The improved planar model contains the leg, the shank, the thigh and an additional pointmass representing the mass of the unmodelled body parts. With the proposed extended model, the proper effect of the shank angle can be captured because the absorbed kinetic energy (CMSKE) is larger in case of the positive shank angle than in case of the negative shank angle. The results confirm the physical observations. Furthermore, the proposed model shows that lower ground-foot impact is generated when fore-foot strike occurs than in case of rear-foot strike, which corresponds to the results obtained by the other models of the recent literature.

Related journal publication:

L. Bencsik and A. Zelei, "Effects of human running cadence and experimental validation of the bouncing ball model," *Mechanical Systems and Signal Processing*, vol. 89, pp. 78–87, 2016

Other related publications:

[136], [137], [145], [146]

Bibliography

[1] R. Seifried, *Dynamics of Underactuated Multibody Systems: Modeling, Control and Optimal Design*, Springer, 2014.

[2] R. Tedrake, "Underactuated robotics: Learning, planning, and control for efficient and agile machines," MIT lecture notes, 2009.

[3] J.-P. Merlet, *Parallel Robots*, Kluwer Academic Publishers, 2000.

[4] KUKA official homepage, "www.kuka-robotics.com," last accessed: March. 2017.

[5] L. Birglen, T. Laliberté, and C. C. Gosselin, *Underactuated Robotic Hands*, Springer, 2008.

[6] E. H Moore, "An innovative robotic gripper for grasping and handling research," *IEEE Journal of Robotics and Automation*, vol. 2, pp. 975–979, 1991.

[7] A. Zelei, *Computed Torque Control and Utilization of Parametric Excitation for Underactuated Dynamical Systems*, Ph.D. thesis, Budapest University of Technology and Economics, 2015.

[8] A. Choukchou-Braham, C. B. Braham, M. Djemai, and K. Busawon, *Analysis and Control of Underactuated Mechanical Systems*, Springer, 2013.

[9] Balanceboard official homepage, "http://balanceboard.co.uk/," last accessed: March. 2017.

[10] Jetovator official homepage, "www.jetovator.com," last accessed: March. 2017.

[11] W. Singhose, W. Seering, and N. Singer, "Residual vibration reduction using vector diagrams to generate shaped inputs," *Journal of Mechanical Design*, vol. 116, no. 2, pp. 654–659, 1994.

[12] G. Stépán and et al., "A ceiling based crawling, hoisting and swinging service robot platform," in *Proceedings of Beyond Gray Droids: Domestic Robot Design for the 21st Century Workshop at HCI 2009*, 2009.

[13] B. Siciliano and O. Khatib (eds.), *Handbook of Robotics*, Springer, 2008.

[14] J. G. de Jalón and E. Bayo, *Kinematic and dynamic simulation of multibody systems: the real-time challenge*, Springer-Verlag, 1994.

[15] V. I. Kirgetov, "The motion of controlled mechanical systems with prescribed constraints (servo constraints)," *Prikl. Mat. Mekh.*, vol. 31, no. 3, pp. 433–447, 1967.

[16] W. Blajer, "Dynamics and control of mechanical systems in partly specified motion," *Journal of the Franklin Institute*, vol. 334, no. 3, pp. 407–426, 1997.

[17] W. Blajer and Kolodziejczyk K., "A geometric approach to solving problems of control constraints: Theory and a dae framework," *Multibody System Dynamics*, vol. 11, no. 4, pp. 343–364, 2004.

[18] P. Masarti, M. Morandini, and A. Fumagalli, "Control constraint of underactuated aerospace system," *ASME, Journal of Computational and Nonlinear Dynamics*, vol. 9, no. 2, 2014.

[19] L.L. Kovács and L. Bencsik, "Stability case study of the acroboter underactuated service robot," *Theoretical and Applied Mechanics Letters*, vol. 2, no. 4, 2012, (Article 043004).

[20] J. J. E. Slotine and W. Li, *Applied Nonlinear Control*, Prentice Hall, 1995.

[21] W. Blajer, R. Seifried, and K. Kolodziejczyk, "Servo-constraint realization for underactuated mechanical systems," *Archive of Applied Mechanics*, vol. 85, pp. 1191–1207, 2015.

[22] O. Khatib, *Commande dynamique dans l espace operationnel des robots manipulateurs en presence debstacles*, Ph.D. thesis, Ecole Nationale Superieure de laAronautique et de laEspace, Toulouse, 1980.

[23] H. Goldstein, *Classical Mechanics*, 2nd ed. Addison-Wesley, 1980.

[24] M. W. Spong and M. Vidyasagar, *Robot Dynamics and Control*, John Wiley & Sons, 1989.

[25] MSC software, "http://www.mscsoftware.com/product/adams," Last accessed: March 2017.

[26] Simpack a Dassault Systémes company, "Simpack," http://www.simpack.com/, Last accessed: March 2017.

[27] MathWorks, "MatLabSimscape," https://www.mathworks.com/products/simscape.html, Last accessed: March 2017.

[28] M. Blundell and D. Harty, *Multibody Systems Approach to Vehicle Dynamics*, Elsevier Butterworth-Heinemann, 2004.

[29] ProjectChrono, "Chrono," https://projectchrono.org/, Last accessed: March 2017.

[30] MBDyn, "MBDyn - Free MultiBody Dynamics Simulation Software," https://www.mbdyn.org/, Last accessed: March 2017.

[31] R. L. Petzold, "Recent developments in the numerical solution of differential/algebraic systems," *Computer Methods in Applied Mechanics and Engineering*, vol. 36, no. 6, pp. 77–89, 2002.

[32] F.E. Udwadia and R.E. Kalaba, *Analytical Dynamics: A New Approach*, Cambridge, 1996.

[33] E. Hairer and G. Wanner, *Solving Ordinary Differential Equations II: Stiff and Differential-Algebraic Problems*, Springer-Verlag, Berlin (2nd ed.), 1996.

[34] Zdravko Terze, *Multibody Dynamics Computational Methods and Applications in Computational Methods in Applied Sciences 35*, Springer, 2014.

[35] W. Schiehlen, A. Rükgauer, and T. Schirle, "Multibody system dynamics," *Force coupling versus differential algebraic description of constrained multibody systems*, vol. 4, pp. 317–340, 2000.

[36] J. Kövecses, J.-C. Piedoboeuf, and C. Lange, "Dynamic modeling and simulation of constrained robotic systems," *IEEE/ASME Transactions on mechatronics*, vol. 8, no. 2, pp. 165–177, 2003.

[37] A. A. Shabana, *Computational Dynamics*, Wiley, 2001.

[38] R.A. Wehage and E. J. Haug, "Generalized coordinate partitioning in dynamic analysis of mechanical systems," Tech. Rep., The University of Iowa, College of Engineering, 1981.

[39] W. Blajer, W. Schiehlen, and W. Schirm, "A projective criterion to the coordinate partitioning method for multibody dynamics," *Archive of Applied Mechanics*, vol. 64, pp. 86–98, 1994.

[40] J. Baumgarte, "Stabilization of constraints and integrals of motion in dyanamical systems," *Computer methods in applied mechanics and engineering*, vol. 1, no. 1, pp. 1–16, 1972.

[41] P.E. Nikravesh and C.O. Chang, "Optimal design of mechanical systems with constraint violation stabilization method," *ASME Journal of Mechanisms*, vol. 107, pp. 493–498, 1985.

[42] P.E Nikravesh and C.O. Chang, "Bdf methods for daes in multibody dynamics: Shortcomings and improvements in real-time integration methods for mechanical system simulation," *NATO ASI Series*, vol. 69, pp. 345–352, 1990.

[43] W. Blajer, "A geometric unification of constrained system dynamicsn," *Multibody System Dynamics*, vol. 1, pp. 3–21, 1997.

[44] E. H. Moore, "On the reciprocal of the general algebraic matrix," *Bulletin of the American Mathematical Society*, vol. 26, no. 9, pp. 394–395, 1920.

[45] M.W. Spong, "Partial feedback linearization of underactuated mechanical systems," in *Proceedings of IROS'94*, Munich, Germany, 1994, pp. 314–321.

[46] I. M. M. Lammerts, *Adaptive Computed Reference Computed Torque Control*, Ph.D. thesis, Eindhoven University of Technology, 1993.

[47] Isidori A., *Nonlinear Control Systems*, 3rd ed. Springer Verlag, 1995.

[48] R. Abraham and J. E. Marsden, *Foundations of Mechanics*, Springer, 1978.

[49] M. Fliess, J. Lévine, P. Martin, and P. Rouchon, "Flatness and defect of nonlinear systems: introductory theory and examples," Tech. Rep., CAS internal report A-284, 1994.

[50] C. C. Ebenbauer and F. Allgower, "A dissipation inequality for the minimum phase property," *IEEE Transactions on Automatic Control*, vol. 53, no. 3, pp. 821–826, 2008.

[51] W. Blajer, K. Dziewiecki, K. Kolodziejczyk, and K. Mazur, "Inverse dynamics of a two-degree freedom underactuated system: Analysis and experiment," in *Proceedings of 10th Conference on Dynam Systems Theory and Applications (DSTA), December 7-10 Lodz, Poland*, 2009.

[52] A. J. Krener, "On the equivalence of control systems and the linearization of nonlinear systems," *SIAM Journal on Control and Optimization*, vol. 11, no. 4, pp. 575–590, 1973.

[53] W. Blajer and Kolodziejczyk K., "Control of underactuated mechanical systems with servo-constraints," *Nonlinear Dynamics*, vol. 50, no. 4, pp. 781–791, 2007.

[54] L.L. Kovács, A. Zelei, L. Bencsik, J. Turi, and G. Stépán, "Motion control of an under-actuated service robot using natural coordinates," in *Proceedings of ROMANSY 18 - Robot Design, Dynamics and Control*, July 5–8, 2010, Udine, Italy, pp. 331–338.

[55] G. E. Carlson, *Signal and Linear Systems Analysis with Matlab*, Wiley, New Jersey, 1998.

[56] P. Glendinning, *Stability, Instability and Chaos: An Introduction to the Theory of Nonlinear Differential Equations*, Cambridge Texts in Applied Mathematics. Cambridge University Press, 1994.

[57] P. Hartman, "A lemma in the theory of structural stability of differential equations," *Article in Proceedings of the American Mathematical Society*, vol. 11, no. 4, 1960.

[58] M Greenberg, *Advanced Engineering Mathematics (2nd ed.)*, Prentice Hall, 1998.

[59] R. DeCarlo, *A State Variable Approach with Numerical Implementation*, Prentice Hall, 1989.

[60] R. V. Cossalter and F. Maggio, "The modal analysis of a motorcycle in straight running and on a curve," *Meccanica*, vol. 39, no. 1, pp. 1–16,, 2004.

[61] J. Escalona and R. L. Chamorro, "Stability analysis of vehicles on circular motions using multibody dynamics," *Proc. IMechE, Part K: Journal of Multibody Dynamics*, 2008.

[62] P Masarti, "Direct eigenanalysis of constrained system dynamics," *Proceedings of the Institution of Mechanical Engineers, Part K: Journal of Multibody Dynamics*, vol. 223, no. 4, pp. 335–342, 2009.

[63] Y. Zhang, B. Wen, and S. Chen, "Eigenvalue problem of constrained flexible multibody systems," *Mechanics Research Communications*, vol. 24, no. 1, pp. 11–16, 1997.

[64] M. Wim and N. Silviu-Iulian, *Stability and Stabilization of Time-Delay Systems*, SIAM, 2007.

[65] M. Farkas, *Periodic Motions*, Applied mathematical sciences. Springer-Verlag, 1994.

[66] L. Bencsik, L.L. Kovács, and A. Zelei, "Stabilization of internal dynamics of underactuated systems by periodic servo-constraints," *International Journal of Structural Stability and Dynamics*, 2017, 14 pages, paper id: 1740004.

[67] L. Bencsik, L.L. Kovács, and A. Zelei, "Stability of underactuated multibody systems subjected to periodic servo constraints," in *Proceedings of Dynamical Systems Theory and Applications (DSTA)*, Dec. 7-10, 2015, Lodz, Poland, pp. 89–94.

[68] R. Seifried and W. Blajer, "Analysis of servo-constraint problems for underactuated multibody systems," *International Journal of Mechanical Sciences*, vol. 4, no. 1, pp. 113–129, 2013.

[69] F. Schnelle and P. Eberhard, *Adaptive Model Predictive Control Design for Underactuated Multibody Systems with Uncertain Parameters*, 2016.

[70] T. Porter and T. Duff, "Compositing digital images," *ACMsiggraph, Computational Graphics*, vol. 18, no. 3, pp. 253–259, 1984.

[71] S. Sastry, *Nonlinear Systems Analysis, Stability, and Control*, Springer, New York, 1999.

[72] A. De Luca, R. Mattone, and G. Oriolo, "Control of redundant robots under end-effector commands: A case study in underactuated systems," *Applied Mathematics and Computer Science*, vol. 7, no. 2, pp. 225–251, 1997.

[73] A. De Luca and G. Oriolo, "Trajectory planning and control for planar robots with passive last joint.," *The International Journal of Robotics Research*, vol. 21, pp. 575—590, 2002.

[74] W. Blajer, R. Seifried, and K. Kołodziejczyk, "Diversity of servo-constraint problems for underactuated mechanical systems: A case study illustration," *Solid State Phenomena*, vol. 198, pp. 473–482, 2013.

[75] R. Zana, *Vibration suppression of under-actuated mechanical systems, Supervisor: L. Kovács L. Bencsik*, Ph.D. thesis, Budapest University of Technology and Economics, 2015.

[76] Conrad electronics, "https://www.conrad.hu/hu/planet-hajtomu-motor-pd4266-12-61-bfec-191895.html?pid=191895," Last accessed: March 2017.

[77] W. Shepherd, L. N. Hulley, and D. T. W. Liang, *Power Electronics and Motor Control*.

[78] J. Ziegler, G. Nichols, and B. Nathaniel, "Optimum settings for automatic controllers," *Transactions of the ASME*, vol. 64, no. 11, 1942.

[79] L. Bencsik and L.L. Kovács, "Alulaktuált robotok kiszámított nyomaték szabályozása szervó kényszerek alkalmazásával," in *Proceedings of XI. Magyar Mechanikai Konferencia pp. 1-6*, Miskolc-Egyetemváros, Magyarország, August 29 - Septemeber 1, 2011.

[80] L.L. Kovács, L. Bencsik, and J. Kövecses, "Dynamic analysis of under-actuated mechanical systems for design optimization and control performance," in *Proceedings of The 2nd Joint International Conference on Multibody System Dynamics - IMSD2012*, Stuttgart, Germany, May 29 - June 1, 2012.

[81] L. Bencsik and L.L. Kovács, "Stability case study of an underactuated service robot," in *Proceedings of 11th Conference on Dynamical Systems - Theory and Applications (DSTA)*, December 5-8, 2011, Lodz, Poland, pp. 89–94.

[82] A. Zelei, L. Bencsik, G. Stépán, and L.L. Kovács, "Dynamics and actuation of the acroboter platform," in *Proceedings of The 2nd Joint International Conference on Multibody System Dynamics - IMSD2012*, May 29 - June 1, 2012, Stuttgart, Germany, pp. 333–334.

[83] L.L. Kovács, A. Zelei, L. Bencsik, and G. Stépán, "The acroboter platform - part 1: Conceptual design and dynamics modeling aspects," in *Proceedings of IUTAM Symposium on Dynamics Modeling and Interaction Control in Virtual and Real Environments - IUTAM Book Series by Springer*, 7-11 June, 2010, Budapest, Hungary, pp. 3–10.

[84] L.L. Kovács, J. Kövecses, A. Zelei, L. Bencsik, and G. Stépán, "Servo-constraint based computed torque control of underactuated mechanical systems," in *Proceedings of ASME 2011 8th International Conference on Multibody Systems, Nonlinear Dynamics, and Control*, August 28–31, 2011, Washington, USA, pp. 331–338.

[85] T. Tamas Insperger, "Stick balancing with reflex delay in case of parametric forcing," *Communications in Nonlinear Science and Numerical Simulation*, vol. 16, no. 4, pp. 2160 – 2168, 2011.

[86] L. Freidovich, A. Robertson, A. Shiriaev, and R. Johansson, "Periodic motions of the pendubot via virtual holonomic constraints: Theory and experiments," *Automatica*, vol. 44, no. 3, pp. 785–791, 2008.

[87] J. Hauser and C. C. Chung, "Converse lyapunov functions for exponentially stable periodic orbits," *Systems and Control Letters*, vol. 22, pp. 27–34, 1994.

[88] C. C. Chung and J. Hauser, "Nonlinear control of a swinging pendulum," *Automatica*, vol. 31, no. 6, pp. 851–862, 1995.

[89] T. Insperger and G. Stépán, "Act-and-wait control concept for discrete-time systems with feedback delay," *IET Control Theory & Applications*, vol. 1, no. 3, pp. 553–557, 2007.

[90] T. Insperger and G. Stépán, "Optimization of digital control with delay by periodic variation of the gain parameters," in *Proeedings of IFAC Workshop on Adaptation and Learning in Control and Signal Processing, and IFAC Workshop on Periodic Control Systems*, August 30 – September 1, 2004, Yokohama, Japan, pp. 145–150.

[91] K.F. Riley, M.P. Hobson, and S.J. Bence, *Mathematical methods for physics and engineering*, Cambridge University Press, 2010.

[92] N. Itagaki, H. Nishimura, and K. Takagi, "Two-degree-of-freedom control system design in consideration of actuator saturation," *Transactions on Mechatronics*, vol. 13, pp. 470–475, 2008.

[93] L. Bencsik, L.L. Kovács, and A. Zelei, "Periodic servo-constraints for stabilizing underactuated multibody systems," in *Proceedings of The 3rd Joint International Conference on Multibody System Dynamics and The 7th Asian Conference on Multibody Dynamics*, June 30-July 3, 2014, Busan, Korea, 2 pages.

[94] C. Guarino Lo Bianco and A. Piazzi, "Minimum-time trajectory planning of mechanical manipulators under dynamic constraints," *International Journal of Control*, vol. 75, pp. 967–980, 2002.

[95] A. Zelinsky, *Field and service robotics*, Springer-Verlag, London, 1998.

[96] L. Zaccarian and A. R. Teel, *Modern anti-windup synthesis: Control augmentation for actuator saturation (Chapter 5: Dynamic linear anti-windup augmentation)*, Princeton University Press, 2011.

[97] J.C. Doyle, R.S. Smith, and D.F. Enns, "Control of plants with input saturation nonlinearities," in *Proceedings of Americal Control Conference*, 1987, pp. 1034–1039.

[98] W. B. Bequette, *Process control: Modeling, design, and simulation*, Prentice Hall Professional, New Jersey, 2003.

[99] L. Sung-Uk and Chang Pyung. Hun, "The development of anti-windup scheme for time delay control with switching action using integral sliding surface," *Journal of Dynamic Systems, Measurement, and Control*, vol. 125, no. 4, pp. 630–638, 2004.

[100] A. Kapoor, A. R. Teel, and P. Daoutidis, "An anti-windup design for linear systems with input saturation," *Automatica*, vol. 34, no. 5, pp. 559–574, 1998.

[101] T. A. Kendi and F. J. Doyle, "An anti-windup scheme for multivariable nonlinear systems," *Journal of Process Control*, vol. 7, no. 5, pp. 329–343, 1997.

[102] F. Morabito, A. R. Teel, and L. Zaccarian, "Nonlinear antiwindup applied to euler–lagrange systems," *IEEE Transactions on Robotics and Automation*, vol. 20, no. 3, pp. 526–537, 2004.

[103] D. Maalouf, C. H. Moog, Y. Aoustin, and S. J. Li, "Maximum feedback linearization with internal stability of 2-dof underactuated mechanical systems," in *Proceedings of the 18th World Congress The International Federation of Automatic Control (IFAC 2011)*, Milano, Italy, August 28 - September 2, 2011, vol. 44, pp. 8132–8137.

[104] Alberto Bemporad, Manfred Morari, Vivek Dua, and Efstratios N. Pistikopoulos, "The explicit linear quadratic regulator for constrained systems," *Automatica*, vol. 38, pp. 3–20, 2002.

[105] P. Mercorelli, B. Paden, and D. Prattichizzo, "Perfect anti-windup in output tracking scheme with preaction," in *Proceedings of the 1998 IEEE International Conference on Control Applications*, Tireste, Italy, 1-4 September, 1998, pp. 134–138.

[106] P. Mercorelli, "An antisaturating adaptive preaction and a slide surface to achieve soft landing control for electromagnetic actuators," *Transactions on Mechatronics*, vol. 17, pp. 76 –85, 2012.

[107] M. Naghshineh and Keshmiri M., "Actuator saturation avoidance in overactuated systems," in *Proceedings of 2004 IEEE/RSJ International Conference on Intelligent Robots and Systems*, Sendai, Japan, September 28 - October 2, 2004, pp. 3613–3618.

[108] A. Zelei, L. Bencsik, and G. Stépán, "Handling actuator saturation as underactuation: Case study with acroboter service robot," *Journal of Computational and Nonlinear Dynamics*, vol. 12, no. 3, 2017.

[109] D. Liberzon, *Switching in systems and control*, Birkhäuser, Boston, 2003.

[110] O. Khatib, "Inertial properties in robotic manipulation," *The International Journal of Robotics Research*, vol. 13, no. 1, pp. 19–36, 1995.

[111] T. Yoshikawa, "Dynamic manipulability of robot manipulators," in *Proceedings of 1985 IEEE International Conference on Robotics and Automation*, 1985, vol. 2, pp. 1033–1038.

[112] W. Sun, Z. Zhao, and H. Gao, "Saturated adaptive robust control for active suspension systems," *Transactions on Industrial Electronics*, vol. 60, no. 9, pp. 3889 –3896, 2013.

[113] M. Goldfarb and T. Sirithanapipat, "The effect of actuator saturation on the performance of pd-controlled servo systems," *Mechatronics*, vol. 9, no. 5, pp. 497 – 511, 1999.

[114] L. Bencsik and L.L. Kovács, "Reduction of the effect of actuator saturation with periodic servo-constraints," *Proceedings of the Institution of Mechanical Engineers, Part C: Journal of Mechanical Engineering Science*, 2016, published online in October 20, 2016, 10 pages.

[115] L. Bencsik, A. Zelei, and L.L. Kovács, "Reduction of the effect of actuator saturation with periodic servo-constraints.," in *Proceedings of ECCOMAS Thematic Conference on Multibody Dynamics 2015*, June 29 - July 2, 2015, Barcelon, Spain, paper id: 246.

[116] M. Nordin and V. H. Frankel, *Basic biomechanics of the musculoskeletal system*, Lea & Febiger, 1989.

[117] Drapała Krzysztof, Pulaski Kazimierz, and Blajer Wojciech, "The influence of actuation modeling on the assesses joint reactions in biomechanical systems," *Polish Journal of Sport and Tourism*, vol. 20, no. 3, pp. 183–187, 2013.

[118] T. McGeer, "Passive dynamic walking," *International Journal of Robotics Research*, vol. 9, no. 2, pp. 62–82, 1990.

[119] A. M. M. Omer, R. Ghorbani, Lim. H., and A. Takanishi, "Semi-passive dynamic walking for humanoid robot using controllable spring stiffness on the ankle joint," in *Proceedings 4th International Conference on Autonomous Robots and Agents*, 2009, pp. 681–685.

[120] W. Blajer and W. Schiehlen, "Walking without impacts as a motion/force control problem," *Journal of dynamic systems, measurement, and control*, vol. 114, no. 4, pp. 660–665, 1992.

[121] T. F. Novacheck, "The biomechanics of running," *Gait and Posture*, vol. 7, pp. 77–95, 1998.

[122] Chi Running official homepage, "www.chirunning.com," last accessed: March 2017.

[123] Natural Running Center official homepage, "www.naturalrunningcenter.com," last accessed: March 2017.

[124] Newton Running official homepage, "www.newtonrunning.com," last accessed: March 2017.

[125] D. E. Lieberman, M. Venkadesan, W. A. Werbel, A. I. Daoud, S. D'Andrea, I. Davis I., I. S. Mang'Eni, and Y. Pitsiladis, "Foot strike patterns and collision forces in habitually barefoot versus shod runners," *Naure, Biomechanics*, vol. 463, no. 8723, pp. 531–535, 2010.

[126] J. Kövecses and L.L. Kovács, "Foot impact in different modes of running: mechanisms and energy transfer," *Procedia IUTAM, Symposium on Human Body Dynamics*, vol. 2, pp. 101–108, 2011.

[127] W. L. Jungers, "Barefoot running strikes back," *Nature, Biomechanics*, vol. 463, no. 7280, pp. 433–434, 2010.

[128] B. J. Benda, P. O. Riley, and D. E. Krebs, "Biomechanical relationship between center of gravity and center of pressure during standing," *IEEE Transactions on Rehabilitation Engineering*, vol. 2, no. 1, pp. 3–10, 1994.

[129] P. de Leva, "Adjustments to zatsiorsky-seluyanov's segment inertia parameters," *Journal of Biomechanics*, vol. 29, no. 9, pp. 1223–1230, 1996.

[130] W.T. Dempster, "Space requirements of the seated operator, wadc-technical report 55-159," Tech. Rep., Wright-Patterson Air Force Base, Ohio, 1955.

[131] S. Plagenhoef, F.G. Evans, and T. Abdelnour, "Anatomical data for analyzing human motion," *Research Quarterly for Exercise and Sport*, vol. 54, pp. 169–178, 1983.

[132] J. M. Font-Llagunes, R. Pamies-Vila, and J. Kövecses, "Configuration-dependent performance indicators for the analysis of foot impact in running gait," in *Proceedings of ECCOMAS Thematic Conference on Multibody Dynamics, Multibody Dynamics 2013, Book of Abstracts*, Zagreb, Croatia, 1-4 July, pp. 31–32.

[133] V.F. Hsu Chen, "Passive dynamic walking with knees: a point foot model," M.S. thesis, Massachusetts Institute of Technology. Dept. of Electrical Engineering and Computer Science, 2007, Supervisor: Russ Tedrake, 56 pages.

[134] S. Collins, A. Ruina, R. Tedrake, and M. Wisse, "Efficient bipedal robots based on passive dynamic walkers," *Science Magazine*, vol. 307, no. 5712, pp. 1082–1085, 2005, includes supplementary "online" material.

[135] M. Garcia, A. Chatterjee, A. Ruina, and M. Coleman, "The simplest walking model: stability, complexity, and scaling," *Journal of Biomechanical Engineering*, vol. 120, pp. 281–288, 1998.

[136] A. Zelei, L. Bencsik, L.L. Kovács, and G. Stépán, "Energy efficient walking and running - impact dynamics based on varying geometric constraints," in *Proceedings of 12th Conference on Dynamical Systems Theory and Applications (DSTA)*, Lodz, Poland, 2-5, December 2013, pp. 259–270.

[137] A. Zelei, L. Bencsik, L.L. Kovács, and G. Stépán, "Impact models for walking and running systems - angular moment conservation versus varying geometric constraints," in *Proceedings of ECCOMAS Thematic Conference on Multibody Dynamics*, Z. Terze, Ed., Zagreb, Croatia, 1-4 July 2013, pp. 47–48.

[138] C. Carpentier, J. M. Font-Llagunes, and J. Kövecses, "Dynamics and energetics of impacts in crutch walking," *Journal of Applied Biomechanics*, vol. 26, no. 4, pp. 473–483, 2010.

[139] J. Kövecses and J. M. Font-Llagunes, "An eigenvalue problem for the analysis of variable topology mechanical systems," *ASME Journal of Computational and Nonlinear Dynamics*, vol. 4, no. 3, pp. 9 pages, 2009.

[140] Running competitor, "www.running.competitor.com," last accessed: March 2017.

[141] Amy G. Schubert, Jenny Kempf, and Bryan C. Heiderscheit, "Influence of stride frequency and length on running mechanics," *Sports Health*, vol. 6, no. 3, pp. 210–217, 2014.

[142] B. D. Wit, D. D. Clercq, and P. Aerts, "Biomechanical analysis of the stance phase during barefoot and shod running," *Journal of Biomechanics*, vol. 33, pp. 269–278, 2000.

[143] Tri coaching, "www.tri-coaching.co.uk," (pictures about running) last accessed: March 2017.

[144] A. H. Grubera, K. A. Boyera, T. R. Derrickb, and J. Hamilla, "Impact shock frequency components and attenuation in rearfoot and forefoot running," *Journal of Sport and Health Science*, vol. 3, no. 2, pp. 113–121, 2014.

[145] L. Bencsik and A. Zelei, "Effects of human running cadence and experimental validation of the bouncing ball model," *Mechanical Systems and Signal Processing*, vol. 89, pp. 78–87, 2016.

[146] L. Bencsik and A. Zelei, "A study on the effect of human running cadence based on the bouncing ball model," in *Proceedings of Dynamical Systems Theory and Applications (DSTA)*, Dec. 7-10, 2015, Lodz, Poland, pp. 47–57.